Fall 2018

Improving air quality prediction through characterizing the model errors using data from comprehensive field experiments

Maryam Abdioskouei
University of Iowa

IMPROVING AIR QUALITY PREDICTION THROUGH CHARACTERIZING THE MODEL ERRORS USING DATA FROM COMPREHENSIVE FIELD EXPERIMENTS

by

Maryam Abdioskouei

A thesis submitted in partial fulfillment
of the requirements for the Doctor of Philosophy
degree in Civil and Environmental Engineering in the
Graduate College of
The University of Iowa

December 2018

Thesis Supervisor: Professor Gregory R. Carmichael

Graduate College

The University of Iowa

Iowa City, Iowa

CERTIFICATE OF APPROVAL

PH.D. THESIS

This is to certify that the Ph.D. thesis of

Maryam Abdioskouei

has been approved by the Examining Committee for
the thesis requirement for the Doctor of Philosophy degree
in Civil and Environmental Engineering at the December 2018 graduation.

Thesis Committee: _____

Gregory R. Carmichael, Thesis Supervisor

_____

Keri C. Hornbuckle

_____

Vaishali Naik

_____

Scott N. Spak

_____

Charles O. Stanier

To my parents.

"Tell me

into what void

the river of life flows

When

was the last time

you bathed in it?"

- *Abdellatif Laabi*

ACKNOWLEDGEMENTS

I would like to express my deepest gratitude to all who helped and supported me to during the past years. First, I would like to thank my advisor, Professor Gregory Carmichael, for his continuous support, encouragement, and advise. I would also like to express my thanks to my supportive Ph.D. committee members: Dr. Keri Hornbuckle, Dr. Vaishali Naik, Dr. Scott Spak, and Dr. Charles Stanier. I am grateful to Dr. Gabriele Pfister, Dr. Frank Flocke, and Dr. Pablo Saide for their patient with me and their invaluable guidance for most of the studies in the thesis. I acknowledge the LMOS science team, especially Dr. Brad Pierce for their contributions to this work.

Also, I would like to appreciate the Department of Civil and Environmental Engineering at the University of Iowa for giving me the opportunity be part of their graduate program. Special thanks to CGRER staff, especially Amy Parker and Jeremie Moen.

Last but not least, I am immensely grateful to mother, father, and sister for their endless unconditional love and support. I also acknowledge all my friends for their emotional support and encouragement when home was so far. My thanks go to Dr. Nariman Jahani, Maral Razmand, Dr. Ellen Black, and Hannah Molitor. I would like to thank Dr. Negin Sobhani for her support and always pushing me to be a better version of myself. I am lucky to have such wonderful people by my side.

ABSTRACT

Uncertainty in the emission estimates is one the main reasons for shortcomings in the Chemistry Transport Models (CTMs) which can reduce the confidence level of impact assessment of anthropogenic activities on air quality and climate. This dissertation focuses on understating the uncertainties within the CTMs and reducing these uncertainties by improving emission estimates

The first part of this dissertation focuses on reducing the uncertainties around the emission estimates from oil and Natural Gas (NG) operations by using various observations and high-resolution CTMs. To achieve this goal, we used Weather Research and Forecasting with Chemistry (WRF-Chem) model in conjunction with extensive measurements from two major field campaigns in Colorado. Ethane was used as the indicator of oil and NG emissions to explore the sensitivity of ethane to different physical parametrizations and simulation set-ups in the WRF-Chem model using the U.S. EPA National Emission Inventory (NEI-2011). The sensitivity analysis shows up to 57.3% variability in the modeled ethane normalized mean bias (NMB) across the simulations, which highlights the important role of model configurations on the model performance.

Comparison between airborne measurements and the sensitivity simulations shows a model-measurement bias of ethane up to -15ppb (NMB of -80%) in regions close to oil and NG activities. Under-prediction of ethane concentration in all sensitivity runs suggests an actual under-estimation of the oil and NG emissions in the NEI-2011 in Colorado. To reduce the error in the emission inventory, we developed a three-dimensional variational inversion technique. Through this method, optimal scaling factors up to 6 for ethane emission rates were calculated.

Overall, the inversion method estimated between 11% to 15% higher ethane emission rates in the Denver-Julesburg basin compared to the NEI-201. This method can be extended to constrain oil and NG emissions in other regions in the US using the available measurement datasets.

The second part of the dissertation discusses the University of Iowa high-resolution chemical weather forecast framework using WRF-Chem designed for the Lake Michigan Ozone Study (LMOS-2017). LMOS field campaign took place during summer 2017 to address high ozone episodes in coastal communities surrounding Lake Michigan. The model performance for clouds, on-shore flows, and surface and aircraft sampled ozone and NOx concentrations found that the model successfully captured much of the observed synoptic variability of onshore flows. Selection of High-Resolution Rapid Refresh (HRRR) model as initial and boundary condition, and the Noah land surface model, significantly improved comparison of meteorology variables to both ground-based and aircraft data. Model consistently underestimated the daily maximum concentration of ozone. Emission sensitivity analysis suggests that increase in Hydrocarbon (HC). Variational inversion method and measurements by GeoTAS and TROPOMI instruments and airborne and ground-based measurements can be used to constrain NOx emissions in the region.

PUBLIC ABSTRACT

Chemistry Transport Models (CTMs) are developed to simulate the faith of atmospheric constituents. These simulations are then used to assess the impact of anthropogenic activities on the air quality and climate and assist the policy makers to develop effective mitigation policies. The focus of this dissertation is to better understand the uncertainties in the CTMs and emission estimates and use comprehensive measurements of atmospheric constituents to reduce these uncertainties.

In the first part, we used a 3-dimensional atmospheric chemistry transport model, i.e., Weather Research and Forecasting with Chemistry (WRF-Chem), in conjunction with extensive measurements from two major field campaigns in Colorado to reduce the uncertainties in the oil and Natural Gas (NG) emission estimates. Ethane was used as the indicator of oil and NG emissions to explore the sensitivity of ethane to different set-ups in the WRF-Chem model using the official U.S. EPA National Emission Inventory (NEI-2011). All the simulations showed large underestimation in ethane concentrations which suggests a large underestimation of oil and NG emission rates in NEI-2011. To reduce the error in the emission inventory, we developed a novel inverse modeling technique. Using this method, optimal scaling factors for ethane emission rates were calculated with the goal to minimize the discrepancies between model and observations. By applying the optimal scaling factors to the emission inventory, we improved the model performance and reduce the uncertainties in the oil and NG emission estimates.

The second part describes the University of Iowa high-resolution chemical weather forecast framework using WRF-Chem and NEI-2011 emission inventory designed for the Lake

Michigan Ozone Study (LMOS-2017) field campaign. The goal of the LMOS field campaign was to assist in understanding the high ozone concentrations in coastal communities surrounding Lake Michigan. WRF-Chem model successfully captured the atmospheric transport but underestimated the daily maximum ozone concentrations. Performing WRF-Chem simulations using different emission scenarios suggests that increase in the Hydrocarbon (HC) emissions can improve the model performance in capturing maximum ozone concentrations.

TABLE OF CONTENTS

LIST OF TABLES

LIST OF FIGURES

1 GENERAL INTRODUCTION

1.1 Background and Significance

High levels of outdoor air pollutions such as fine particulate matter and ozone have been associated with many health and environmental impacts causing 3.3 million premature death annually worldwide (Lelieveld et al., 2015). Other than the health impact, gaseous and particulate air pollutants such as methane, ozone, and fine Particulate Matters (PM) can impact the climate by changing the solar radiation budget (Fiore et al., 2012). Atmospheric Chemistry and Transport models (CTMs) have been used to predict the levels of air pollutions and to study the health and climate impact of these pollutants (Anenberg et al., 2010; Fiore et al., 2012; Lelieveld et al., 2013; Silva et al., 2013). Accurate simulation of atmospheric transport and chemistry is essential for the development of effective mitigation policies to minimize the health and climate impact of air pollutants. The estimates of air pollutant concentrations have been improved due to better representation of atmospheric processes in the CTMs, increase in model resolutions, and more available atmospheric measurements. However, there are still large uncertainties associated with CTMs and emission inventories which call for more work. The abundance of atmospheric measurement from ground-sites, field experiments, and satellites, provides an opportunity to study and address the shortcomings of CTMs in much more details using systematic data-driven methods. The main focus of this dissertation is to quantify and reduce the uncertainties in the CTMs and emission inventories using various suites of measurements.

The first part of this study focuses on improving emission estimates from oil and Natural Gas (NG) sector. With the rapid increase in the oil and NG production in the United States (US), high levels of methane, Non-Methane Hydrocarbons (NMHC), and NOx were measured in the

vicinity of oil and NG fields (Allen, 2016a) which were not captured in the official emission inventories (Brandt et al., 2014).

Methane is the primary constituent of NG and the second most important greenhouse gas after carbon dioxide (CO_2). Methane has a shorter effective lifetime (~ 12 years) than CO_2, but 37 times stronger radiative forcing (on a molar basis). Therefore, it has a stronger near-time climate impact in comparison with CO_2 (Alvarez et al., 2012). Methane is a precursor to tropospheric ozone and contributes to tropospheric ozone production and background ozone which has severe impacts on human health, vegetation, and crops. High concentrations of methane have been observed by ground-based, airborne, and satellite measurement tools in regions with heavy oil and NG operation (Karion et al., 2013; Kort et al., 2014; Miller et al., 2013; Pétron et al., 2014; Schneising et al., 2014; Turner et al., 2015; Zavala-Araiza et al., 2015).

Elevated levels of NMHCs (such as ethane, propane, n-butane, i-pentane, n-pentane, and benzene) (Halliday et al., 2016; Pétron et al., 2014) and ozone (Ahmadov et al., 2015b; Field et al., 2015; Oltmans et al., 2014; Rappenglück et al., 2014) have been measured in the areas close to oil and NG operation sites. At the global scale, studies have reported a significant increase in the global concentration of ethane and propane in recent years due to increase in oil and NG activities in North America (Franco et al., 2016; Hausmann et al., 2016; Helmig et al., 2016; Kort et al., 2016).

We used measurements from Front Range Air Pollution and Photochemistry Éxperiment (FRAPPÉ) and Deriving Information on Surface Conditions from COlumn and VERtically Resolved Observations Relevant to Air Quality (DISCOVER-AQ) field experiments and high-resolution Weather Research and Forecasting with Chemistry (WRF-Chem) model (Grell et al., 2005; Skamarock et al., 2008) simulations to assess the model performance in capturing ethane

(oil and NG tracer) and quantify the impact of WRF-Chem physical parametrization and set-up on the uncertainties in the model. Next, we used a variational inversion method to constrain ethane emissions from the oil and NG sector.

The second part of this work focuses on tropospheric ozone formation over Lake Michigan. Urban and rural regions around Lake Michigan have persistently recorded high ozone concentrations. The high ozone concentrations along the shore are associated with the lake breeze (Harris and Kotamarthi, 2005; Lennartson and Schwartz, 1999; Lyons and Olsson, 1973). During the summer, morning land breeze transport pollutants to the shallow stable layer over the lake. Ozone is produced in this stable layer and being transported over the land with the afternoon lake breeze (Cleary et al., 2015; Dye et al., 1995; Foley et al., 2011). CTMs have difficulties predicting the surface ozone concentrations in this region because of the unique meteorology and combination of anthropogenic and biogenic emissions (McNider et al., 2018). Lake Michigan Ozone Study (LMOS) field experiment was conducted from 22 May to 21 June 2017 to measure ozone and ozone precursors concentration using ground-based, airborne, and remote sensing instruments. We used the measurements from the LMOS experiments and high-resolution WRF-Chem model to assess the model and emission inventory performance in capturing transport, formation, and concentration of ozone and ozone precursors.

1.2 Thesis Outline

In chapter 2, We used ethane as the indicator of oil and NG emissions and explored the sensitivity of ethane concentration to different physical parametrizations and simulation set-ups in the WRF-Chem model using the U.S. EPA National Emission Inventory (NEI-2011). We evaluated the impact of the following configurations and parameterizations on predicted ethane concentrations: Planetary Boundary Layer (PBL) parametrizations, daily re-initialization of meteorological variables, meteorological initial and boundary conditions, and horizontal

resolution. We assessed the uncertainties around oil and NG emissions by using measurements from FRAPPÉ and DISCOVER-AQ field campaigns over the Northern Front Range (NFR) Colorado in summer 2014. Under-prediction of ethane concentration in all sensitivity runs suggests an actual under-estimation of the oil and NG emissions in the NEI-2011. An Increase of oil and NG emissions in the simulations partially improved the model performance in capturing ethane and lumped alkanes (HC3) concentrations but did not impact the model performance in capturing benzene and toluene which is due to very low emission rates of these species from oil and NG sector in the NEI-2011. This chapter is based on the results published in Abdi-Oskouei et al. (2018)

In chapter 3, a three-dimensional variational inversion technique is developed to reduce the uncertainties of ethane emissions from oil and NG sector in Colorado. We used the extensive observational data set provided by the FRAPPÉ and the DISCOVER-AQ filed campaigns in summer 2014 over Colorado in conjunction with the WRF-Chem. The important advantage of this inverse modeling method is the ability to constrain emissions at high temporal and spatial resolution (Saide et al., 2015). Furthermore, it is possible to simultaneously constrain multiple species and include multiplatform measurements. Performing inverse modeling technique provided us with optimal scaling factors for emissions rates with the goal to minimize the discrepancies between model and measurements. This chapter discusses the details of the inverse modeling method and assesses the performance of the model based on improved emission inventory.

Chapter 4 provides details about the LMOS field experiment. LMOS took place during May and June 2017 to address high ozone episodes in coastal communities surrounding Lake Michigan. Aircraft, ship, mobile lab, and ground-based stations were used in this campaign to build an

extensive dataset regarding ozone, its precursors, and particulate matter. A forecasting system was designed to produce high-resolution (4x4 km^2 horizontal resolution and 53 vertical levels) forecast products using the WRF-Chem modeling system in support of experimental planning during LMOS 2017. Preliminary in-field evaluation of model performance for clouds, on-shore flows, and surface and aircraft sampled ozone and NOx concentrations found that the model successfully captured much of the observed synoptic variability of onshore flows. The model captured the variability of ozone concentration well, but under-predicted peak ozone concentration during high ozone episodes. In post-campaign WRF-Chem simulations, we investigated the sensitivity of the model performance to different physical parametrization and model set-ups. We also studied the sensitivity of ozone formation to changes to anthropogenic and biogenic hydrocarbon and NOx emissions.

Chapter 5 summarizes the important findings from chapters 2 to 4, highlights the concluding remarks, and discuss the future directions.

2 IMPACTS OF PHYSICAL PARAMETRIZATION ON PREDICTION OF ETHANE CONCENTRATIONS FOR OIL AND GAS EMISSIONS IN WRF-CHEM

Abstract. Recent increases in the Natural Gas (NG) production through hydraulic fracturing have called into question the climate benefit of switching from coal-fired to natural gas-fired power plants. Higher than expected levels of methane, Non-Methane Hydrocarbons (NMHC), and NOx have been observed in areas close to oil and NG operation facilities. Large uncertainties in the oil and NG operation emission inventories reduce the confidence level in the impact assessment of such activities on regional air quality and climate, as well as development of effective mitigation policies. In this work, we used ethane as the indicator of oil and NG emissions and explored the sensitivity of ethane to different physical parametrizations and simulation set-ups in the Weather Research and Forecasting with Chemistry (WRF-Chem) model using the U.S. EPA National Emission Inventory (NEI-2011). We evaluated the impact of the following configurations and parameterizations on predicted ethane concentrations: Planetary Boundary Layer (PBL) parametrizations, daily re-initialization of meteorological variables, meteorological initial and boundary conditions, and horizontal resolution. We assessed the uncertainties around oil and NG emissions by using measurements from the FRAPPÉ and DISCOVER-AQ campaigns over the Northern Front Range Metropolitan Area (NFRMA) in summer 2014. The sensitivity analysis shows up to 57.3% variability in normalized mean bias of the near-surface modeled ethane across the simulations, which highlights the important role of model configurations on the model performance and ultimately the assessment of emissions. Comparison between airborne measurements and the sensitivity simulations indicates that the model-measurement bias of ethane ranged from -14.9 ppb to -8.2 ppb (NMB ranged from -80.5% to -44%) in regions close to oil and NG activities. Under-prediction of ethane concentration in all sensitivity runs suggests an actual under-estimation of the oil and NG

emissions in the NEI-2011. Increase of oil and NG emissions in the simulations partially improved the model performance in capturing ethane and lumped alkanes (HC3) concentrations but did not impact the model performance in capturing benzene, toluene, and xylene which is due to very low emission rates of these species from oil and NG sector in the NEI-2011.

2.1 Introduction

Recent advances in the unconventional Natural Gas (NG) production technology (hydraulic fracturing) have resulted in economical access to NG reserves in deep shale formations and a 36% rise in US NG production from 2005 to 2014 (Lyon, 2015). Increase in the NG production, decrease in the NG price, and environmental advantages of NG-fired power plants over coal-fired power plants have made NG an important competitor for coal in the electricity generation sector. In 2015, NG and coal each had a 33% share in the electricity generation in the US. It is predicted that NG's share in electricity generation will grow 1.5% every year (Energy information administration of US Department of Energy., 2016; U.S. Energy Information Administration, 2016). With the rapid increase in the unconventional oil and NG production, higher than expected levels of greenhouse gases, specifically methane, and air pollutants such Non-Methane Hydrocarbons (NMHC) and NO_x (from flaring or compressors, reboilers, pneumatic devices, trucks, and other equipment using fossil fuel) (Allen, 2016b; Olaguer, 2012) have been observed in some places in vicinity of oil and NG facilities. The high concentrations of these chemicals measured in many studies at different scales and regions suggest that official emission inventories (e. g. Greenhouse Gas Inventory (GHGI) and Emission Database for Global Atmospheric Research (EDGAR)) fail to capture the magnitude of emissions from unconventional extraction activities (Brandt et al., 2014). The underestimation of emission inventories has raised concerns regarding the climate implications of promoting NG as the "bridge fuel" (Alvarez et al., 2012; Howarth et al., 2011; Levi, 2013; McJeon et al., 2014), and

its impacts on the air quality and public health (Halliday et al., 2016; McKenzie et al., 2012). Additionally, Methane and NMHC emitted from the oil and NG sector can degrade regional air quality and contribute to ozone formation on regional and global scales (Helmig et al., 2016). Outdated Emission Factors (EF), super-emitters in the production systems, and rapid growth in the production facilities are some of the reasons for the underestimation (Brandt et al., 2014; Lyon, 2015; Zavala-Araiza et al., 2015).

The Colorado Northern Front Range (NFR), including the Denver metropolitan area, is located between the Rocky Mountains and the High Plains with a total population of about 4.8 million. In 2007, a large region of the NFR was declared in nonattainment of the National Ambient Air Quality Standard (NAAQS) for 8h average ozone. Major sources of pollutants in this area are vehicle emissions, oil and NG operation, agriculture and feedlots, and power plants. In the past years, oil and NG development has increased drastically in the NFR. NG production in Weld County has increased from 55.8×10^6 m^3 (1.97×10^6 Thousand Cubic Feet (MCF)) to 181.8×10^6 m^3 (6.42×10^6 MCF) from 2004 to 2016. The Wattenberg gas field in Weld County is close to populated regions and has the highest well density in the NFR with more than 25,000 active NG wells (Colorado Oil and Gas Conservation Commission, 2017). In the NFR, measured NMHCs are 18-77 times greater than the regional background as determined from the NOAA flask network (Thompson et al., 2014). High levels of NMHC can cause health concerns at regional scales and can contribute significantly to the ozone pollution in the region (Cheadle et al., 2017; Gilman et al., 2013; McDuffie et al., 2016; Pétron et al., 2012; Pfister et al., 2017b; Thompson et al., 2014). Using box models constrained with observations, McDuffie et al. (2016) estimated that NFR oil and NG activities contribute ~50% to the regional Volatile Organic Compound (VOC) OH reactivity and 20% to the regional photochemical ozone production.

Mass balance approach methods have been widely used to estimate the emissions from oil and NG activities (Conley et al., 2016; Karion et al., 2015; Peischl et al., 2016; Pétron et al., 2012; Smith et al., 2015). This method cannot provide details on the spatial and temporal variability of emissions and has limitations in domains with complex atmospheric transport such as the NFR. High resolution three-dimensional atmospheric chemical transport models can better capture the variability in meteorology and chemistry in different domains. Paired with observations and using inverse modeling techniques, these models help evaluate the performance of emission inventories on high temporal and spatial scales (Barkley et al., 2017; Cui et al., 2014, 2017) and allow assessments of the impact of oil and NG activities on regional air quality. Ahmadov et al. (2015) used the Weather Research and Forecasting Model with Chemistry (WRF-Chem) to study high ozone episodes and emission reduction scenarios in the Uintah Basin. Their results show a strong underestimation of methane and VOC emissions in the National Emission Inventory 2011 (NEI-2011).

WRF-Chem provides users with different dynamical, physical, and chemical schemes (Grell et al., 2005; Skamarock et al., 2008). These choices can impact the performance of the model, specifically in regions with complex transport patterns (Saide et al., 2011). In order to assess the performance of emission inventories, it is critical to address the uncertainties derived from model configurations on simulated concentration fields. The goal of this study is to quantify the impact of WRF-Chem configurations on predicting the oil and NG emissions in the NFR. VOCs in the NFR have shown a clear source signature associated with oil and NG activities (Gilman et al., 2013; Pétron et al., 2014). Diverse air pollution sources and complex metrological patterns due to mountain-valley circulation, high elevation, and harsh terrain are some of the challenges for air quality modeling in this area. We use ethane, which has a simple chemical cycle and a lifetime of about two months, as a tracer for oil and NG (Helmig et al., 2016). The model and

emission inventory performance are evaluated by comparing meteorological parameters as well as ethane and VOC concentrations to surface and airborne measurements. We explore the sensitivity of the modeled transport and ethane concentrations to different WRF-Chem physical parametrizations and set-ups. This work will be followed by development of an inverse modeling technique to constrain the oil and NG emission rates by calculating optimal scaling factor for the emission inventory. Simulations discussed in this study will be used to calculate the variability of the optimal scaling factor. To inform not only about the absolute magnitude in the ethane emissions but to further explore the feasibility to constrain other trace gas oil and NG emissions, we investigate CO and VOC emission estimates from oil and NG sector and VOC ratios in the observations and the model.

2.2 Method

2.2.1 Aircraft and ground-based observations

The National Science Foundation/National Center for Atmospheric Research (NSF/NCAR) Front Range Air Pollution and Photochemistry Éxperiment (FRAPPÉ) and National Aeronautics and Space Administration (NASA) Deriving Information on Surface Conditions from COlumn and VERtically Resolved Observations Relevant to Air Quality (DISCOVER-AQ) campaigns were conducted in July and August 2014, in the NFR Colorado. These two campaigns provide detailed and coherent airborne and ground-based measurements in this area, which can assist in evaluation and improvement of chemical transport models and emission inventories. The NSF/NCAR C130 collected extensive airborne measurements of various atmospheric constituents during the FRAPPÉ campaign. A total of 15 flights (~80 flight hours) were conducted in the NFR with the goal of mapping the emissions and their transport and chemistry in this region. During the DISCOVER-AQ campaign, the NASA P3B aircraft performed approximately 20 flights containing spiral ascents or descents over six key sites in the NFR to

capture the vertical profiles of the atmospheric constituents and their diurnal variation. Ethane was measured on board of C130 and P3 aircrafts. On C130 aircraft, ethane was measured by the University of Colorado's CAM instruments with detection sensitivity of 15 ppt, details for which are discussed in Richter et al. (2015). Aerodyne Ethane-Mini spectrometer on P3 was used to measure ethane concentration (Yacovitch et al., 2014). Fried (2015) compared CAMS ethane measurements with sub-ppb precision with the Aerodyne measurements during wing tip comparisons and the agreement was within 9%, corresponding to differences of less than 55 ppt.

The National Oceanic and Atmospheric Administration (NOAA), the Colorado Department of Public Health and Environment (CDPHE), and the National Park Services (NPS) operated numerous ground-level measurement sites during these two campaigns. In this work, we present ground-level measurements from the NOAA Boulder Atmospheric Observatory (BAO; 40.05°N, 105.01°W, 1584 m above sea level (asl)), the NOAA Platteville site (PAO; 40.18°N, −104.73°W, 1523 m asl), Fort Collins (FC; 40.89°N, -105.13°W, 1572 m asl), NREL-Golden (Golden; 39.74°N, -105.18°W, 1833 m asl), and CDPHE wind measurements at Weld County tower (WC-Tower; 40.39°N, -104.73°W, 1483 m asl), Rocky Flats N (RF-N;39.91°N, -105,19°W, 1803 m asl), Welch (39.64°N, -105.14°W, 1743 m asl), Chatfield (39.53°N, -105.07°W, 16756 m asl), and Aurora-East (39.64°N, -104.57°W, 1802m asl). BAO and PAO are located north of Denver and close to the Wattenberg Gas Field in Weld County (Figure 2-1). Measurements of temperature, relative humidity, wind speed and direction at 10m, 100m, and 300m were recorded at BAO. Surface wind measurements from PAO (3m) and WC-Tower (4m) were used in this study. The planetary Boundary Layer (PBL) height was measured and calculated at PAO, Fort Collins (FC), and NREL-Golden using micro-pulse Lidar backscatter during the daytime (Compton et al., 2013).

2.2.2 ***WRF-Chem model***

We used WRF-Chem 3.6.1 (Grell et al., 2005; Skamarock et al., 2008), a fully coupled online air quality and transport model, to investigate the sensitivity of modeled PBL, winds, temperature, relative humidity, and ethane concentrations to different physical parametrizations and configurations. Figure 2-1illustrates the location of the two nested domains and the underlying terrain map. We used one-way nesting (i.e., the outer domain ran independently of the inner domain). The outer domain has a 12 km × 12 km horizontal resolution, and the inner domain has a 4 km × 4 km horizontal resolution. Both domains have 53 vertical levels with the domain top at 50 hPa (~11 layers below 1km). The outer domain is designed to capture the emission from the Western US, and the inner domain includes Colorado and Utah. Sensitivity simulations start on 24 July 2014 and end on 18 Aug 2014.

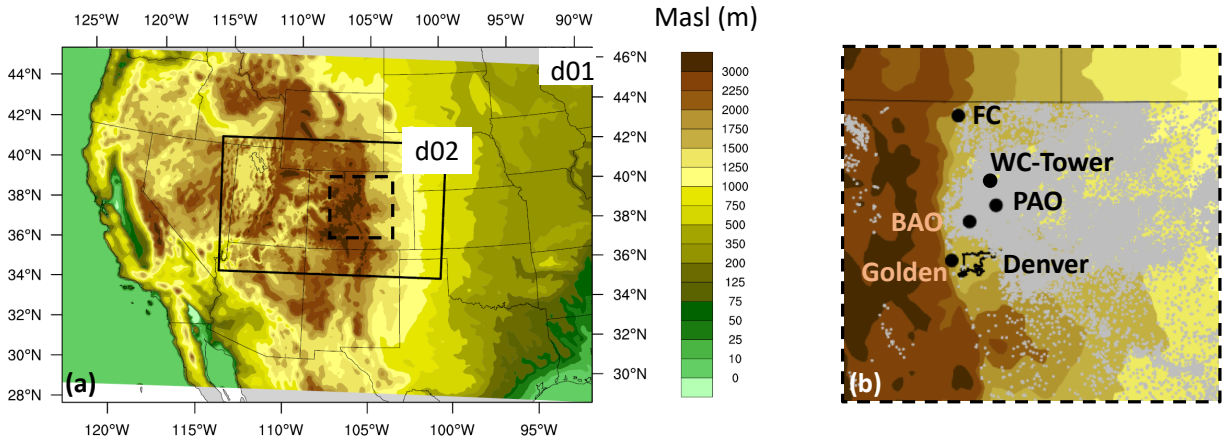

Figure 2-1 Terrain map of the WRF-Chem outer domain (d01) and inner domains (d02) and location of observation sites. a) shows the two nested domains designed for this study. b) shows the zoomed in map of domain 2 with the location of several sites. Grey dots show the location of permitted wells (http://cogcc.state.co.us/)

Table 2-1 shows a summary of the WRF-Chem configurations for this study, used in all sensitivity simulations. The Morrison double-moment scheme was selected as the microphysics option and Goddard shortwave (Chou and Suarez, 1999) and RRTMG longwave radiation

schemes (Iacono et al., 2008) were used as shortwave and longwave radiation parametrizations, respectively. The Grell-Freitas convection scheme (Grell and Freitas, 2014) was used as convective parametrization for both outer and inner domain. The inner domain falls into the "grey-scale" which means many of the assumptions used in convective parametrization will no longer be valid at this resolution. The Grell-Freitas convection scheme is a stochastic scale dependent convective parametrization based on the method proposed by Arakawa et al. (2011) and is designed for domains with horizontal resolution up to few kilometers. Comparisons between a simulation with resolved convection of inner domain and a simulation using the Grell-Freitas convective parametrization in the inner domain showed similar performance in capturing transport (not shown). Thus, we used the Grell-Freitas convective scheme for both domains in all simulations to reduce the computation costs.

Table 2-1 Summary of basic WRF-Chem configuration

Category	Selected option
Horizontal resolution	12km and 4km
Vertical resolution	53 layers (11 within the lowest 1km)
Microphysics	Morrison double-moment scheme
Land Surface	5-layer thermal diffusion
Shortwave radiation	Goddard shortwave
longwave radiation	RRTMG scheme
Cumulus parametrization	Grell-Freitas scheme

Gas-phase chemistry	RACM-ESRL
Biogenic emission	MEGAN

We selected the Regional Atmospheric Chemistry Mechanism chemistry using Earth System Research Laboratory (RACM-ESRL) (Stockwell et al., 1997) coupled to the Modal Aerosol Dynamics Model/Secondary Organic Aerosol Model (MADE/SORGAM). RACM includes 17 stable inorganics, 4 inorganic intermediates, 32 stable organic species, and 24 organic intermediates. RACM_ESRL (Kim et al., 2009) is an updated version of the RACM mechanism and includes 23 photolysis and 221 chemical reactions (Ahmadov et al., 2015c). To reduce the computational costs, hydrocarbons with similar behavior are lumped together in the chemical mechanisms. For example, "HC3" in the RACM_ESRL mechanism includes alkanes such as propane, n-butane, isobutane, and acetylene (ethyne), and alcohols such as methanol and ethanol. "TOL" includes toluene and benzene. Ethane and methane are treated exclusively in the RACM_ESRL mechanism. More details regarding the reactions and lumping groups can be found in Stockwell et al., 1997. Chemical boundary conditions from Monitoring Atmospheric Composition and Climate reanalysis (MACC), available every 3 hours, (Inness et al., 2013) and model outputs from RAQMS, available every 6 hours, (Natarajan et al., 2012; Pierce et al., 2007) were used as chemical boundary and initial conditions in the simulations. The model outputs from these global models are specific to the simulation time (24 July 2014 tp 18 Aug 2014) and are interpolated to the WRF-Chem domain and temporal resolution prior to starting the simulations. Ethane concentrations showed no strong sensitivity to the two different chemical initial and boundary conditions (i.e., RAQMS and MACC) and is not discussed further.

2.2.2.1 WRF-Chem sensitivity tests

WRF-Chem provides users with a number of different dynamical, physical, and chemical schemes. Users can select schemes based on the physical properties of the domain of interest, goals of the study, and computational limitations. We evaluated the sensitivity of WRF-Chem to different physics options, such as the PBL parametrization, and configurations including daily re-initialization of meteorological fields, different meteorological initial and boundary conditions, and varying horizontal resolution. Table 2-2 shows details on the sensitivity runs and lists the meteorological and chemical boundary conditions used for each run. The naming system for the simulations is based on the different settings (e.g. simulation 5-MnERi represents the simulation number (5), PBL Scheme (MYNN3), meteorological initial and boundary condition (ERA-interim), chemical initial and boundary condition (RAQMS), and daily re-initialization of meteorological fields (i)). Simulation ID in Table 2-2 has been used when discussing sensitivity tests in the paper.

Table 2-2. Summary of WRF-Chem configurations for sensitivity tests designed for this study

Test	Sim. ID	Sim. Name	PBL Scheme	Met IC & BC	Chem IC & BC	Init.	Emiss.
PBL	PBL1	1-YFM	YSU (Y)	NCEP-FNL (F)	MACC (M)	Free run	NEI11
	PBL2	2-MjFM	MYJ (Mj)	NCEP-FNL (F)	MACC (M)	Free run	NEI11
	PBL3	3-MnFM	MYNN3 (Mn)	NCEP-FNL (F)	MACC (M)	Free run	NEI11
Initialization	Init4	4-MnER	MYNN3 (Mn)	ERA-interim (E)	RAQMS (R)	Free run	NEI11
	Init5	5-MnERi	MYNN3 (Mn)	ERA-interim (E)	RAQMS (R)	re-init (i)	NEI11
Met IC & BC	Met5	5-MnERi	MYNN3 (Mn)	ERA-interim (E)	RAQMS (R)	re-init (i)	NEI11
	Met6	6-MnFRi	MYNN3 (Mn)	NCEP-FNL (F)	RAQMS (R)	re-init (i)	NEI11
Horizontal	Hor5	5-MnERi	MYNN3 (Mn)	ERA-interim (E)	RAQMS (R)	re-init (i)	NEI11

	Hor5-12km	5-MnERi-12km	MYNN3 (Mn)	ERA-interim (E)	RAQMS (R)	re-init (i)	NEI11
Emission Inventory	Em7	5-MnERiMeg	MYNN3 (Mn)	ERA-interim (E)	RAQMS (R)	re-init (i)	NEI11 + Megan
	Em8	7-MnERiMeg-2OnG	MYNN3 (Mn)	ERA-interim (E)	RAQMS (R)	re-init (i)	NEI11 (2x OG) + Megan

An accurate simulation of air pollution is dependent on a precise description of transport processes, meteorological conditions, and the PBL height (PBLH) (Cuchiara et al., 2014; Hu et al., 2010). Transport of pollutants within the domain depends on turbulent motions and vertical mixing within the PBL. WRF-Chem (3.6.1) has eleven different PBL schemes to address the closure problem in the simulation of turbulent motions. In general, PBL schemes can be classified into two main groups; local and non-local. A local PBL scheme estimates the turbulent fluxes of heat, momentum, and moisture from local mean and gradient flux values. In a non-local PBL scheme, non-local fluxes can influence fluxes in each grid, hence they are expected to better capture large-size eddies in the simulation (Stull, 1988). We tested one non-local and two local PBL schemes to understand the sensitivity of the model to PBL parameterization in a domain with high elevation and complex terrain. We used Yonsei University (YSU) first order (Hong et al., 2006) as the non-local PBL scheme in the PBL1 (1-YFM) simulation. The local schemes used in PBL2 (2-MjFM) and PBL3 (3-MnFM) simulations were Mellor–Yamada–Janjic (MYJ) 1.5 order (2.5 level) (Janjic, 2001; Janjic et al., 2000) and Mellor-Yamada-Nakanishi-Niino (MYNN3) 3rd level (Nakanishi and Niino, 2009).

WRF-Chem is a mesoscale model and requires initial and boundary conditions from a larger-scale model. Usually, these initial and boundary conditions are taken from re-analysis products of larger-scale models optimized using assimilation techniques and observations. The choice of initial and boundary condition products can impact the model performance (Angevine et al., 2012; Saide et al., 2011). We tested two different meteorological initial and boundary conditions,

European Reanalysis (ERA-interim) by European Center for Medium-Range Weather Forecasts (ECMWF) in Met5 (5-MnERi) simulation and NCEP's Global Forecast System (GFS) in Met6 (6-MnFRi) simulation. ERA-Interim reanalysis is produced with 80km by 80km horizontal and 6-hour temporal resolution (European Centre for Medium-Range Weather Forecasts (ECMWF), 2009), and NCEP FNL (final) operational global analysis is produced using GFS with 1-degree by 1-degree horizontal and 6-hour temporal resolution (National Centers for Environmental Prediction, National Weather Service, NOAA, 2000).

Simulations were performed for 24 days from 24 July 2014 to 18 August 2014. Initializing the meteorological fields in the simulation at the first time step with the larger-scale model values and running it for 24 days without any nudging will result in deviations from the larger scale re-analysis products. On the other hand, the lower resolution of the larger-scale models can lower the accuracy of WRF-Chem high-resolution simulations. To investigate this impact, we tested two different set-ups for WRF-Chem. In Init4 (4-MnER) simulation, we initialized the meteorological fields at the first time step with larger-scale model values and ran the simulation freely for 24 days ("free run"). In Init5 (5-MnERi) simulation, the meteorological fields were re-initialized every day at 18 UTC (12pm local time) and run for the next 30 hours. The first 6 hours of the simulation (18 UTC to 00 UTC) were discarded to allow for the model to spin up. In this set-up, chemistry fields were recycled from previous cycles of simulations.

The sensitivity of the model to the horizontal resolution was examined by comparing the performance of the outer domain (12 km × 12 km) to the inner domain (4 km × 4 km) in Hor5 (5-MnERi) simulation. In one-way nesting, the outer domain runs independently of the inner domain; thus, comparing the performance of the outer and inner domains is valid.

2.2.2.2 Emission inventory

NEI-2011 version 2 is a bottom-up emission inventory of U.S. anthropogenic emissions. While we cannot expect the year 2011 inventory to fully represent the model year 2014, it was the only inventory available to the WRF-Chem user community at the time of this study. Emissions in this inventory are calculated based on fuel consumption, source activity, and emission factors reported by state, tribal, and local governing agencies (U.S. Environmental Protection Agency, 2015). WRF-Chem provides a processed version of NEI-2011 to the users, which includes emission of 76 species (50 speciated VOC compounds, 19 PM2.5 aerosol species, and 7 primary species). NEI-2011 and emissions for only oil and NG sector in the NEI-2011 were provided to us by Dr. Stuart McKeen (NOAA Earth Systems Laboratory, Boulder, CO). Table Appendix 1 includes details on the mapping table used to convert NEI-2011 species to RACM and MADE/SORGAM chemical and aerosol mechanism. The separate oil and NG emission information was used to conduct an additional sensitivity simulation with perturbed oil and NG emission, which we used to study the sensitivity of modeled ethane concentrations as well as concentrations of VOCs and CO to the oil and NG emission sector. We used the Model of Emissions of Gases and Aerosols from Nature (MEGAN) for biogenic emission in all simulations (Guenther et al., 2012). Ethane does not have a significant biogenic source (Yacovitch et al., 2014); thus, we did not assess the impact of biogenic emissions in this study. Wildfire emissions were not included in the simulations, but this will have a negligible impact on the results as wildfires did not significantly influence the air quality in the NFR during the FRAPPÉ campaign (Valerino et al., 2017).

2.3 Results and Discussion

We start with an evaluation of the overall performance of all simulations and later provide a detailed discussion on the different sets of sensitivity simulations. To evaluate the sensitivity of

WRF-Chem to different physical parametrizations, we compared the simulated meteorological variables, such as temperature, relative humidity, wind fields, and PBLH, with measurements. 27 July 2014 and 28 July 2014 were reported as Denver cyclone episodes (Dingle et al., 2016; Valerino et al., 2017; Vu et al., 2016), and neither simulation captured the cyclone pattern and enhancements accurately on these two days. Thus, we only included the period of 1 August 2014 to 15 August 2014 in our analysis to avoid skewing the results because of large model errors during the Denver cyclone episode. For quantitative comparison between the simulations, we used statistical measures including correlation coefficient (R), root mean square error (RMSE), mean absolute error (MAE), mean bias (MB), and normalized mean bias (NMB). Definitions of these metrics can be found in the supplement. We used NMB as a proxy for model sensitivity to quantify the impact of model configuration on different variables. Variability of NMB (calculated by subtracting minimum NMB from maximum NMB) in sensitivity tests can provide a range for uncertainties in the model cases independent of the model values.

2.3.1 Evaluation of overall model performance

Table 2-3 includes the statistical measures for temperature and relative humidity in all the simulation tests at 100m altitude at BAO. Figure 2-2 compares the diurnal cycles of measured temperature, relative humidity, wind speed, and wind direction at 100m altitude at BAO with corresponding model values for all the simulation tests. While Figure 2-2 provides an overview of all sensitivity tests, Figure Appendix 2 separates each sensitivity test to provide a clearer test by test comparison. Similarly, Table Appendix 2 to 5 includes statistical measures and Figure Appendix 1 and Figure Appendix 3 show diurnal cycles of temperature, relative humidity, wind speed, and wind direction at BAO 10m and 300m. All model simulations capture the overall daily cycle in temperature and relative humidity well (Figure 2-2 and Table 2-3). The variability across different sensitivity runs can be large, with modeled temperature varying by up to 6°C and the

model-measurement NMB ranging from -3.9% to 11.1%. Relative humidity has larger variability among the simulations during nighttime compared to daytime. The NMB of relative humidity ranges from -29.7% to 52.6%.

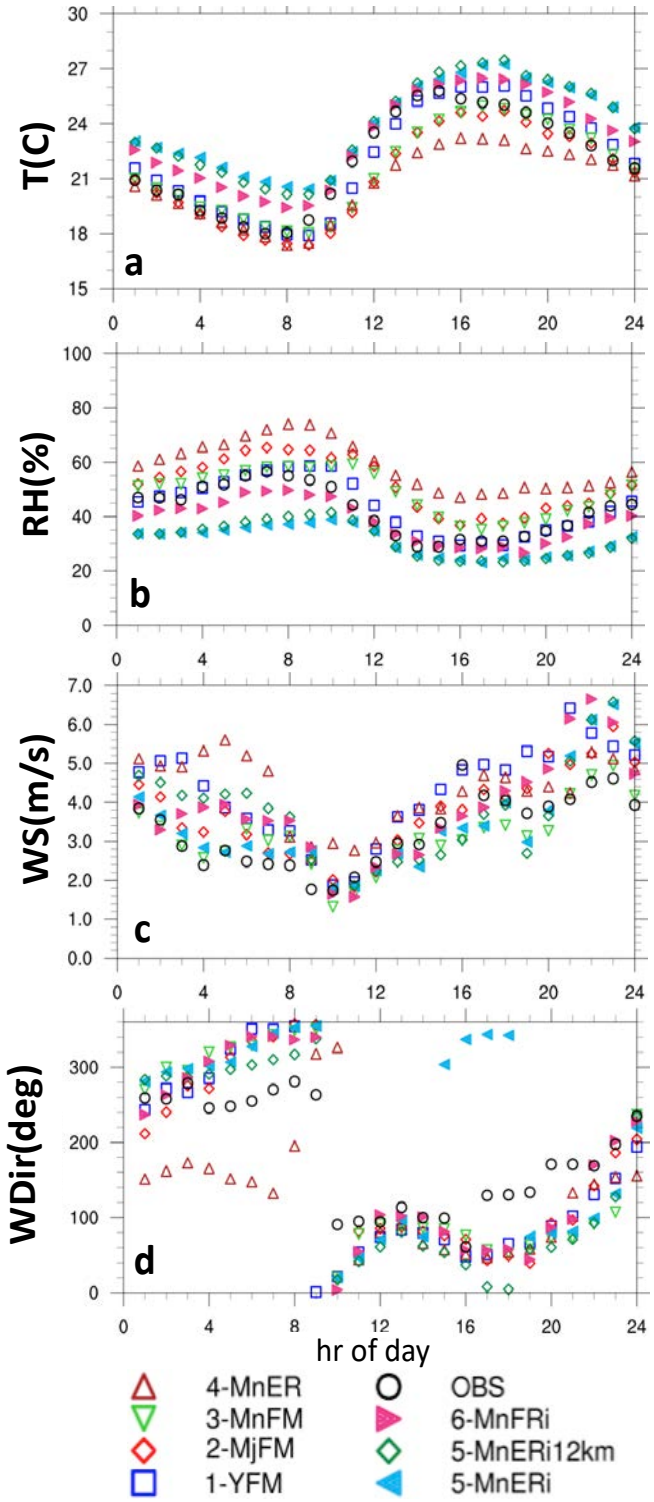

Figure 2-2. Average diurnal cycle of temperature (a), relative humidity (b), wind speed (c) and wind direction (d) for all tests and observation at BAO 100m. Averages are calculated for Aug 1 to 15, 2014

Table 2-3. Summary of model performance in capturing temperature (T) and Relative Humidity (RH) at BAO 100m during 1 to 15 August 2014

100m		PBL			Met IC and BC		Initialization		Horizontal resolution	
T(C)	OBS	PBL1	PBL2	PBL3	Met5	Met6	Init4	Init5	Hor5	Hor5 12km
Mean	22.0	22.2	21.1	21.5	23.9	23.2	20.7	23.9	23.9	23.9
R		0.9	0.8	0.8	0.8	0.8	0.6	0.8	0.8	0.8
RMSE		1.9	2.1	2.0	2.7	2.2	3.1	2.7	2.7	2.7
MAE		1.4	1.7	1.7	2.2	1.6	2.5	2.2	2.2	2.1
MB		0.2	-0.9	-0.5	1.9	1.2	-0.3	1.9	1.9	1.9
NMB(%)		0.8	-3.9	-2.3	8.6	5.4	-6.0	8.6	8.6	8.6
RH(%)	OBS	PBL1	PBL2	PBL3	Met5	Met6	Init4	Init5	Hor5	Hor5 12km
Mean	42.3	43.7	51.8	48.9	31.1	38.5	58.9	31.1	31.1	31.5
R		0.7	0.6	0.5	0.5	0.5	0.4	0.5	0.5	0.6
RMSE		11.9	16.3	14.7	16.7	13.6	25.9	16.7	16.7	16.0
MAE		9.2	13.5	12.3	12.8	10.3	21.2	12.8	12.8	12.0
MB		1.5	9.5	6.6	-11.2	-3.8	16.6	-11.2	-11.2	-10.8
NMB(%)		3.5	22.5	15.6	-26.5	-8.9	39.2	-26.5	-26.5	-25.4

Wind patterns vary significantly from daytime to nighttime. During the day, wind primarily blows from the east towards the Rocky Mountains with a slight southerly component. During the night, this pattern switches to predominantly westerly winds bringing cooler air to lower terrain. Wind measurements at the BAO at different altitudes (10m, 100m, 300m) can help us better understand the wind pattern at higher model levels. Table 2-4 includes mean and standard deviation of daytime and nighttime wind fields in the simulations and the observations at 100m. Results for the 10m and 300m level at BAO during 1 August 2014 to 15 August 2014 are included in Table Appendix 4 and Table Appendix 5, respectively. In addition to BAO, we investigated the wind sensitivity to physical parametrizations at two other sites that are close to oil and NG operations, WC tower and PAO (Figure Appendix 5). At BAO, higher wind speeds were measured at higher elevations which is captured by the model. Overall, most simulations show skill in capturing diurnal cycles of wind speed and direction with better agreement with observations for daytime (Table 2-4, Table Appendix 4, and Table Appendix 5). Overall, the model runs show fairly good performance in capturing temperature, relative humidity, and wind

fields, especially for daytime. A higher sensitivity to the physical parametrization was observed for nighttime.

Table 2-4. Summary of model performance in capturing wind speed and direction at BAO 100m during Aug 1-15, 2014

			PBL			Met IC & BC		Initialization		Horizontal Res.	
Day - 100m		OBS	PBL1	PBL2	PBL3	Met5	Met6	Init4	Init5	Hor 5	Hor5-12km
Wind Speed	Mean	3.2	3.8	3.4	2.7	2.9	3.2	3.8	2.9	2.9	2.8
	STD	2.0	2.1	2.3	1.6	1.6	1.8	2.9	1.6	1.6	1.5
Wind Direction	Mean	117.8	62.9	64.0	66.8	33.9	59.6	55.9	33.9	33.9	41.1
	STD	71.1	48.8	63.4	56.3	73.1	75.9	74.8	73.1	73.1	67.7
Night – 100m		OBS	PBL1	PBL2	PBL3	Met5	Met6	Init4	Init5	Hor 5	Hor5-12km
Wind Speed	Mean	3.4	4.7	4.1	3.6	4.0	4.4	4.9	4.0	4.0	4.7
	STD	1.8	2.3	2.8	2.5	2.5	2.3	2.9	2.5	2.5	3.2
Wind Direction	Mean	233.1	114.1	268.5	349.8	331.4	292.2	155.6	331.4	331.4	303.9
	STD	70.6	97.1	89.4	86.8	87.3	77.1	85.2	87.3	87.3	85.1

Ethane is predominantly emitted from oil and NG production sites (Helmig et al., 2016; Xiao et al., 2008) and is a valuable chemical tracer to study the transport patterns of oil and NG emissions. To evaluate the impact of vertical mixing intensity on the distribution of pollutants, we compared the vertical distribution of ethane concentrations between the simulations. Figure 2-3 shows the diurnal cycle of averaged vertical cross section of ethane concentrations at PAO with measured PBL height for each simulation.

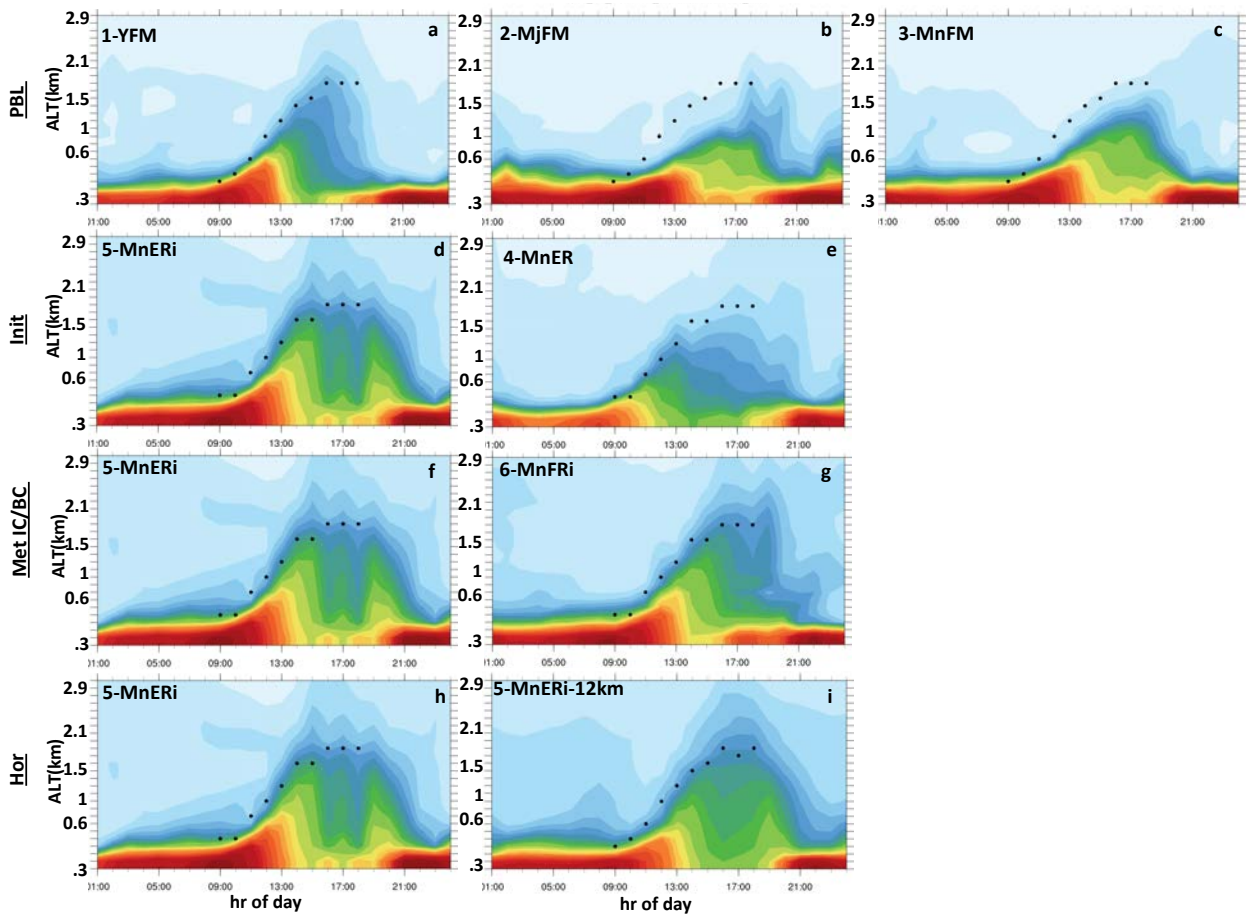

Figure 2-3 Cross section of modeled ethane at PAO and measured PBL height (black dots) averaged from August 1 to 10, 2014 (a to i). j, k, and l show diurnal evolution of PBL in all simulations at PAO (j), Fort Collins (k), and Golden-NREL (l) sites and measured PBLH (during daytime)

Complex local topography can cause localized transport patterns in the domain, which cannot be resolved at the model's 4 km x 4 km horizontal resolution. Pfister et al. (2017) discuss the impacts of the complicated wind patterns in the NFR and the limitations of WRF-Chem simulations in capturing the transport during FRAPPÉ campaign in details. To reduce the impact of localized influences on the sensitivity analysis we use airborne measurements which better represent the regional picture. Evaluation of modeled ethane concentrations with aircraft data provides information on the impact of different configurations on the transport of oil and NG emissions. Whisker plots of ethane concentrations at different elevations along the C130

morning and afternoon flights are shown in Figure 2-4. This plot limits the C130 observation to the NFR region (east of -105.2 longitude) to reduce transport errors, and it separates observations collected during 9:00 to noon (AM flights) and noon to 18:00 (PM flights) to account for the diurnal changes in PBLH. For this comparison, hourly model output has been interpolated to the time and location of each 1-minute average observation. Lower concentrations of ethane were measured during the PM flights compared to AM flights because of the higher PBLH and stronger vertical mixing in the afternoon (Figure 2-3). Table 2-5 summarizes the mean and NMB of ethane concentration for all simulations using ethane airborne measurements. In all simulations, the ethane concentrations are under-predicted by up to 3.3 ppb (NMB ranges between -63% to -42%) for the C130 AM flights and up to 1.7 ppb (NMB ranges between -47.6% to -29.5%) for the C130 PM flights. Overall, measured ethane concentrations, absolute biases, and absolute NMBs are higher for C130 AM compared to C130 PM. However, the differences between variability in NMBs for C130 AM and C130 PM are small i.e., 21% and 18.1%.

Table 2-5. Ethane mean, NMB, and NMB variability from C130 and P3 BAO and PAO airborne measurements below 2000m and the corresponding model values

			C130 - NFR		P3 - BAO		P3- PAO	
			AM	PM	AM	PM	AM	PM
	OBS	Mean (ppb)	5.2	3.5	12.4	4.9	18.6	8.7
PBL	PBL1	Mean (ppb)	3.0	1.8	8.5	3.9	7.8	2.6
		NMB (%)	-43.1	-47.6	-31.3	-21.4	-58.0	-69.7
	PBL2	Mean (ppb)	3.0	2.4	9.1	4.5	7.9	5.4
		NMB (%)	-43.1	-32.4	-26.5	-7.6	-57.3	-37.3
	PBL3	Mean (ppb)	2.8	2.5	8.7	4.9	10.4	4.2
		NMB (%)	-47.1	-29.5	-30	0	-44.0	-51.5
	All PBL	NMB var. (%)	4.0	18.1	4.8	21.4	14.1	32.4
Init.	Init4	Mean (ppb)	1.9	2.2	5.2	2.7	3.6	2.4
		NMB (%)	-63.0	-37.8	-57.8	-45.7	-80.5	-72.9
	Init5	Mean (ppb)	2.7	2.1	7.5	5.5	8.7	6.1
		NMB (%)	-47.9	-40.1	-39.7	11.6	-53.2	-30.0
	All Init	NMB var. (%)	15.1	2.3	18.0	57.3	27.3	42.8
Met IC & BC	Met5	Mean (ppb)	2.7	2.1	7.5	5.5	8.7	6.1
		NMB (%)	-47.9	-40.1	-39.7	11.6	-53.2	-30.0
	Met6	Mean (ppb)	3.0	1.9	7.0	4.5	7.9	4.0
		NMB (%)	-42.0	-45.0	-43.5	-9.0	-57.3	-53.9
	All Met	NMB var. (%)	5.9	4.9	3.7	20.6	4.2	23.9
Hor. Res	Hor5	Mean (ppb)	2.7	2.1	7.5	5.5	8.7	6.1
		NMB (%)	-47.9	-40.1	-39.7	11.6	-53.2	-30.0
	Hor5-12km	Mean (ppb)	2.6	2.0	5.7	3.8	5.7	3.9
		NMB (%)	-50.2	-43.3	-54.2	-21.6	-69.4	-55.1
	All res.	NMB var. (%)	2.3	3.2	14.4	33.3	16.2	25.1
Emiss	Em7	Mean (ppb)	2.8	2.2	7.6	5.3	9.1	6.0
		NMB (%)	-47.1	-38.1	-38.6	7.3	-50.8	-31.2
	Em8	Mean (ppb)	5.1	3.9	14.6	10.1	17.5	11.4
		NMB (%)	-2.9	11.7	17.6	106.1	-5.5	31.8
	All emiss	NMB var. (%)	44.3	49.9	56.3	98.9	45.3	62.9

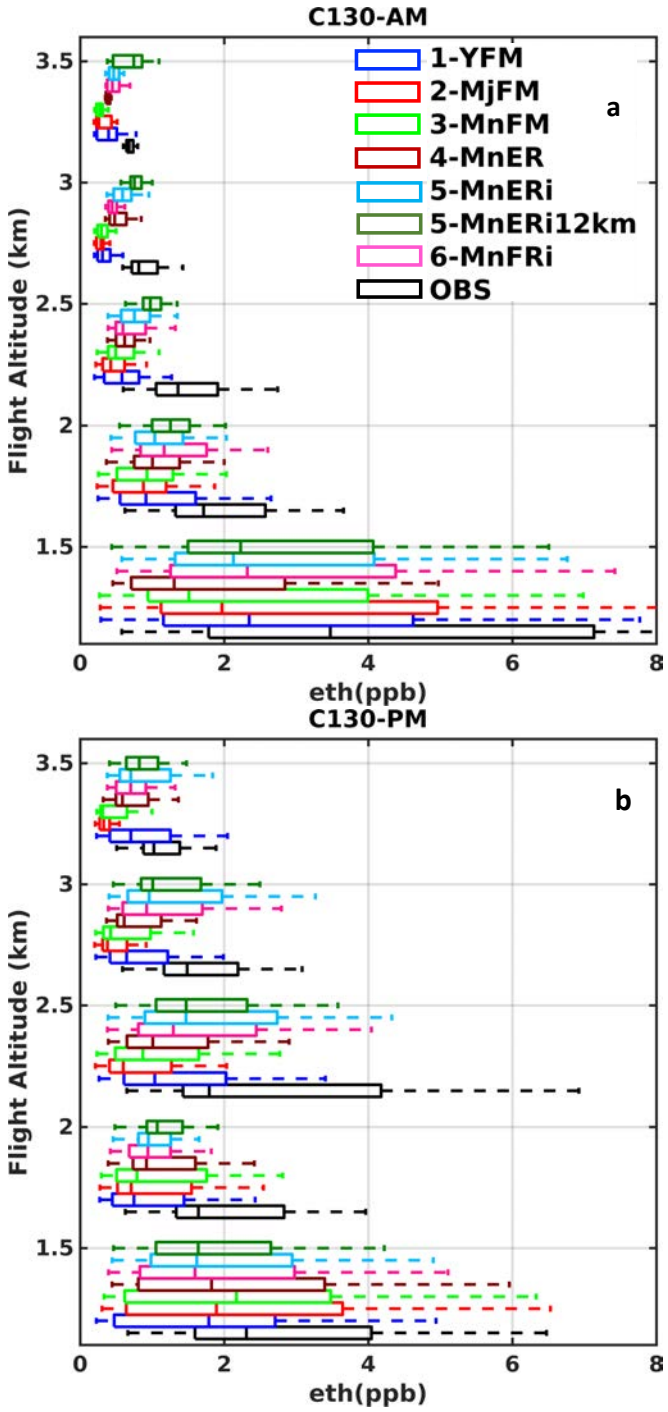

Figure 2-4. Vertical distribution of simulated and measured ethane in the NFR area separated by the flight time. (a) C130-AM 9am to noon observation and the corresponding model values. (b) C130-PM noon to 6pm observation and the corresponding model values

Measurements from P3 spirals focus on smaller regions and can capture the impact of local emissions. Figure 2-5 compares the vertical distribution of measured ethane concentrations against the corresponding model values (interpolated to time and location of each 1-min average observation) for all the simulations at BAO and Platteville (PAO) spirals. Both sites are located close to oil and NG sources (Figure 1), however urban emissions from Denver region can reach BAO (Pfister et al., 2017a). Similar to C130 observations, we illustrate the morning and afternoon data separately. Mean concentrations of up to 18.6 ppb (SD 2.8 ppb) were measured by P3 aircraft, but these high values were not captured by the model and resulted in biases up to -14.9 ppb (NMB of -80.5%) at PAO spirals and biases up to -7.16 ppb (NMB of -57.8%) at BAO spirals. Similar to C130 flights, higher measured ethane concentrations, absolute biases, and NMBs are observed for P3 AM flights compared to PM flights. Higher absolute biases and larger variance at lower altitude in AM flights and can be due to larger uncertainties in capturing morning evolution of PBL. Variability in NMBs across simulations are greater in the PM spirals (42.8% at PAO and 57.3% at BAO) compared to AM spirals (36.5% at PAO and 31.3% at BAO).

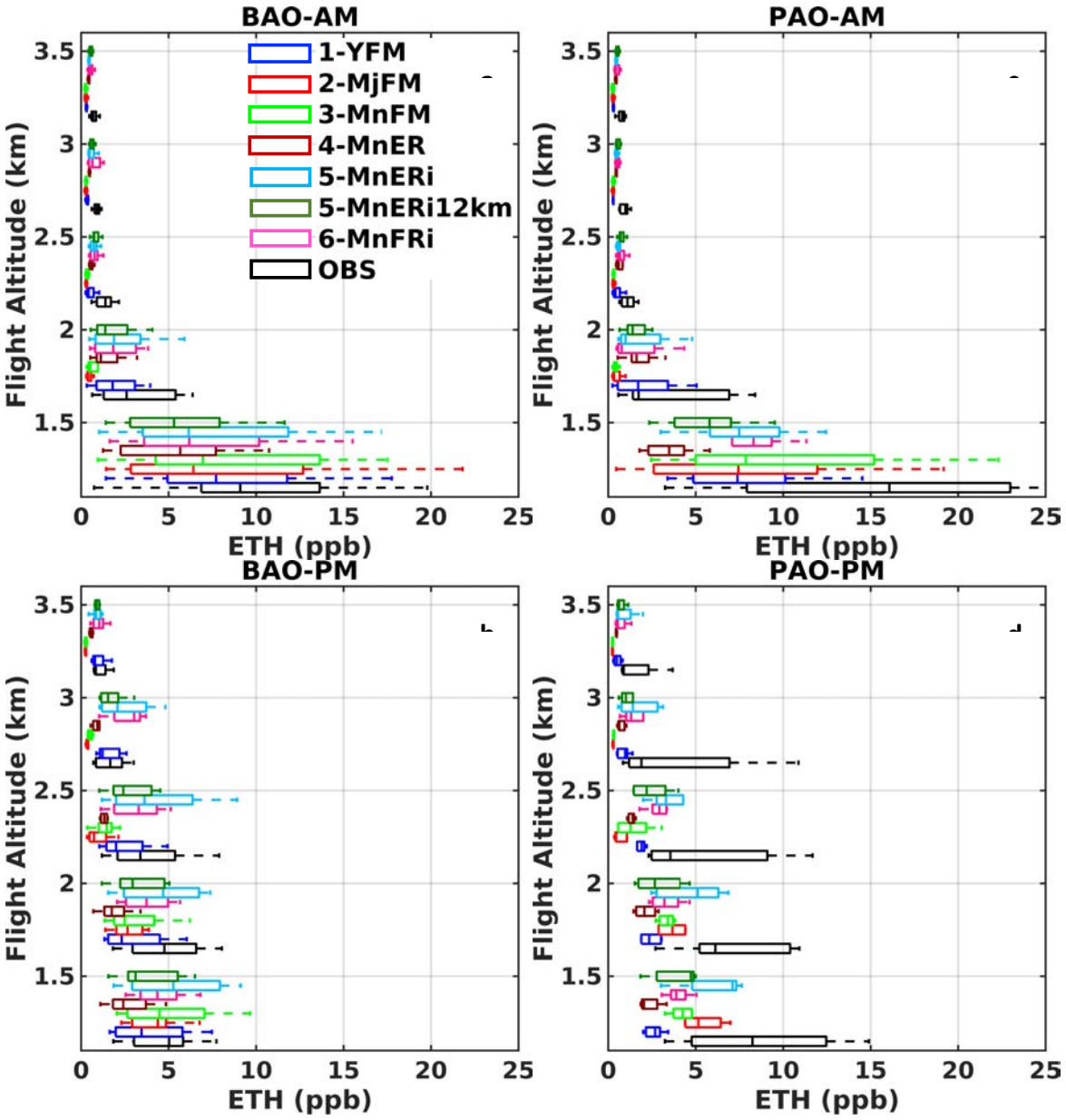

Figure 2-5. Vertical distribution of ethane at PAO (a and b) and BAO (c and d) site measured during P3 spiral flights and the corresponding model values. Flights are separated by the flight time. a and c show P3-AM that include 9am to noon observation and the corresponding model values. b and d show P3-PM that include noon to 6pm observation and the corresponding model values

While the model shows difficulty in representing the absolute magnitude in ethane concentrations in all simulations at lower altitudes, most simulations capture the changes in variance of ethane concentrations from lower to higher altitudes well especially for the C130 and P3 BAO flights. The C130 flights covered a larger region with varying flight patterns across the

NFR, thus less variability in the modeled ethane concentrations was observed compared to the P3, which flew a repetitive pattern and the repeated spirals over the key surface locations reflect a higher influence from localized emissions.

2.3.2 Sensitivity to planetary boundary layer parametrization

We evaluated the sensitivity of WRF-Chem meteorological fields and ethane concentrations to a non-local (YSU) and two local (MYJ and MYNN3) PBL schemes in PBL1, PBL2, and PBL3 simulation, respectively. Table 2-2 includes details on simulation configurations. Temperature at BAO changed little between the different PBL schemes and the model agrees with observations (Figure 2-2). At all three altitudes, PBL1 had a small positive bias (errors less than 1°C) while PBL2 and PBL3 had a small negative bias (errors less than 1°C) (Table 2-3 and Table Appendix 2). Relative humidity differed slightly between local and non-local PBL parametrizations. PBL1 captured relative humidity well, especially at lower altitudes (mean bias of 0.38%, 1.47%, and 4.93% for 10m, 100m, and 300m respectively). PBL2 and PBL3 both over-predicted relative humidity at all altitudes. The mean bias for PBL2 and PBL3 ranged between 11.12% to 14.78% and 6.61% to 9.55%, respectively.

At all altitudes of BAO, PBL1 predicted higher wind speeds than observed as well as PBL2 and PBL3 (Figure 2-2, Figure Appendix 1-3). Wind direction does not vary significantly between PBL1, PBL2, and PBL3 at BAO tower and the model missed the southerly component of afternoon winds. Figure Appendix 4 shows the 10m average wind speed (during 1-August to 11-August) in PBL1, PBL2, and PBL3 for daytime and nighttime and compares it with measurements. Higher daytime wind speed was predicted by PBL1 in the Colorado Eastern plains, especially north of Denver and close to oil and NG operations. Figure Appendix 5 shows the averaged diurnal cycle of wind speed and wind direction at WC Tower and PAO (sites close

to oil and NG operation). At WC tower and PAO, PBL2 and PBL3 better captured the southerly component of afternoon winds compared to BAO.

Each PBL scheme in the WRF model uses different diagnostics to determine the PBLH. To have a consistent comparison of PBL height in the three simulations, we used the 1.5-theta-increase method to estimate PBL height. In this method, PBLH is the lowest altitude where the difference between minimum potential temperature and potential temperature is greater than 1.5 K (Hu et al., 2010; Nielsen-Gammon et al., 2008). Figure 2-6 shows the diurnal evolution of PBLH as calculated using the 1.5-theta-increase method in the simulations. Observed PBLH at the PAO, Fort Collins (FC), and Golden-NREL sites were retrieved from micro-pulse Lidar backscatter profiles using Covariance Wavelet Transform (CWT) (Compton et al., 2013). PBLH in the PBL1 simulation is greater than either PBL2, PBL3, or observations, and the bias is largest in the afternoon. Figure 2-3 (a, b, and c) shows PBL1 distributed ethane higher into the atmosphere and more dilution resulted in lower ethane concentration within the PBL. Figure Appendix 6 shows, on average, up to 5 ppb higher surface ethane concentrations in simulations based on local PBL schemes (PBL2 and PBL3) compared to the simulation based on non-local PBL scheme (PBL1).

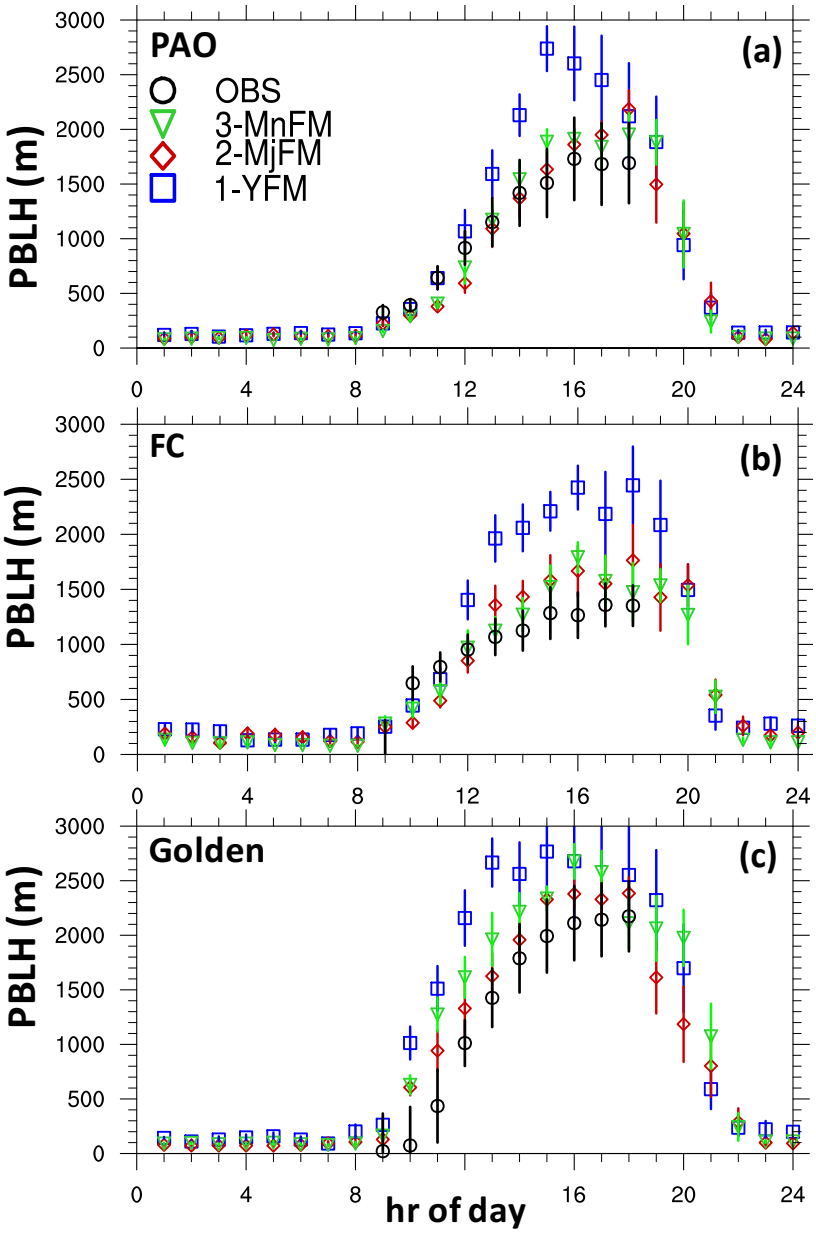

Figure 2-6. Diurnal evolution of PBL in MYJ, MYNN3, and YSU schemes at PAO (a), Fort Collins (b), and Golden-NREL (c) sites. PBLH was measured using micro-pulse Lidar backscatter profiles during the daytime. Error bars represent the standard error

The high bias in temperature, wind speed, and PBLH in PBL1, non-local PBL scheme, suggests a strong vertical mixing that is more defined in the Colorado Eastern plains and close to the oil and NG activities. The local PBL schemes (i.e. PBL2 and PBL3) predict cooler and moister climates and lower PBLH, which indicates less vertical mixing. This is consistent with previous

works that compared local and non-local PBL schemes in the WRF model (Angevine et al., 2012; Hu et al., 2010).

The comparison between C130 airborne measurements and modeled ethane concentrations across the NFR, as illustrated in Figure 2-4, shows biases between -2.5 ppb and -2.3 ppb for AM flights and between -1.7 ppb and -1 ppb for PM flights. Lower NMB variability (4%) was observed in the C130 AM with NMB ranging from -43.1% to -47.1% compared to C130 PM with NMB variability of 18% and NMB ranging from -29.5% to -47.6%. Similar to the C-130 comparison, Figure 2-5, the simulations did not capture the high ethane values measured during P3-BAO and P3-PAO spirals. The sensitivity of modeled ethane profiles to the PBL scheme is larger in P3 flights compared to C130 flights, with NMB variability of 14.1% ranging from -58% to -44% for PAO AM flights and NMB variability of 32.4% ranging from -37.3% to -69.7% for the PAO PM flight. On average PBL1 predicted higher ethane concentrations during AM flights at lower altitudes compared to PBL2 and PBL3 (Figure 2-3). Faster evolution of morning PBL and stronger vertical mixing in PBL1 lofted pollutants (including ethane) higher into the atmosphere in the morning (Figure 2-6). The rapid growth of morning PBL in PBL1 resulted in higher concentration of ethane at higher altitudes (0.5 to 2 km) compared to PBL2 and PBL3.

2.3.3 Sensitivity to re-initialization

We investigated the impact of daily initialization of meteorological fields on the model performance in capturing the transport of pollutants. For this, we conducted a sensitivity simulation (Init5) in which each daily cycle started at 18 UTC from ERA-interim meteorological fields and ran for 30 hours. In the comparison free-running simulation, Init4, we initialized the model at the first time step using the ERA-interim model and ran the simulation from 24 July 2014 to 18 August 2014 freely. Physical configurations and meteorological and chemical initial

and boundary conditions kept the same for these two simulations (Table 2-2). Figure 2-2 shows an up to 3°C bias in nighttime temperature in Init5, but good agreement with the measured temperature during the day. Init4 showed better skill in capturing nighttime temperature compared to Init5, but predicted the lowest daytime temperature among all the simulations with a bias up to -3°C. On average, the NMB of the temperature at BAO100m is between 8.6% in Init5 and -6.0% in Init4 (Table 2-3), which is the largest variability in NMB temperature across the simulations. Similar to the temperature, relative humidity showed a strong sensitivity to re-initialization. Init4 predicted the highest relative humidity, with NMB of 39.2% and Init5 predicted the lowest relative humidity, with an NMB of -26.5% among the simulations at BAO 100m (Table 2-3). Nighttime wind direction at BAO (Figure 2-2), PAO, and WC tower (Figure Appendix 2) had a strong southerly component in Init4 compared to Init5 and observations. In addition, Init4 predicted higher wind speeds compared to BAO measurements (Figure 2-2) and Init5. Figure 2-7 shows on average higher wind speed at 10m altitude across the domain in Init4 compared to Init5 and measurements at both daytime and nighttime.

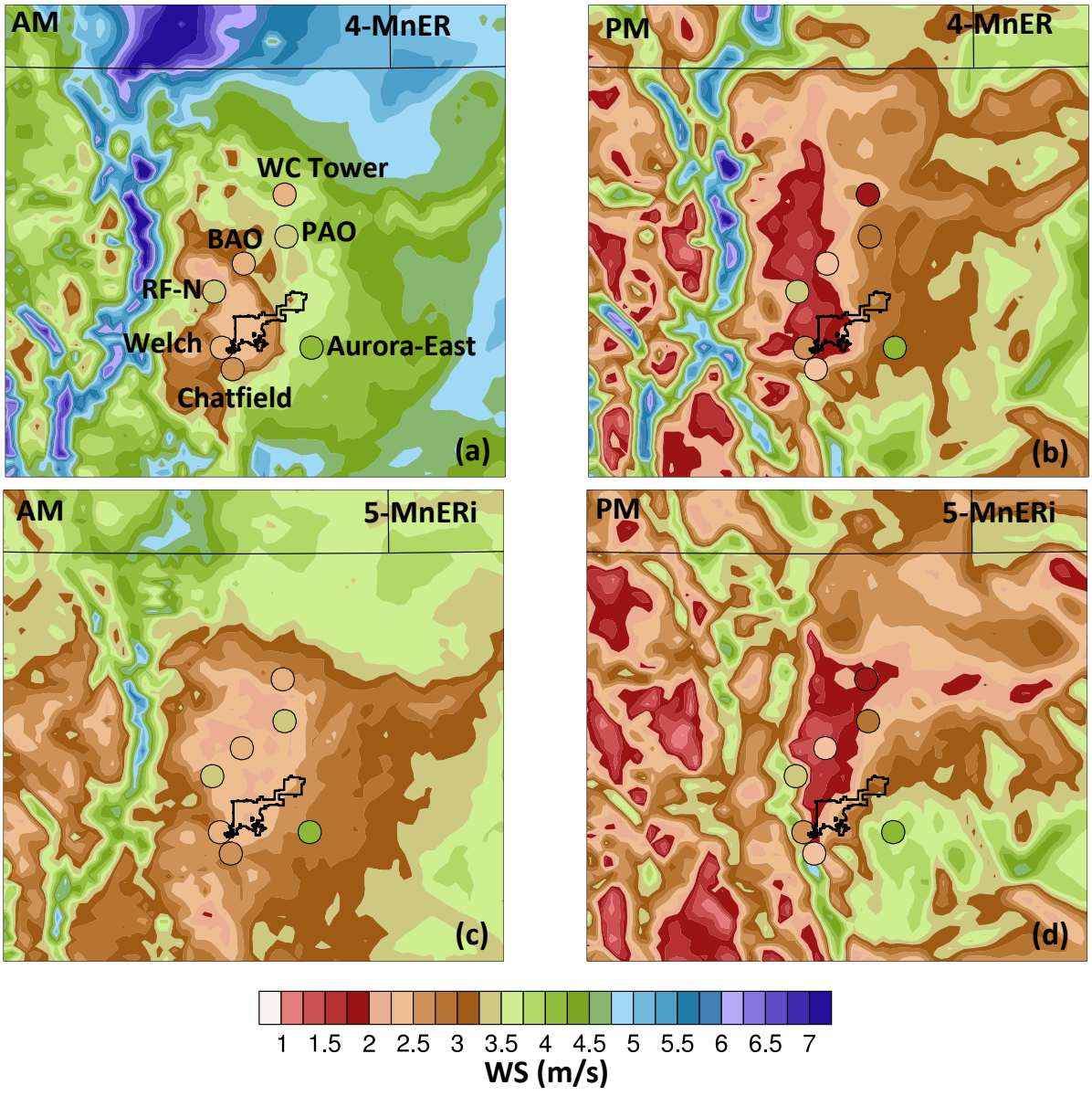

Figure 2-7 Measured (circles) and modeled (color contour) wind speed at 10m captured by Init4 (a and b) and Init5 (c and d) from Aug 1 to 11, 2014 and separated by daytime vs nighttime

When compared to C130-AM ethane concentrations (Figure 2-4), Init4 predicted the lowest ethane concentrations (a bias of -3.3 ppb and NMB of -63%) among all the simulations. This is likely due to the high bias in of wind speed in this simulation which resulted in lower concentrations of ethane (Figure 2-7). The ethane bias is ~-2.5 ppb and NMB is -47.9% in Init5 during C130-AM. Concentrations during the C130-PM flights showed a weak sensitivity to re-

initialization with NMB ranging from -37.8% (Init4) to -40.1% (Init5). For the P3-BAO and P3-PAO spirals in both AM and PM flights, Init4 had the lowest ethane values compared to all the other simulations and compared to observations (Figure 2-5). This resulted in the largest NMB variability across the simulations. During PAO AM, NMB ranges between -80.5% for Init4 and -53.2% for Init5 (NMB variability of 27.3%) and during PAO PM, NMB ranges between -72.9% for Init4 and -30.0% for Init5 (NMB variability of 43.9%).

2.3.4 Sensitivity to meteorological initial and boundary condition

We tested the performance of changing the meteorological initial and boundary conditions by comparing simulations using ERA-Interim (Met5) with simulations using NCEP-FNL (Met6). As was done for Met5, we initialized meteorological fields with the re-analysis fields every day allowing for a 6-hour spin-up. To prepare meteorological initial and boundary conditions from global models, WRF interpolates these outputs to the designed domains. Figure Appendix 7 illustrates the differences between ERA-interim and NCEP-FNL model outputs interpolated to the outer domain at the lowest model level and averaged during August 1 to 15, 2014. Overall, the wind speed predictions by these two global models are very similar with slightly (less than 1 m/s) higher prediction by NCEP-FNL. ERA-interim and NCEP-FNL had larger discrepancies in temperature and relative humidity throughout the domain. Comparison with BAO observations (not shown) indicates similar performance for both models with somewhat lower temperature and higher relative humidity in ERA-interim compared to NCEP-FNL. These discrepancies did not have a large impact on temperature and relative humidity in the WRF-Chem simulation, however. Figure 2-2 and Figure Appendix 1-3 indicate that the performance of the two simulations is comparable in capturing temperature and relative humidity with a better agreement with measurements during the day. Met5 had slightly higher temperature and lower relative humidity compared to Met6 and compared better to measurements especially during the night.

This is because WRF-Chem only uses the global values as the initial and boundary values and resolves for atmospheric variables such as temperature and relative humidity in high resolution based on physical parametrizations set for the simulation.

Comparison of ethane measurements by the C-130 and P3 aircraft with Met5 and Met6, shown in Figure 2-4 and Figure 2-5, respectively, also reflects an overall low sensitivity of the model performance to meteorological initial and boundary condition for both AM and PM flights. High sensitivity was observed during P3-PAO PM flight with ethane NMB variability of 23.9% where Met5 had a bias of -2.6 ppb (NMB of -30%) and Met6 had -4.7 ppb (NMB of -53.9%).

2.3.5 Sensitivity to horizontal resolution

The two nested domains in simulation Hor5 had a horizontal resolution of 12 km × 12 km (coarse) and 4 km × 4 km (fine). The one-way nesting method was used to prevent any feedback from the higher resolution inner domain on the outer domain. This means that while the outer domain provides the boundary conditions to the inner domain, the higher resolution fields from the inner domain do not alter the outer domain fields. To compare the impact of horizontal resolution, we compared the performance of the coarse domain with the fine domain in the same simulation (5Hor). Temperature and relative humidity did not show significant sensitivity to the horizontal resolution at BAO and PAO, as neither did surface winds at BAO (Figure 2-2), PAO, and WC tower (Figure Appendix 4). At 100m and 300m altitudes at BAO, the coarse domain predicted higher nighttime wind speed compared to the fine domain and the measurements.

Averaged ethane concentrations along the C130 flights (Figure 2-4) do not vary significantly with horizontal resolution. However, higher differences are observed for the P3 spirals. This might be due to the C130 flights covering a larger area and, in parts, averaging out the impact of horizontal resolution, whereas the P3 spirals capture small-scale transport patterns in the domain

more effectively. For the P3 spirals (Figure 2-5), the ethane NMB during BAO PM is +11.6% for the fine domain and -21.6% for the coarse domain. These values are -30% and -55.1% during PAO PM flights, respectively.

2.3.6 Oil and NG emission in the NFR

We assessed the performance of the model in capturing oil and NG emissions by focusing on ethane, which is mostly emitted from oil and NG emission sources, and on species with multiple emission sources such as CO and other VOCs. To investigate the contribution of oil and NG emissions to NFR air quality, we ran two additional simulations: in the one, the emissions are based on the NEI-2011 as provided (base simulation or Em7), in the other we doubled the oil and NG emissions (perturbed simulation or Em8).

Figure 2-8 shows the C130 PM measurements and bias limited to altitudes below 2000m and Figure 2-9 displays scatterplots of measured to modeled species concentrations limited to NFR, below 2000m with measured ethane greater than 2ppb. Figure 2-8a and b illustrate high values of ethane concentrations in the vicinity of oil and NG facilities which were not captured by the model resulting in low biases. As can be expected, the simulated ethane concentrations show a high sensitivity to changes in the oil and NG emissions (Figure Appendix 8). The highest sensitivity was observed for measurements taken over regions close to oil and NG sources, such as the P3-PAO spirals. Ethane biases between Em7 and Em8 varied from -9.4 ppb to -1 ppb (NMB from -50.8% to -5.5%) during P3-PAO AM, and from -2.7 ppb to +2.8 ppb (-31.2% to +31.8%) during P3-PAO PM. Doubling oil and NG emissions lowered the absolute bias during the AM flights (NMB from -50.8% to -5.5%), but resulted in an overestimation of ethane concentrations during the PM flights (NMB from -31.2% to +31.8%). One possible reason for the difference between AM and PM biases might be an incorrect representation of the diurnal

variation of ethane emission rates in the NEI-2011. An inverse modeling technique, as will be subject of further studies, can be used to calculate optimal scaling factors for hourly ethane emissions with the goal to minimize the discrepancies between model and measurement.

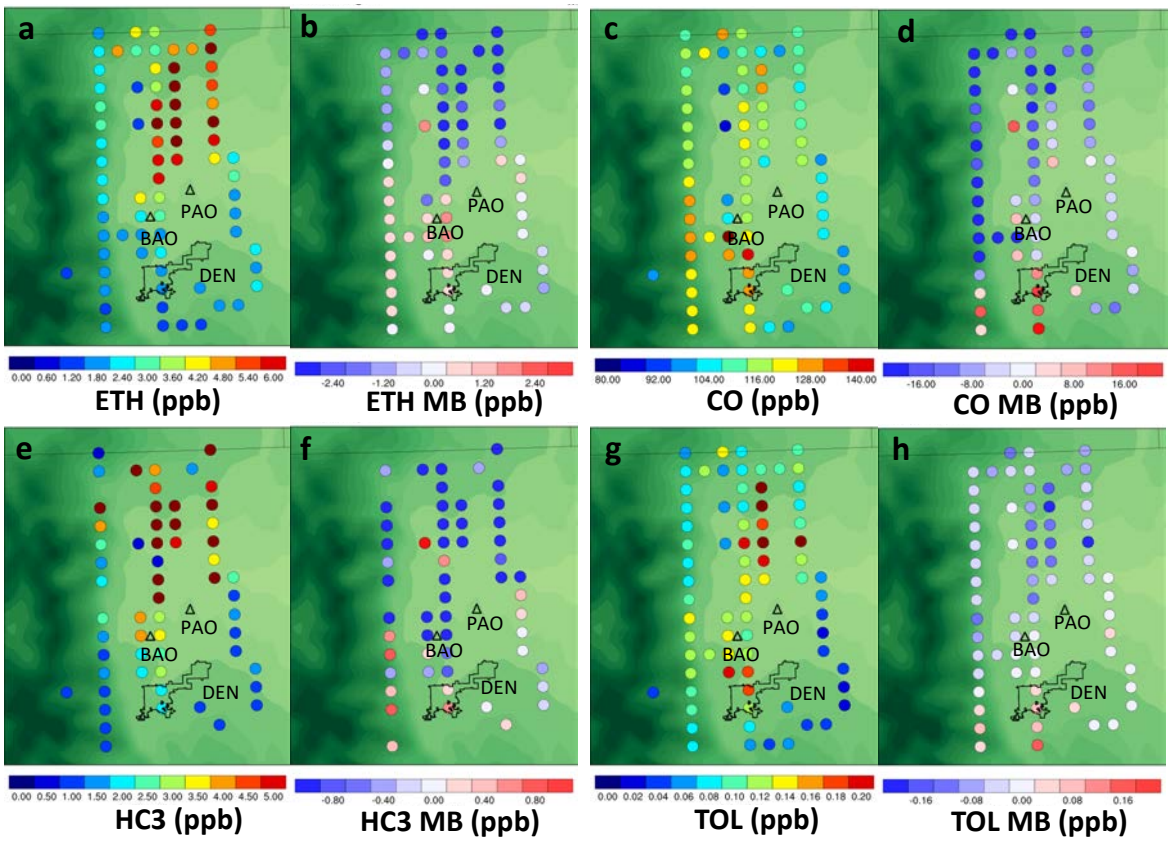

Figure 2-8. Mean and mean bias ethane concentration (a and b), CO (c and d), HC3 (e and f), and TOL (g and h) along the C130 PM flights are limited to measurements below 2000m agl and grids with more than 4 measurement points. The outline of Denver county and the locations of BAO and PAO are marked on the underlying terrain map

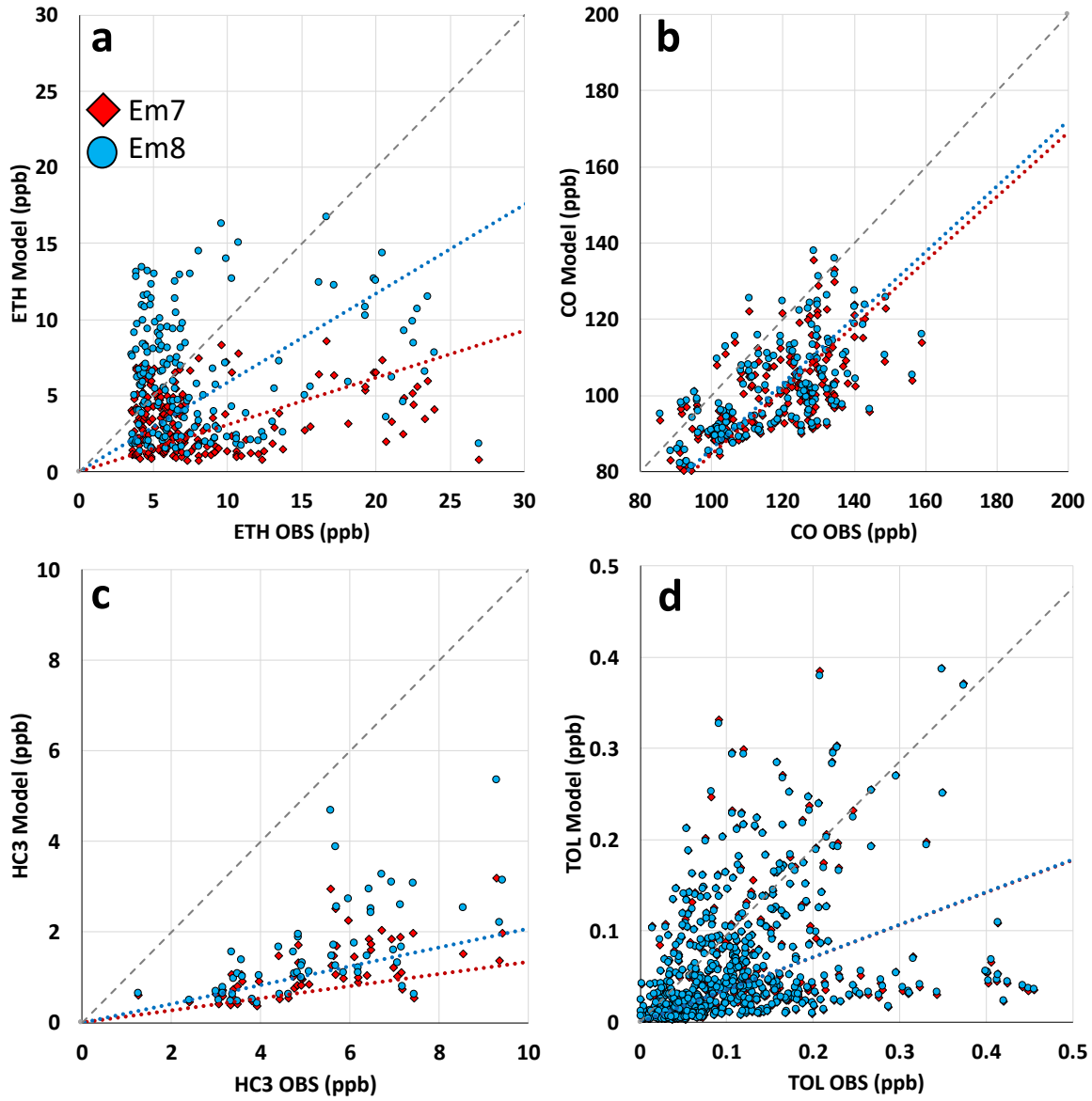

Figure 2-9. Scatter plot of measured vs. corresponding model values of ethane (a), CO (b), HC3 (c), and TOL (d) along the C130 PM flights limited to measurements in the NFR and below 2000m. Red diamonds represent the Em7 (base emissions) and blue circles represent Em8 (perturbed emissions). Red and Blue lines show the best fit using least square linear regression method for Em7 and Em8, respectively

CO is mostly emitted from combustion processes and is released from many different source sectors. Figure 2-8c shows CO enhancements over both Denver and oil and NG facilities. Biases along the C130 flight tracks (Figure 2-8d) show an over-prediction of CO over Denver and west of Denver and an under-prediction over the oil and NG facilities. The scatterplot in Figure 2-9b

reflects an overall low bias in modeled CO can be partly due to errors in capturing background CO. Doubling oil and NG emissions in Em8 only marginally increased the slope of the regression line indicating a low sensitivity of CO in the NFR to oil and NG emissions. This suggests that the source of the low bias in CO likely is related to other source categories and/or the model boundary conditions.

In the RACM chemical mechanism, alkanes such as propane, n-butane, isobutane, and acetylene (ethyne), and alcohols such as methanol and ethanol are lumped under the "HC3" group (Stockwell et al., 1990). We compared the simulated HC3 concentrations with the sum of measured chemicals in the HC3 group during C130 flights. Similar to ethane, the highest values of HC3 were measured over oil and NG facilities (Figure 2-8c). These enhancements were not captured in the model and resulted in low model biases (Figure 2-8f). Comparison of measured HC3 with modeled values from Em7 and Em8, Figure 2-9c, confirms the low bias of HC3 and shows some increase in the slope of the regression line in Em8 albeit less pronounced compared to ethane.

Toluene and benzene are lumped together in the RACM chemistry under "TOL" (Stockwell et al., 1990). We compared simulated TOL with the sum of toluene and benzene concentrations observed during the C130 flights. The transport sector is a strong source of toluene and benzene in the NFR as well as oil and NG activities. TOL enhancements were observed over oil and NG facilities and Denver with higher values associated with oil and NG emissions (Figure 2-8g). The model did not capture the enhancements in regions influenced by oil and NG emissions, but well captured TOL values over Denver (Figure 2-8h). TOL showed very low sensitivity to perturbed oil and NG emissions as shown in Figure 2-9d. TOL emissions from oil and NG sector in the emission inventory used in this study (NEI-2011) were very low thus doubling oil and NG

emissions did not increase TOL in the Em8. Similar to toluene and benzene, xylene enhancements were measured over oil and NG facilities and Denver. Model underestimated xylene enhancements over oil and NG activities and overestimated these enhancements over Denver. Em8 with doubled oil and NG emissions showed very similar performance to Em7 which indicates low emission rates of xylene from oil and NG sector in the NEI-2011 (not shown).

Figure 2-10 illustrates the HC3 to TOL ratio measured along the C130 PM limited to NFR region and altitudes below 2000m and the corresponding model values. Figure 2-10a shows oil and NG influenced points with enhanced measured ethane (concentrations greater than 2 ppb). HC3 to TOL ratios in oil and NG influenced locations show inconsistency between measured (HC3/TOL = 68) and Em7 modeled ratios (HC3/TOL = 22) which was improved in the Em8 (HC3/TOL = 40.9). However, doubling oil and NG emission still resulted in underestimations of HC3, TOL, and their ratios in this region. Figure 2-10b shows urban influenced points with low measured ethane (concentrations less than 2 ppb). Modeled HC3 to TOL ratios (7.3 for Em7 and 8.9 for Em8) in the urban influenced locations did not show large sensitivity to oil and NG emissions and agreed well with the measurements (10.2). In both oil and NG and urban influenced regions models predicted lower than measured Y-intercepts which was not improved in Em8. Figure 2-9c also confirms the low bias (about -2ppb) in background HC3 in the model. One reason for this offset can be underestimation in HC3 concentration in the boundary condition fields or leakage from the NG distribution system which was not captured in the model.

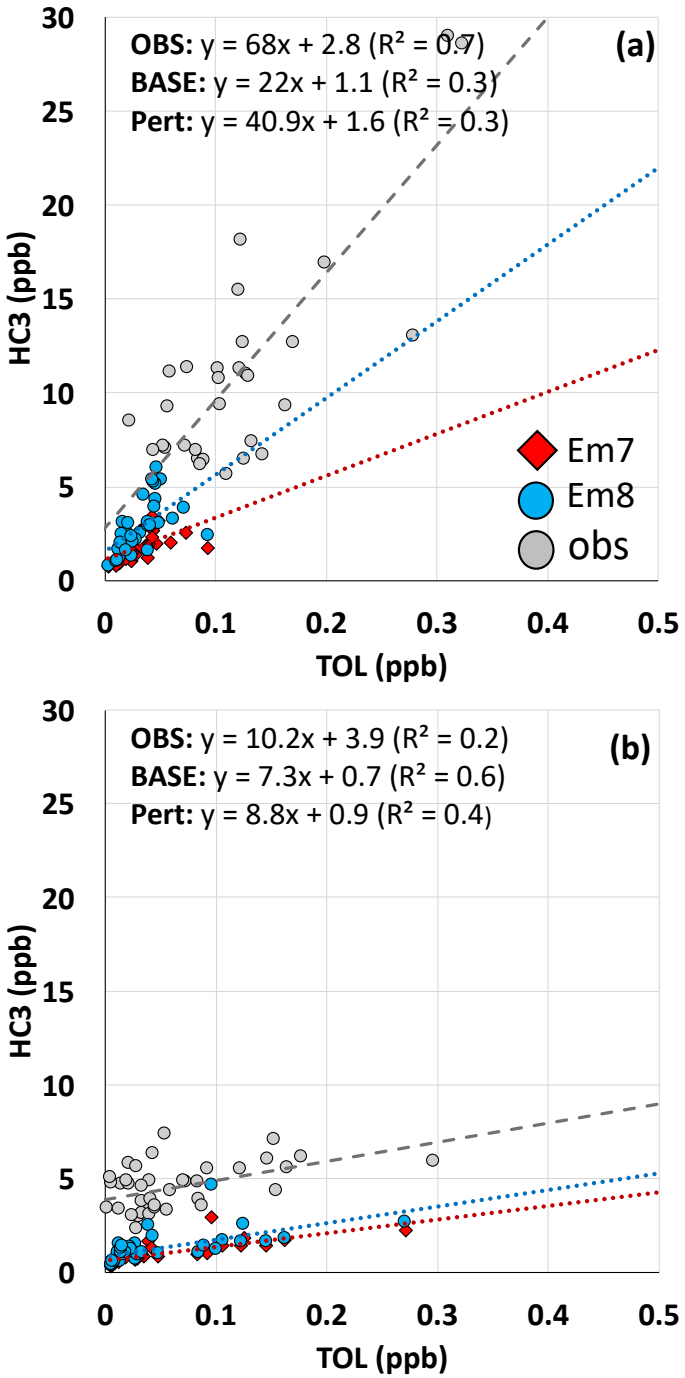

Figure 2-10.Sscatter plot of HC3 vs. TOL concentrations along the C130 PM flights limited to measurements in the NFR and below 2000m altitude. Plot (a) shows HC3 vs. TOL (when measured ethane is greater than 2ppb) for measurements and the corresponding model values. Plot (b) shows HC3 vs. TOL (when measured ethane is less than 2ppb) for measurements and the corresponding model values. Grey circles represent measurements, red diamonds represent the Em7 (base emissions), and blue circles represent Em8 (perturbed emissions). Grey, Red and Blue lines show the best fit using least square linear regression method for observations, Em7 and Em8, respectively

The results suggest that HC3, toluene, benzene, and xylene from oil and NG sector are significantly underestimated in the NEI-2011. The low model bias for these species is more pronounced compared to the low model bias in ethane (Figure 2-9). The inconsistency between these biases implies that the NEI-2011 emission ratios might need to be changed and HC3, toluene, benzene, and xylene oil and NG emissions would need to be increased by a larger factor than ethane.

2.4 Conclusion

We used WRF-Chem to understand the sensitivity of pollutant transport at a high horizontal resolution to different model configurations with the focus on oil and NG emissions. By conducting a range of different sensitivity simulations, we assessed the variability of meteorological variables such as temperature, relative humidity, and wind fields as well as of ethane concentrations (used as a tracer for the oil and NG sector) to different model configurations and parameterizations. The overall daily cycle of temperature and relative humidity was captured well in the simulations with NMB ranging from -3.9% to 11.1% in temperature and from 29.7% to 52.6% in relative humidity. All simulations showed good skill in capturing daytime wind fields but showed higher biases for nighttime wind speeds.

Table 2-5 summarizes the mean and NMB for ethane concentrations from C130 and P3 airborne measurements below 2000m agl and the corresponding model values for all sensitivity tests. Significant underestimation of ethane in all simulations– especially in regions close to oil and NG activities – with biases up to -14.9 ppb (NMB up to -80.5%) suggest that the emission inventory used (NEI-2011) under-predicts oil and NG emissions. NMB variability (Table 2-5) was used as a proxy for variability in the model performance caused by model configurations. NMB of the near-surface ethane concentration for aircraft flight patterns across sensitivity simulations varied by up to 57.3% for P3-BAO, by up to 42.8% for P3-PAO and by up to 21.1%

for C130 flights. The lower NMB variability during C130 flight can be due to the larger area coverage by this aircraft during the FRAPPÉ campaign and the irregular flight patterns. P3 spirals, covering smaller regions within the domain during repetitive flight patterns, focused more on the local emissions and smaller scale transport patterns and captured a larger ethane sensitivity to model configurations. The largest sensitivity occurred in the initialization test (comparing daily re-initialization with free-run simulation) with ethane NMB variability up to 57.3%, followed by the horizontal resolution test (comparing horizontal resolution of 12 km × 12 km with 4 km × 4 km) and the PBL parametrization test (comparing local with non-local PBL schemes) with ethane NMB variability up to 33.3% and 32.4%, respectively. To further investigate the performance of the model in capturing oil and NG emissions in the NFR we used a similar domain set-up with 12 km × 12 km and 4 km × 4 km horizontal resolution for outer and inner domains, respectively, daily re-initialization of meteorological variables with ERA-interim model, and MYNN3 PBL scheme.

We compared measured ethane, CO, lumped alkanes (HC3), lumped toluene and benzene (TOL), and xylene to corresponding modeled values and assessed the changes in the model performance when doubling oil and NG emissions. The model showed under-prediction of ethane with the original inventory and a strong sensitivity of ethane concentrations to oil and NG emissions. Doubling oil and NG emissions resulted in an improvement during AM flights and an overestimation of ethane during the PM flights which suggests possible incorrect representation of the diurnal variation of ethane emission rates in the NEI-2011. The model tends to overestimate CO over the Denver region and underestimates CO over the oil and NG region. Low sensitivity of CO to oil and NG emissions indicates that CO in the region is predominantly emitted from sources other than oil and NG. Enhancements of HC3, TOL, xylene over oil and NG facilities were not fully captured in the model and resulted in low biases. Doubling emissions

from oil and NG emissions improved the model performance in capturing HC3, but still resulted in a low model bias. Although high values of TOL and xylene were measured over oil and NG facilities, the model did not capture these enhancements in either the simulations with base NEI-2011 emissions or doubled oil and NG emissions. The inconsistency between the sensitivity of ethane, HC3, benzene, toluene, and xylene to the increase in oil and NG emissions and mismatch between VOC ratios in the model and measurement suggest that oil and NG emission rates in the NEI-2011 need to be scaled differently for these species. VOC ratios in the measurements can be used to update these ratios in the emissions inventory.

The presented results reflect the challenges that one is faced with when attempting to improve emission inventories by contrasting measured with modeled concentrations, either through simple direct comparisons or more advanced methods, such as inverse modeling. Any uncertainties that arise from the model configuration will translate into the derived emission constraints, and it is important to be aware of the uncertainties resulting from different model setups. The WRF-Chem simulations and knowledge gained from this study will be used to support inverse modeling studies aimed to improve estimates of emission from oil and NG sector in the NFR.

3 CONSTRAINING OIL AND NATURAL GAS EMISSIONS THROUGH A MULTIPLATFORM INVERSION

Abstract

We implemented a variational inversion technique to constrain hourly ethane emissions from oil and NG sector in Colorado. High-resolution (4km x 4km) WRF-Chem simulation along with airborne measurements of ethane were coupled to calculate the optimal scaling factor for ethane emission in NEI-2011v2. Tracers linked to hourly ethane emissions were added to the WRF-Chem model and showed that airborne ethane observations in the Northern Front Range (NFR) Colorado are dominantly influenced by the Denver-Julesburg (DJ) basin emissions released on the day of the measurement. Scaling factors up to 6 were calculated for the ethane emitted from the Wattenberg field. Overall, the inversion method estimated between 11% to 15% higher ethane emission rates in the DJ basin compared to the initial emission inventory (NEI-2011v2). Ethane to methane or other VOCs ratio in the measurements and the constrained ethane emission rates can be used to estimate the emission rates of these species and compare them to the official emission inventories.

3.1 Introduction

With the rapid increase in the unconventional oil and Natural Gas (NG) production higher than expected levels of air pollutants such as methane, VOC, and NOx have been observed in areas close to oil and NG facilities. The high concentrations of these chemicals measured in many studies at different scales and regions suggests the official emission inventories (e. g. EPA-GHGI and EDGAR) fail to capture the magnitude of emissions from unconventional operation (Brandt et al., 2014). The underestimation of emission inventories has raised concern regarding the climate implications of promoting NG as the “bridge fuel” (Alvarez et al., 2012; Howarth et al.,

2011; Levi, 2013; McJeon et al., 2014) and its impacts on the air quality and public health (Halliday et al., 2016; McKenzie et al., 2012). Studies show that methane leakage of higher than ~3% from NG systems can offset the climate benefits of replacing coal with NG (Alvarez et al., 2012; Wigley, 2011). Outdated Emission Factors (EF), super-emitters in the production systems, and rapid growth in the production facilities are some of the reasons for the underestimation (Brandt et al., 2014; Lyon, 2015; Zavala-Araiza et al., 2015).

Lyon (2015) classified emissions from NG facilities into three groups of vented emissions, fugitive emission, and incomplete combustion emissions (Lyon, 2015). Vented emissions are NG released intentionally due to safety, equipment design, or convenience. NG-powered pneumatic controllers are the largest sources of vented emissions in the US. In unconventional production during the well completion large amounts of NG can be released from the flowback water. Higher well density in unconventional production results in high amounts of methane and VOC emission (constituents of NG) from each well pad. In January 2015, the US EPA restricted almost all hydraulically fracture NG wells to use reduced emission completions (green completion) to capture the completion flowback gas (United States Government Publishing Office, 2015). Fugitive emissions are unintentional leakages from faulty equipment. The emission rates on such equipment can increase with equipment wear. Combustion emissions can occur during the flaring or operation of engines that combust NG. With high efficiency of flaring technology, the amount of NG emitted through this phase is relatively small. However, flaring can release Black Carbon (BC) and VOC into the atmosphere and impact the air quality (Prenni et al., 2016).

Methane is the primary constituent of NG and the second most important greenhouse gas after carbon dioxide (CO_2). Methane has a shorter effective lifetime (~ 12 years) than CO_2, but 37

times stronger radiative forcing (on a molar basis). Therefore, it has a stronger near-time climate impact in comparison with CO_2 (Alvarez et al., 2012). Methane global emissions are 4% of the global CO_2 anthropogenic emissions in a unit of carbon mass flux but contributes ~20% to additional radiative forcing in lower atmosphere since 1750 due to its strong radiative forcing (Saunois et al., 2016). Methane is a precursor to tropospheric ozone and contributes to tropospheric ozone production and background ozone which has severe impacts on human health, vegetation, and crops. High concentration of atmospheric methane has been observed by various measurement tools in areas with heavy NG operation (Karion et al., 2013; Kort et al., 2014; Miller et al., 2013; Pétron et al., 2014; Schneising et al., 2014; Turner et al., 2015; Zavala-Araiza et al., 2015). Using satellite observations, different studies have detected positive methane anomalies associated with oil and NG operation in the US (Kort et al., 2014; Schneising et al., 2014; Turner et al., 2015).

Besides methane, oil and NG activities release VOCs (constituents of NG) and NOx in significant amounts into the atmosphere. These air pollutants can directly impact the air quality via participation in photochemical production of ozone. Elevated levels of VOCs (such as ethane, propane, n-butane, i-pentane, n-pentane, and benzene) (Halliday et al., 2016; Pétron et al., 2014) and ozone (Ahmadov et al., 2015b; Field et al., 2015; Oltmans et al., 2014; Rappenglück et al., 2014) have been measured in the areas close to oil and NG operation sites. At the global scale, studies have reported a significant increase in the global concentration of ethane and propane in recent years due to increase in oil and NG activities in North America (Franco et al., 2016; Hausmann et al., 2016; Helmig et al., 2016; Kort et al., 2016).

Given the scale of NG development and the rapid growth in the NG production, many studies have focused on estimating the emission from NG facilities and investigating the impact of these

emissions on climate and air quality. To estimate the emissions, two methods of bottom-up and top-down are widely used. Bottom-up studies directly measure the concentration of the desired pollutant from devices or facilities before emissions are mixed in the atmosphere (Allen et al., 2013; Caulton, 2011; Harrison et al., 2011; Omara et al., 2016). While in top-down approaches atmospheric concentrations of different species are measured using different tools such as aircraft, tower, ground sampling, remote sensing, and satellite measurements (Karion et al., 2013, 2015; Miller et al., 2013; Peischl et al., 2016; Pétron et al., 2012, 2014; Townsend-Small et al., 2012). The atmospheric measurements are used along with a simple mass balance approach or sophisticated atmospheric transport model or chemical transport models (CTMs) to simulate the transportation of the pollutants and the chemical process in the atmospheric.

By comparing top-down and bottom-up studies on methane emission estimation at scales from device to continental scale, Brand et al. (2014) concluded that official inventories such as EPA-GHGI and EDGAR consistently underestimate methane emissions. Figure 3-1 shows the ratio of measured (estimated) methane emissions in different studies to predicted values or emission factors by inventories, separated based on the scale of measurements. Smaller scale studies based on bottom-up evaluation have higher variation in methane emission estimation due to large variation in emission rate of equipment and super emitters. Larger scale studies based on top-down methods show better agreements when compared to smaller scale evaluation and consistently estimate higher than inventory emissions.

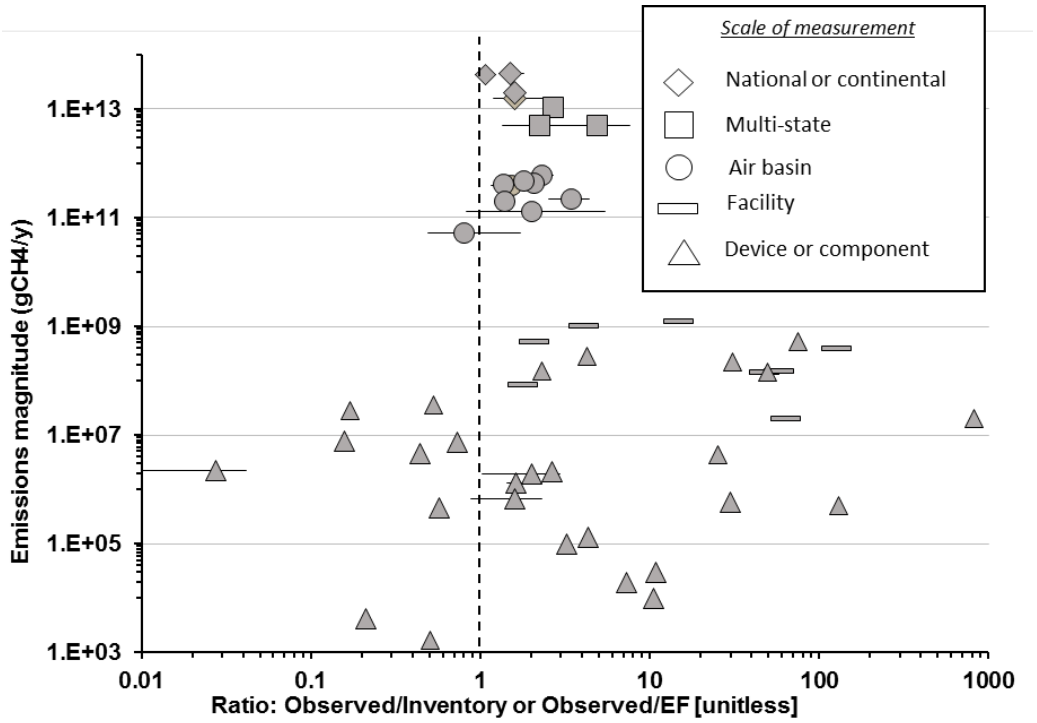

Figure 3-1 Comparison between methane emission estimation/observation and inventories. Adapted from Brandt et al (2014) (Brandt et al., 2014)

At the global scale, methane concentrations began rising in 2007, with the rate of ~6 ppb/year, after a slowdown in growth in the late 1990s (Hausmann et al., 2016; Nisbet et al., 2014). The reason for this sudden increase is poorly understood due to high uncertainty in the global methane budget. Methane has both natural (e. g. wetlands) and anthropogenic (e. g. oil and NG facilities, agriculture, landfills) sources and oxidation by hydroxyl radicals (OH) is the major sink (~90%) for atmospheric methane (Kirschke et al., 2013). Reducing the uncertainties associated with global methane is a difficult task because of various sources of methane, lack of observation especially from natural sources, and complexity in capturing OH trends. Studies suggest two dominant contributors for the increasing trend of methane; (i) tropical and boreal wetlands, and (ii) oil, NG, and coal extraction. Carbon isotope observations (^{13}C and ^{12}C isotope) suggest wetlands and agricultural sources (ruminants and rice paddies) as the dominant factor driving this increase (Nisbet et al., 2016; Schaefer et al., 2016). While remote sensing and

satellite observations paired with modeling tools point to the North American oil and NG facilities as one of the most important contributors to the global methane trend (Bergamaschi et al., 2013; Turner et al., 2016). Satellite measurements can cover areas with poor ground measurements coverage, yet methane source attribution remains a challenge in areas with multiple methane emission sources (Saunois et al., 2016). Studying co-emitted species such as ethane (methane to ethane ratio) can provide a valuable constrain on the source attribution of methane emission. Variability in the relation between co-emitters is one of the limitations of this approach. For example, methane to ethane ratio ranges between 1.7 to 33 (Helmig et al., 2016) depending on the facility which limits our confidence in estimation methane emission. Additionally, Helmig et al. (2016) points that using methane co-emitters to estimate methane emission from oil and NG facilities tend to overestimate methane concentration. This could be due to lower methane to ethane ratio or potential emission increase outside North America that are not well measured.

Using simulations of global energy-economy-climate systems, McJeon et al. (2014) showed that with the current greenhouse gas mitigation policies we cannot benefit from replacing coal with NG. On the positive side, methane mitigation policies can potentially have near-term climate benefits because of the shorter life-time and stronger radiative forcing of methane in comparison with CO_2 (Shindell et al., 2012). Additionally, health impact assessment of NG facilities for regulation development can be limited by the lack of an accurate estimate of air pollution emissions. The high uncertainties and inconsistency in the literature on the methane budget, emissions from NG facilities, and the role of oil and NG emission in the global anthropogenic emissions are the main challenges in the development of climate mitigation policies and air pollution control regulation.

Chemical transport models (CTMs) can be coupled with inverse modeling techniques to estimate emissions while capturing the atmospheric transport and chemistry. The Adjoint of GEOS-Chem (Goddard Earth Observing System Chemistry) model (Henze et al., 2006) has been used along with different types of observation to perform inverse modeling with chemistry on oil and NG emission at continental, and global scales (Turner et al., 2015, 2016; Wecht et al., 2014). GEOS-Chem adjoint is a suitable method to constrain emissions at continental and global scale because of coarse grid sizes. Improving high resolution emission inventories using inverse modeling method is a more sophisticated and computationally expensive task. However, it leads to more accurate impact assessment and can reduce the uncertainties in emission inventories.

High resolution regional CTMs can be used to improve emission inventories. Studies that performed inverse modeling techniques at regional high resolution scale to constraint oil and NG emission are very limited. Cui et. al (2015) used FLEXPART coupled with WRF (Weather Research and Forecasting) as forward metrological model and aircraft measurement to quantify methane emission at 8km x 8km horizontal resolution in southern California. Using this method, they attributed the observed methane to oil and NG systems, dairies, and landfills. As discussed, using FLEXPART-WRF instead of a CTM limits the inverse modeling to less reactive species like methane. Emission from oil and NG include more reactive species such as non-methane hydrocarbons (e. q. VOCs), NOx, and CO which have a significant impact on regional air quality. Therefore, it is essential to expand the inverse modeling technique to capture other air pollutants by incorporating CTM in this technique

In this study, we used WRF-Chem model to capture the meteorology and atmospheric chemistry in high horizontal resolution (4km x 4km) in the Northern Front Range (NFR) Colorado. Variational inverse modeling technique described in Saide et al. (2015) was implemented using

measurements from Deriving Information on Surface Conditions from COlumn and VERtically Resolved Observations Relevant to Air Quality (DISCOVER-AQ) and Front Range Air Pollution and Photochemistry Éxperiment (FRAPPÉ) field campaigns to constrain ethane emission from oil and NG sector. This method has the ability to improve the emission estimates by constraining hourly emissions using high-resolution full-chemistry simulations and measurements. We used ethane as the oil and NG tracers because it is dominantly emitted from oil and NG sector in the domain (Yacovitch et al., 2014) and has a relatively long lifetime of about two months (Helmig et al., 2016). Methane has multiple sources such as oil and NG and feedlots which can introduce uncertainties to the solution because of the uncertainties in the source apportionment of measured methane.

3.2 Method

3.2.1 Model description and inversion methodology

WRF-Chem 3.6.1. (Grell et al., 2005; Skamarock et al., 2008) was used to model the transport and meteorology in the Northern Front Range (NFR) in Colorado. Chapter 2 describes the details of the WRF-Chem configuration and set-up used for the NFR domain. We changed the chemical and aerosol mechanisms to MOZART (Emmons et al., 2010) and GOCART (Ginoux et al., 2001) respectively. NEI2011-v2 was used as the anthropogenic emission inventory and a priori for the oil and NG emissions. Airborne ethane measurements by C130 and P3 aircrafts during FRAPPÉ and DISCOVER-AQ, as described in Chapter 2, were used in the inversion method.

Variational inversion method (Saide et al., 2015) is implemented to constrain ethane hourly emission rates from oil and NG sector using airborne measurements from C130 and P3 aircraft. We added passive hourly tracers linked to hourly ethane emissions from oil and NG sources in the simulation. The passive tracers do not deposit or react in the simulation, they are simply

being transported in the domain. We designed and tested different inversion experiments by adding different groups of tracers linked to emissions from certain regions and days. The hourly tracers specific to certain regions can provide more information regarding the temporal and spatial distribution of oil and NG emissions. Two simulations, one based on NEI-2011v2 and the other one based on NEI-2011v2 with perturbed (doubled) oil and NG emissions and both with added passive tracers, were used in the inversion method to calculate the sensitivity of the ethane concentration fields to changes in emission. The sensitivity matrices calculated with Equation 3-1 to Equation 3-5 and then used in the cost function (Equation 3-6) to determine the optimal scaling factor for each tracer. Given num_{obs} number of ethane concertation measurement points, we extracted the corresponding ethane and tracer model concentrations (in time and location) for both base simulation (Equation 3-1) and perturbed simulation (Equation 3-2).

$$B_{eth} = \begin{pmatrix} Beth_1 \\ \vdots \\ Beth_i \\ \vdots \\ Beth_{num\_obs} \end{pmatrix} \quad \text{Equation 3-1}$$

$$P_{eth} = \begin{pmatrix} Peth_1 \\ \vdots \\ Peth_i \\ \vdots \\ Peth_{num\_obs} \end{pmatrix} \quad \text{Equation 3-2}$$

Where $0 \leq i \leq num_{obs}$ and $Beth_i$ is the ethane concentration at observation point *i* (time and location) in the base model and $Peth_i$ the ethane concentration at observation point *i* (time and location) in the perturbed model.

$$B_{tr} = \begin{pmatrix} Btr_{(1,1)} & \cdots & Btr_{(1,num\_tr)} \\ \vdots & Btr_{(i,j)} & \vdots \\ Btr_{(num_{obs},1)} & \cdots & Btr_{(num_{obs},num_{tr})} \end{pmatrix} \quad \text{Equation 3-3}$$

Where $0 \leq j \leq num_{tr}$ and num_{tr} is the total number of tracers. Btr includes the concentration of all tracers (from 1 to num_{tr}) at each measurement point in the base model. Ptr matrix is built similarly but with tracer concentration in the perturbed model.

$$B_{TOTtr} = \begin{pmatrix} Btr_{(1,1)} + \cdots + Btr_{(1,j)} + \cdots + Btr_{(1,num_{tr})} \\ Btr_{(i,1)} + \cdots + Btr_{(i,j)} + \cdots + Btr_{(i,num_{tr})} \\ Btr_{(num_{obs},1)} + \cdots + Btr_{(num_{obs},j)} + \cdots + Btr_{(num_{obs},num_{tr})} \end{pmatrix} \quad \text{Equation 3-4}$$

B_{TOTtr} is an array and includes the sum of all tracer concentrations at each measurement point in the base model. P_{TOTtr} is calculated similarly but with tracer concentrations in the perturbed model.

$$H_n(i,j) = \left(\frac{[P_{eth} - B_{eth}]}{[P_{TOTtr} - B_{TOTtr}]}\right) \times \left(\frac{P_{tr} - B_{tr}}{F_P - F_B}\right) \quad \text{Equation 3-5}$$

Where Fp is the scaling factor of the perturbation simulation which is 2 in this experiment and Fb is the scaling factor of the base simulation which is 1 in this experiment. H_n is the Jacobian matrix for measurement set n (e.g. airborne measurements by C130)

$$J(F) = J_1 + E \times J_2 \quad \text{Equation 3-6}$$

$$J_1 = \frac{W_n}{2}\left(ln\left[\frac{H_n*(F-F_b)+B_{eth}-B_{other}}{OBS_{eth}-B_{other}}\right]\right)^t R_n^{-1}\left(ln\left[\frac{H_n*(F-F_b)+B_{eth}-B_{other}}{OBS_{eth}-B_{other}}\right]\right) \quad \text{Equation 3-7}$$

$$J_2 = \frac{1}{2}\left(ln\left[\frac{F}{F_b}\right]\right)^t B^{-1}\left(ln\left[\frac{F}{F_b}\right]\right) \quad \text{Equation 3-8}$$

Cost function (J), as presented in Equation 3-6, consists of two terms representing errors by deviation from measurement (J_1) and errors by deviation from initial guess or emission inventory (J_2). E is a regularization parameter and is used to balance between the two terms of the cost

function. E is set based on uncertainties in the measurements compared to the initial guess (Henze et al., 2008). Higher values of E will result in higher impact of initial guess on the final solution thus less deviation from initial guess and lower values of E will cause solutions closer to measured values. Optimal E value was determined using L-curve method (Hansen, 2005) and visualization of errors in J_1 and J_2 with respect to different E values (Henze et al., 2008). Minimizing the cost function (J(F)) will provide optimal scaling factor (F) that minimizes the errors with respect to observation uncertainties (R) and uncertainties in initial guess or emission inventory (B). We used liner cost function instead of logarithmic cost function as used in Saide et al. (2015). A logarithmic cost function puts equal weight on the model-measured discrepancies for the enhanced and low (background) concentration values when calculating the scaling factor. However, in a linear cost function model-measured discrepancies at the enhancements have a larger impact on the solution. Oil and NG sector is the dominant source of ethane in the region and the focus of this work is to improve the model performance in capturing the enhancements (not the background), thus we used linear cost function. B_{other} includes ethane emitted from non-oil and NG sources (which is negligible).

W_n is set to assign a smaller weight to observation datasets with larger measurement points. This way all datasets can equally contribute to the cost function. W_n is simply the ratio of number of measurements in dataset n to total number of measurements in all datasets. We assumed no correlation between observation errors thus R_n is an identity matrix. B is calculated using exponential decay law (Saide et al., 2012, 2015) and correlates emissions which are closer in time to produce a smoother solution.

$$B_{ij} = e^{-\frac{\Delta t}{L_t}}$$ Equation 3-9

Where Δt is the time differences between traces and L_t is the correlation length scale and is set to 4 hours. L-BFGS-B numerical method is used to minimize the cost function (Zhu et al., 1997).

3.3 Results and Discussion

3.3.1 Denver Julesburg basin oil and NG emissions

In the first experiment, we evaluated the contribution of oil and NG emissions from Denver Julesburg (DJ) basin to the total ethane concentration at the measurement points. Two sets of hourly tracers were assigned to the ethane emitted from oil and NG source inside (set 1) and outside (set 2) DJ basin and one tracer was assigned to ethane emitted from all non-oil and NG sources in the domains (Figure 3-2).

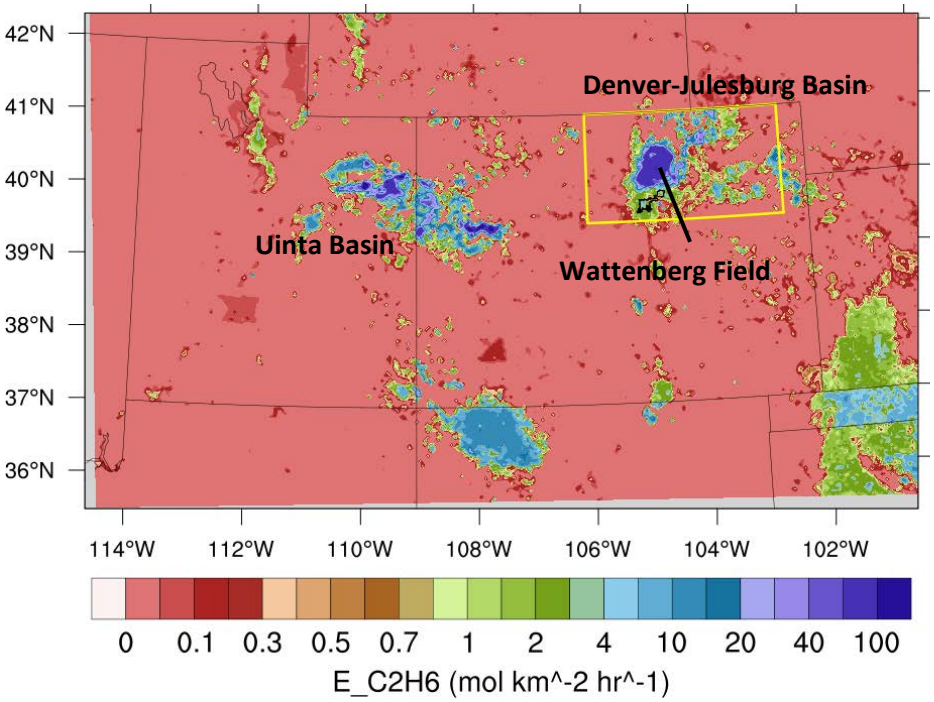

Figure 3-2 spatial distribution of ethane emission from oil and NG in the inner domain in the NEI-2011v2. Set 1 of tracers (DJ basin) were released from oil and NG sources in the yellow rectangle

Initial and boundary values of all tracers were set to zero. In this 3-day experiment, 72 hourly tracers for set 1 (DJ basin) and set 2 and one single tracers for non-oil and NG sources, total of

145 tracers, were added to the WRF-Chem model. Simulations started on 1 August 2014 00Z and to 4 August 2014 00Z. C130 performed two flights and P3 performed four flights on 2 and 3 August 2014. Figure 3-3 shows the flight patterns of C130 and P3 morning flights with circles indicating the model errors at each observation point. P3 afternoon flight follows the same pattern as the morning flight (not shown). Overall, negative biases were observed over regions with high modeled surface ethane concentrations or oil and NG activity regions.

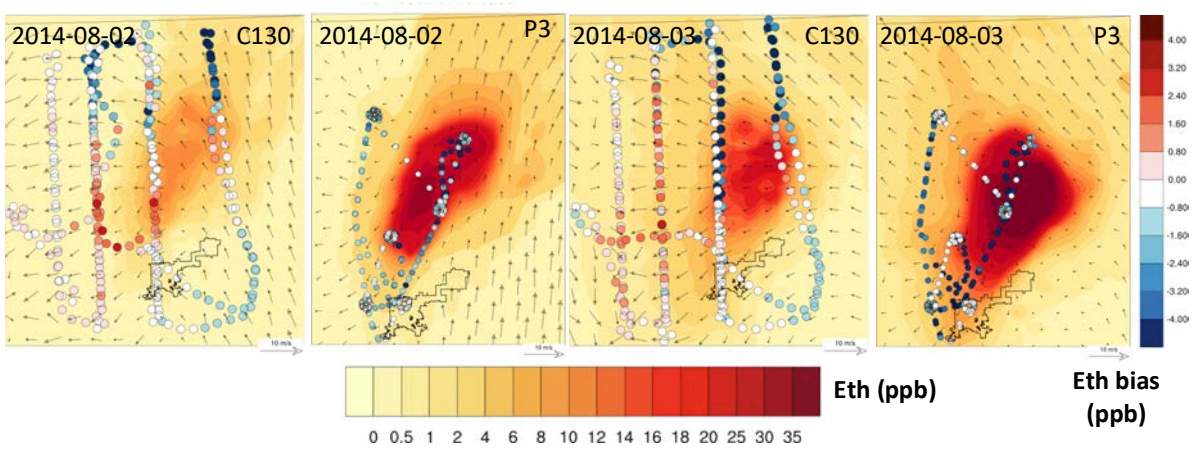

Figure 3-3 circles show errors in ethane concentration along C130 and P3 flight trajectory on 2 and 3 August 2014. Background contour shows the surface ethane concentration at 18Z (12am LT) for C130 and at 16Z (10am LT) for P3 on the flight day. Denver county is marked on the maps with a black line

C130 flights on 2 and 3 August 2014 both took place in the afternoon (from 2pm to 6pm LT). Figure 3-4 illustrates higher concentrations of ethane measured by C130 aircraft on 3 August 2014 compared to 2 August 2014. Model underestimated wind speed but captured wind direction on 2 August at the measurement points with enhanced ethane concentrations. Model wind speed performance was slightly better on 3 August 2014.

In theory because of the relative long lifetime of ethane (about 2 months), the sum of all tracers concentration is very close to the ethane concentration. We determined the contribution of each set of tracers and tracers released on different days to the total tracer concentrations at the

measurement points. Figure 3-4a and b show measured and modeled ethane concentrations and the sum of all tracer set 1 concentrations in base (red) and perturbed (blue) simulations. It can be concluded that DJ basin (set 1) emissions are the major contributors to the total ethane concentrations along the C130 flight. Sum of all tracers separated by the release day along the C130 flights are plotted in Figure 3-4c and d. Emissions released on the day of the measurement are the main contributors to the total ethane concentrations. Modeled ethane concentration had a strong sensitivity to the increase in oil and NG emissions especially in places with enhanced ethane concentrations (peaks).

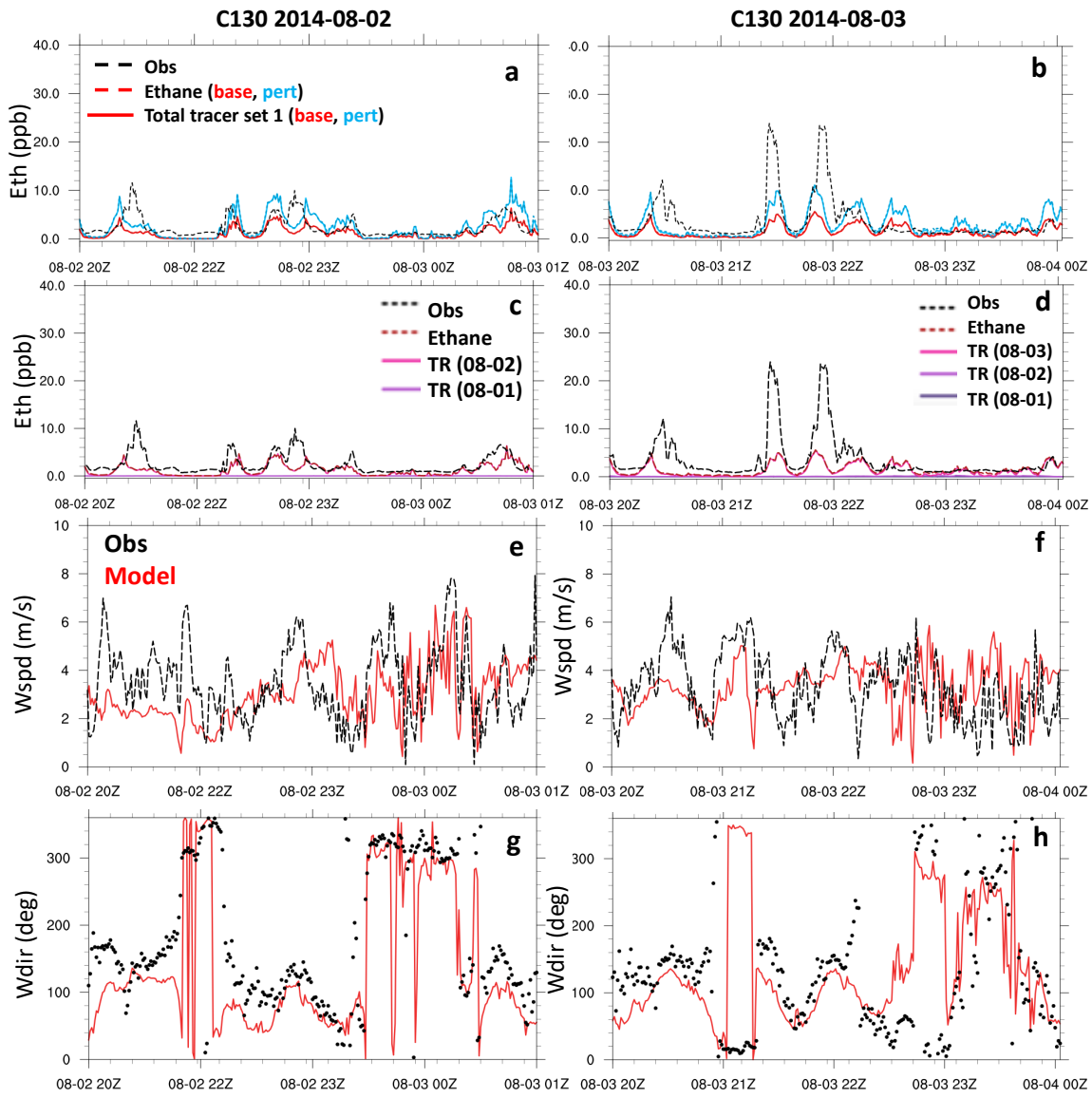

Figure 3-4 Left column: measured and modeled values along 2 August 2014 flight. Right column: measured and modeled values along 3 August 2014 flight. Subplots a and b show measured ethane concentration in black dashed line. Red and blue lines show ethane and tracer concentrations in base and perturbed simulations, respectively. solid lines show sum of all tracers set 1 (DJ basin) at the measurement point. Subplots c and d show sum of all tracers separated by the release days. Sub-plots e and f show measured (black) and modeled (red) wind speeds. Sub-plots g and h show measured (black) and modeled (red) wind direction

The morning (AM) P3 flights on 2 and 3 August started at 7am to 12pm and afternoon (PM) started at 1pm to 6pm. Wind filed measurements were not available during P3 flights because of the limits of equipment in measuring wind fields during flights with spiral patterns. Overall, higher ethane concentrations were measured and modeled during AM flights because of the

lower morning PBL height (Figure 3-5) (Abdi-Oskouei et al., 2018). Similar to C130, P3 measured lower ethane concentrations in the afternoon of 2 August compared to 3 August. During P3 flights, Model showed strong sensitivity to increase in oil and NG emissions in locations where enhanced ethane concentration were measured (spirals over oil and NG facilities). Sum of tracers in set 1 along the P3 trajectory indicates that emissions from the DJ basin are the main contributors to measured ethane which confirms the results from C130 flights. Similarly, emissions released on days prior to day of the measurement did not play a significant role in the total ethane (not shown).

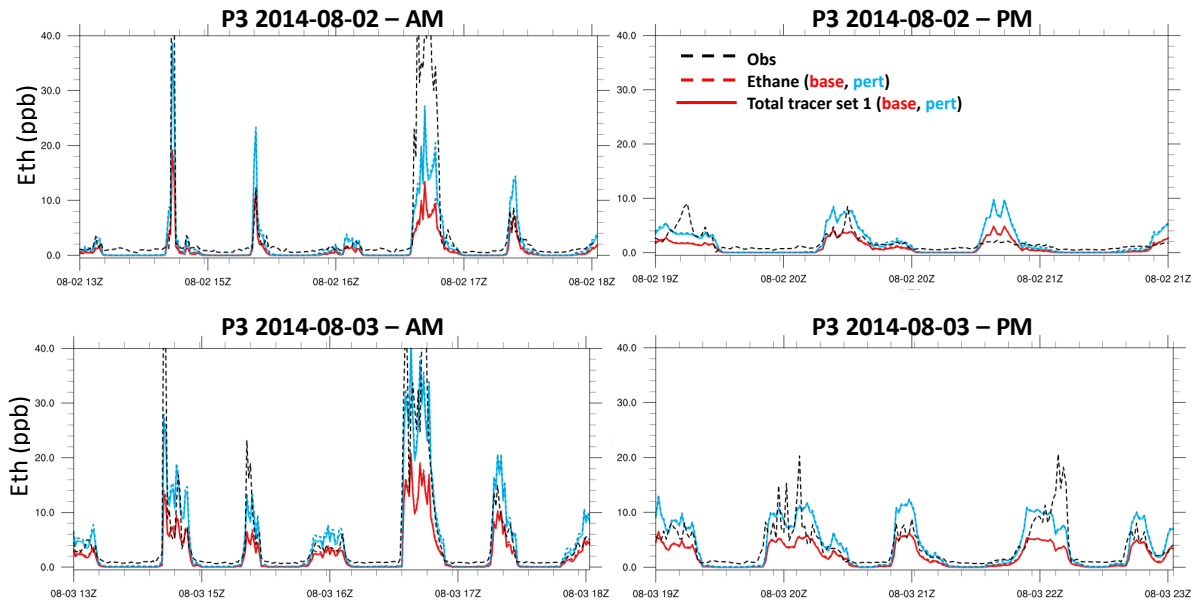

Figure 3-5 Measured ethane concentration in black dashed line. Red and blue lines show ethane and tracer concentrations in base and perturbed simulations, respectively. solid lines show sum of all tracers set 1 (DJ basin) at the measurement point

3.3.2 Ethane emission estimates using DJ basin tracers

We performed variational inversion method to calculate optimal scaling factor for each tracer emission rate. In this experiment we assumed that there is no day-to-day variation in oil and NG emissions and only used 24 tracers for each tracer set. The contribution of tracers released on

days prior to the flight days is small. Thus, not including these tracers will not impact the inverse modeling solutions.

Both L-curve and visualization methods were used to assess the impact of using different E values on the inverse modeling solution (Figure 3-6 a and b). In the L-curve plot, optimal E maximizes the curvature between J_1 and J_2. L-curve plotted using E values from 0.01 to 100 (Figure 3-6 a) is almost a straight line and thus inconclusive. In Figure 3-6 b, J_1 error is normalized to J_1 values (x axis) and J_2 error is normalized to J_2 values at the smallest E (0.01) (y-axis). Sum of normalized errors (J_1 and J_2 terms) in, is minimized at E of 5. Correction factors of 24 tracers in set 1 and set 2 calculated for E of 0.1, 1, and 5 are plotted in Figure 3-6c and d. Smaller E value resulted in higher variation in hourly correction factor of tracers in set 1. We used E =5 which resulted in a smooth solution for tracers in set 1. Overall, the contribution of emission released from outside the DJ basin to total ethane concentration was small. With E =5, inverse modeling method calculated small correction factors for tracers in set 2 which agrees with the negligible contribution of these tracers to the total ethane concentration.

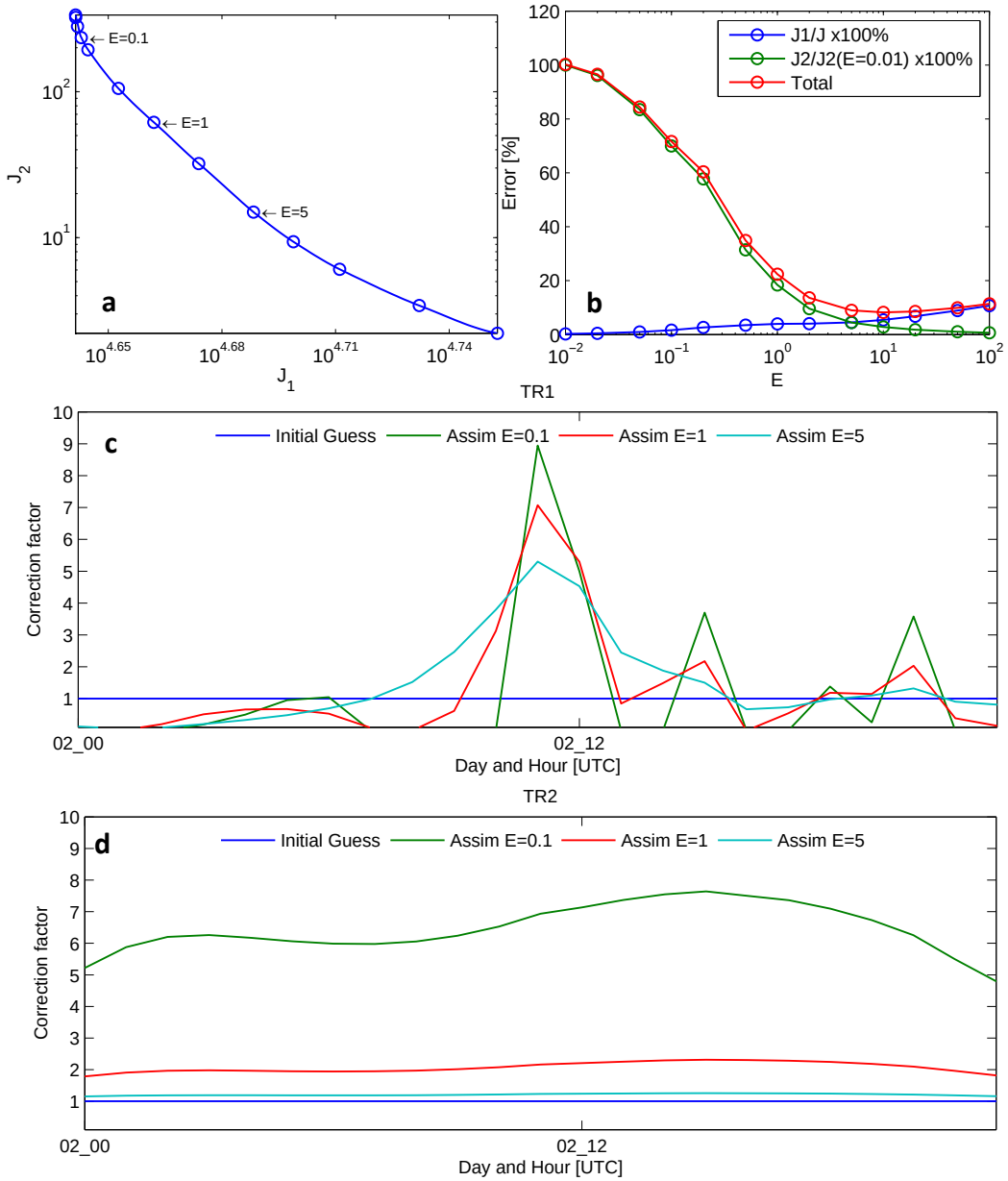

Figure 3-6 Effect of regularization parameter (E) value on the correction factor calculated by the inverse modeling method. a: L-Curve, b: Total error minimization, c: correction factor for tracer set 1 (DJ basin), d: correction factor for tracer set 2 (outside DJ basin)

Figure 3-7 shows the correction factor calculated for each hourly tracer in set 1 and set 2 with E = 5. The correction factors were applied to the ethane emissions from oil and NG sector based on the location (e.g., ethane emission in DJ basin was scaled using correction factor of set 1).

Correction factors for DJ basin ethane (from oil and NG) emissions at hours 0Z to 7Z (6pm to

1am LT) are less than one which indicates emission rates smaller than initial guess during these hours. It should be noted that airborne measurements were not available during the nighttime and all measurements used in the inverse modeling method were conducted from 13Z to 23Z (7am to 5pm LT). From 7Z to 15Z (1am to 9am LT) large correction factors up to factor of 5 were calculated for DJ basin oil and NG emissions.

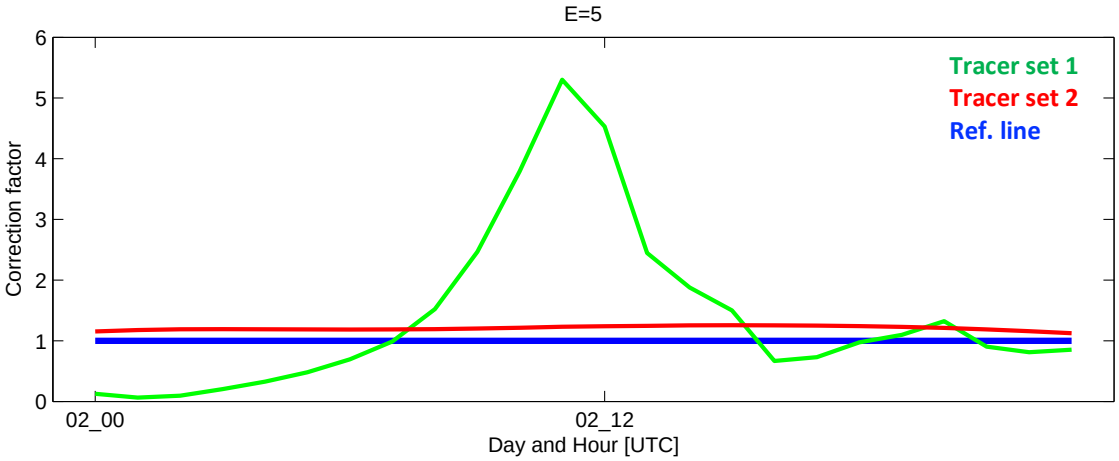

Figure 3-7 Hourly correction factor calculated for ethane emission in DJ basin (set 1/green) and outside DJ basin (set 2/red)

Using correction factors calculated in the IM_2sets experiment the total daily ethane emission in the DJ Basin increased from $4.4x10^{14}$ kg/day to $4.9x10^{14}$ kg/day (11% increase) and in domain 2 from $2.6x10^{16}$ kg/day to $3x10^{16}$ kg/day (15% increase) (Table 3-1).

Table 3-1 Daily ethane emission (kg/day) from domain 2 and DJ basin in NEI_2011v2 (initial guess) and scaled emission inventories

Emission inventory	Eth emiss (kg/day) Domain 2	Eth emiss (kg/day) DJ basin
Initial guess (NEI-2011v2)	2.6E+16	4.4E+14
IM_2sets	3.0E+16	4.9E+14
IM_4sets	3.9E+16	5.8E+14

A WRF-Chem simulation was conducted from 1 to 9 August 2014 with the IM_2sets scaled emission inventory to assess the performance of the updated emission inventory. Figure 3-8

illustrates ethane concentrations measured along C130 and P3 aircraft and model values on 2 and 3 August (used in the inverse modeling calculation or Data Assimilation (DA) days). Model with IM_2sets scaled emissions (blue line) better capturing enhanced ethane concentrations compared to the initial simulation.

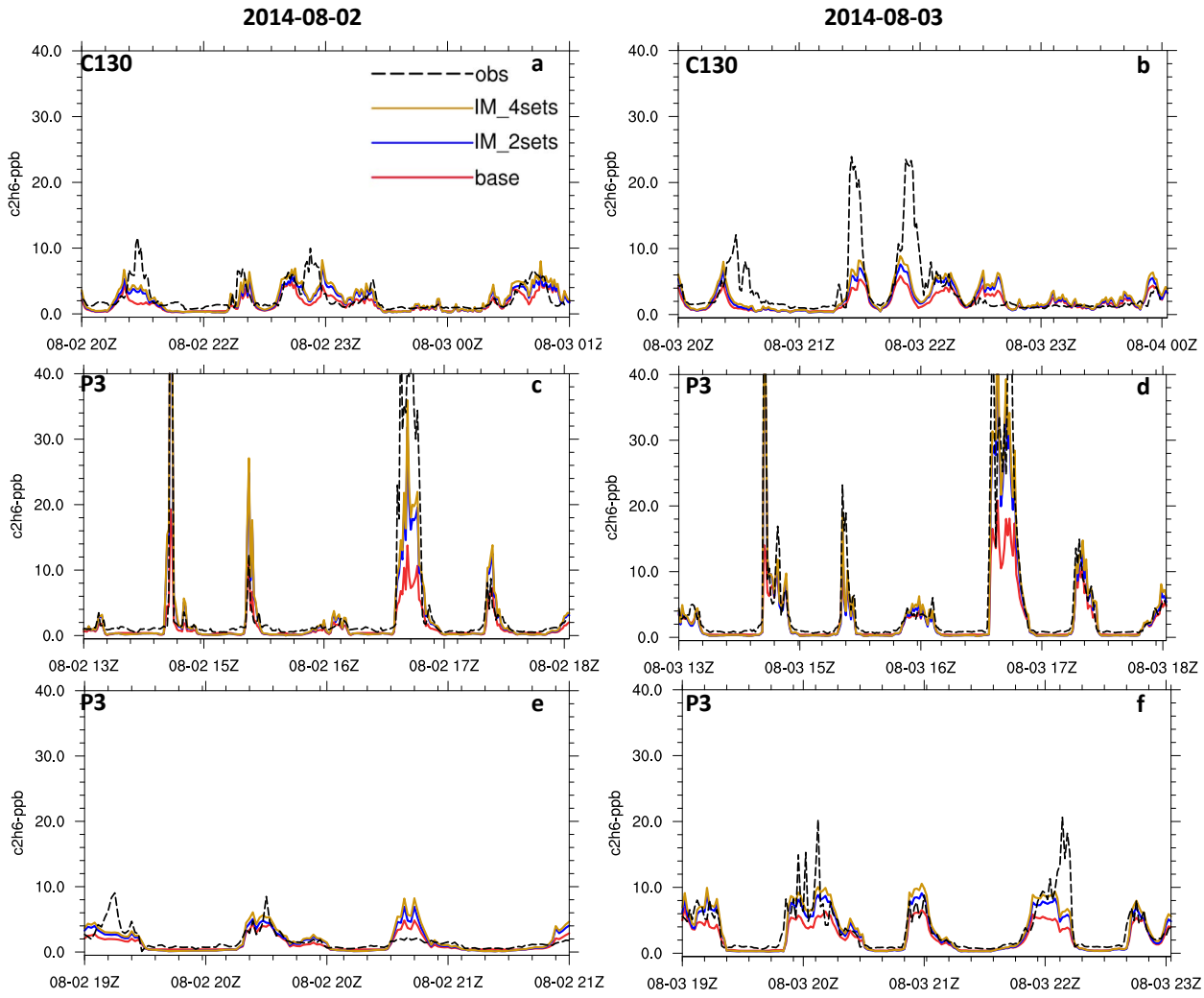

Figure 3-8 Measured and modeled ethane concentration along C130 and P3 aircraft. Left column: 2 August 2014 flights. Right column: 3 August 2014 flights. Black, red, blue, and gold lines show measurement, simulation with initial emission, simulation with updated emission (2 sets), and simulation with updated emission (4 sets), respectively. Red numbers are indicators for the FLEXPART back-trajectory tests

Table 3-2 includes statistics of the model performance compared with all P3 and C130 measurements during 2 to 8 August 2014 and separated based on flights included in the inverse

modeling calculation (DA days) and flights not included in the inverse modeling calculation (non-DA days). The statistics are calculated for measurement points with ethane concentration greater than 2ppb to only focus on model performance in capturing ethane concentration enhancements. Overall, scaled emission inventory improved the model performance in the IM_2sets simulation with Normalized Mean Bias (NMB) of -0.47ppb in the initial simulation and -0.21ppb in the simulation with scaled emission inventory. Index of Agreement (IOA) was improved from 0.56 to 0.73.

Table 3-2 Summary of statistics of ethane concentration (ppb) measured on C130 and P3 aircraft (only for ethane concentration > 2ppb) compared with modeled ethane concentration in simulation with initial guess and scaled emission inventory. Non-DA days include flights on 6, 7, 8 August 2014 and DA days include 2 and 3 August 2014

obs > 2ppb	model	R	MAE	RMSE	MB	NMB	IOA
All	base	0.55	4.64	8.68	-3.82	-0.47	0.56
	IM_2sets	0.56	4.40	8.18	-1.71	-0.21	0.73
	IM_4sets	0.56	4.52	8.26	-0.87	-0.11	0.74
Non-DA days	base	0.52	5.27	8.92	-4.62	-0.55	0.51
	IM_2sets	0.52	4.70	8.16	-3.08	-0.37	0.63
	IM_4sets	0.51	4.60	8.01	-2.35	-0.28	0.66
DA days	base	0.59	4.01	8.43	-3.01	-0.38	0.61
	IM_2sets	0.63	4.09	8.2	-0.32	-0.04	0.78
	IM_4sets	0.63	4.43	8.51	0.63	0.08	0.78

Figure 3-9 shows the vertical distribution of ethane concentration measured during C130 and P3 and the corresponding model values. The IM_2sets simulation (blue color) predicted higher ethane concentration at all altitudes compared to initial simulation (red color). Simulation with the scaled emission inventory better captured the variance in ethane concentration at lower altitudes and slightly overestimated ethane concentration at higher altitudes during both DA and non-DA flights.

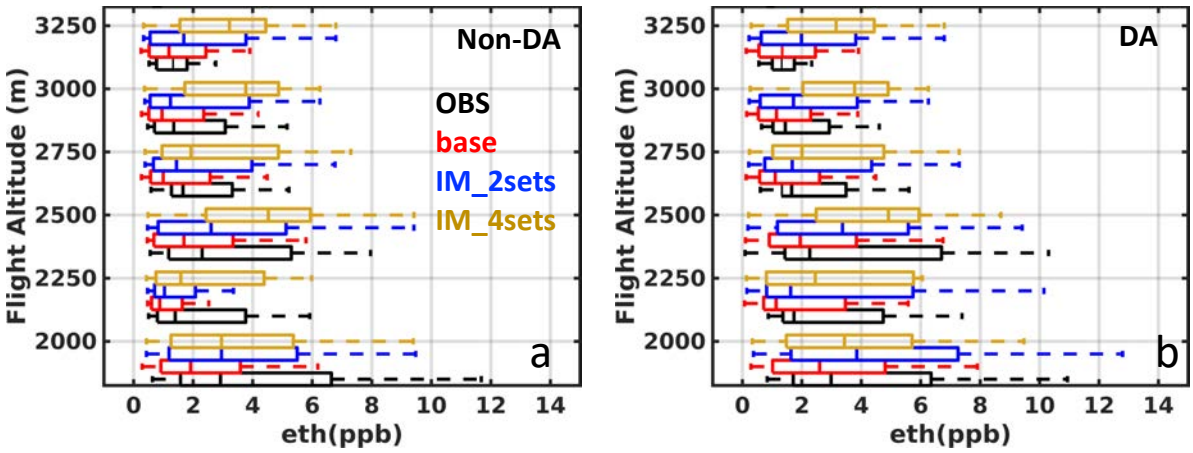

Figure 3-9 Vertical distribution of measured and modeled ethane concentration along C130 and P3 aircrafts on non-DA flights (not included in the inversion calculation) and DA flights. Elevations are meters above sea level

3.3.3 Ethane emission estimates using sub-region tracers

Given the improved model performance in predicting ethane concentration enhancements in IM_2sets simulation, we performed a similar experiment with more sets of tracers in the DJ basin (i.e., IM_4sets). Addition of more tracer sets emitted from sub-regions within the DJ basin can provide more spatial information regarding the emission rates in the region. Three sets of oil and NG hourly tracers focusing on DJ basin sub-regions emission and one set of tracers focusing on emissions outside of the three sub-regions were linked to oil and NG emissions in the IM_4sets experiment. One single tracer was linked to the ethane emission from non-oil and NG sources. Figure 3-10 illustrates the location of sub-regions in DJ basin. Sub-region 1 covers Wattenberg field north of Denver with heavy oil and NG activities and the highest ethane emission rates. sub-regions 2 and 3 include northeast and east of Denver with lower ethane emission rates.

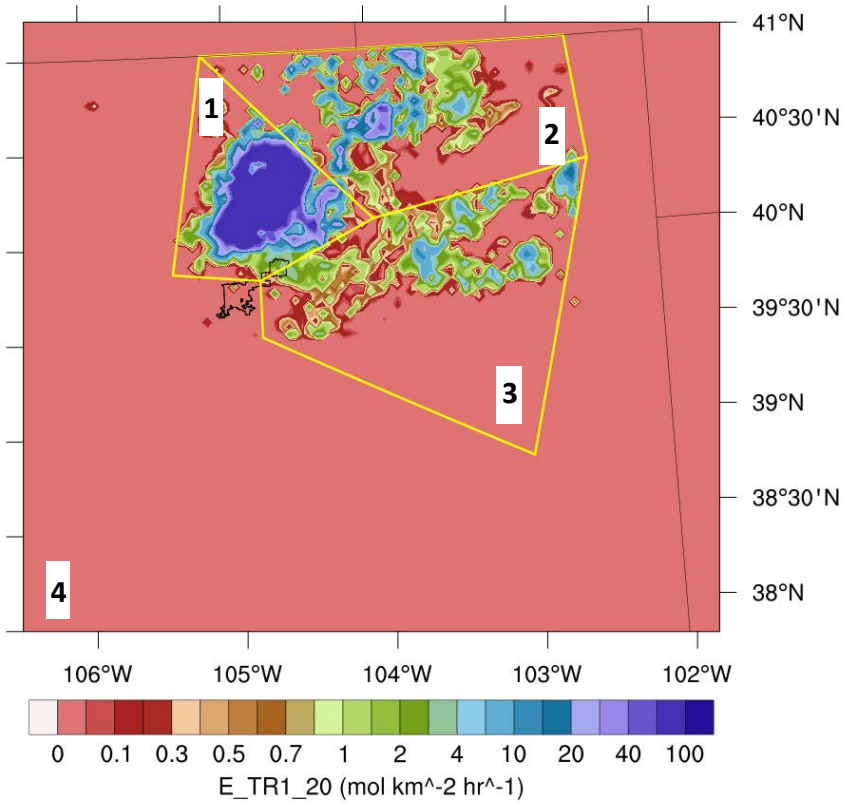

Figure 3-10 Spatial distribution of ethane from oil and NG sector and the location of sub-regions

Variational inversion method was conducted to calculate the optimal scaling factor for each hourly tracer in the four sub-regions. Similar to the IM_2sets experiment (section 3.3.2), E=5 minimized the total of J1 and J2 errors (Figure 3-11).

The Highest correction factor (up to 6) was assigned to sub-region 1 (Wattenberg field) with highest emission rates of ethane. Diurnal variability of correction factor of sub-region 1 is very similar to correction factor of DJ basin in IM_2sets experiment with values less than 1 from 00Z to 7Z (6pm to 1am LT) and large values from 7Z to 15Z (1am to 9am). Correction factors calculated for sub-region 2 and 3 are both higher than 1 for all hours with larger values (up to 3) assigned to sub-region 2. Similarly, correction factors for set 4 (outside the three sub-regions) are higher than 1 but almost constant throughout the day. Tracer set 4 are released from area further from the measurement location and are well mixed, thus do not have a diurnal variation in their

scaling factor. Using IM_4sets scaling factors, the total ethane emission in the DJ basin in the scaled emission inventory is 5.8×10^{14} kg/day (16% higher than initial guess) and 3.9×10^{16} kg/day (50% higher than initial guess) in domain 2 (Table 3-1). Domain 2 covers Utah and Uintah basin with high oil and NG extraction activities. The large ethane emission rates outside DJ basin in the domain 2 and the scaling factor of ~1.5 for tracer 4 justify the 50% increase in the ethane emissions with IM_4set scaling factor in the domain 2.

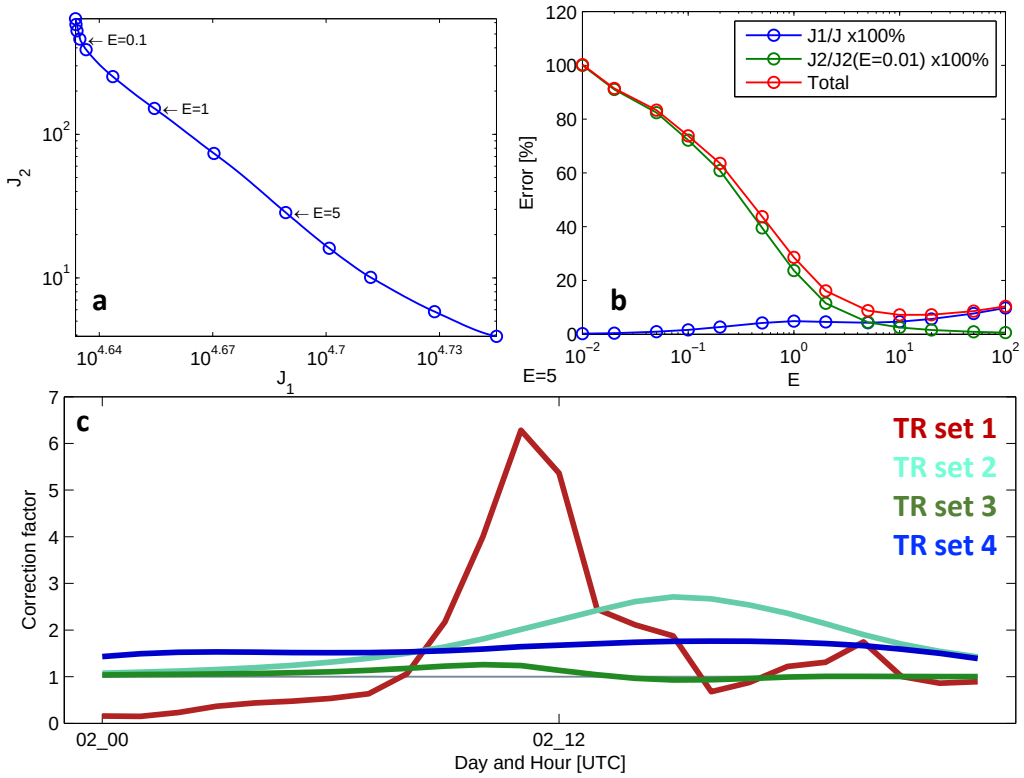

Figure 3-11 Effect of regularization parameter (E) value on the correction factor calculated by the inverse modeling method in IM_4sets experiment. a: L-Curve, b: Total error minimization. c: correction factor for each set of hourly tracers

In Figure 3-8, the gold line indicates the modeled ethane concentration in the WRF-chem simulation based on emission inventory scaled using IM_4sets correction factors. At the measurement points ethane concentration in IM_4sets simulation is very similar to IM_2sets simulation with slightly higher values at the enhancement points. Statistics in Table 3-2 shows

slightly better performance for IM_4sets simulation comparted to IM_2sets. Comparison of vertical distribution in Figure 3-9 shows high concentrations of ethane in IM_4sets simulation compared to measurement and IM_2sets. This could be due to higher scaling factor calculated for region 4 which impacted the lateral boundary value of ethane concentration.

Figure 3-12 shows total hourly ethane emission rates (from oil and NG sector) in the DJ basin and in domain 2. Overall, emission rates in domain 2 which also includes DJ basin and Uintah basin in Utah follow the diurnal variation of initial emission inventory (base) with lower emission rates from 4Z to 12Z (10pm to 6am LT). DJ basin scaled ethane emission (both IM_2sets and IM_4sets) however, does not follow the same diurnal cycle. Large scaling factor for DJ basin tracers and small scaling factors for emissions outside DJ basin can explain the differences between diurnal cycle of ethane emission rates in the DJ basin and domain 2.

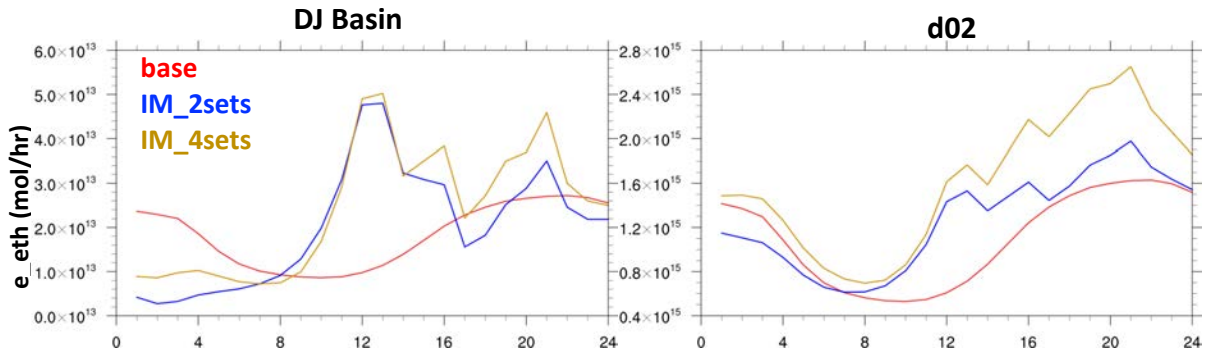

Figure 3-12 Total ethane emission rate from oil ad NG sector in the DJ basin (left) and in domain 2 (right) for the base, IM_2sets, and IM_4sets emission inventories

3.4 Conclusions

There is a large uncertainty in the emission estimates from the oil and NG sector. Several field campaigns have been carried out to better understand the oil and NG emissions (Peischl et al., 2018). In this work we used a variational inversion method with high-resolution WRF-Chem simulation and measurements from FRAPPÉ and DISCOVER-AQ field campaigns to constrain

the ethane emissions from oil and NG sector. Hourly tracers were assigned to oil and NG ethane emissions. Forward WRF-Chem simulations with tracers indicates that majority of ethane measured along C130 and P3 aircraft were emitted from the DJ basin on the day of the measurement. The inverse modeling method calculated optimal scaling factor for each tracer. We tested different set-ups for tracers and used 6 sets of aircraft measurements on 2 and 3 August 2014. Scaling factors up to 6 were calculated for ethane emitted from the Wattenberg field. The inverse modeling solution indicates that the total ethane emissions from oil and NG sector is between 11% to 15% higher than the NEI-2011v2 emission inventory in the DJ basin.

One of the limitations of this method is that the errors in transport can be interpreted as errors in emissions inventory and impact the scaling factor. It is important to study the model performance in capturing transport prior to carrying out the variation inversion method. Performing inversion on a WRF-Chem simulation with a different model configuration can provide variability in scaling factor due to changes in model transport. Based on resulted discussed in Chapter 2, PBL scheme can have an important impact (up to 33% in normalized mean bias variability) on the model performance in capturing ethane. We will perform WRF-Chem simulation (base and perturbed mode) using YSU PBL scheme. Carrying out inversion method using WRF-Chem simulation with YSU PBL scheme will provide the variability of scaling factors and the range of estimates for ethane emission rates.

By using ethane to methane or other VOCs ratio in the measurement the constrained ethane emission rates can be scaled to estimate the emission rate of these species. For example, HC3 (lumped alkanes such as propane, n-butane, isobutane, and acetylene (ethyne)) concentration measured along the C130 aircraft showed a strong correlation with ethane concentration. Ethane to HC3 ratio of 0.6 (R^2=0.9) was observed for measurement points with ethane concentration

greater than 2ppb (oil and NG influenced). Using the ethane to HC3 ratio and constrained ethane emission rates, HC3 emission rates from oil and NG sector can be estimated and compared to the emission inventory values. Running a WRF-Chem simulation with the scaled emission inventory of ethane and HC3 and available HC3 observation will be used to assess the new emission rate performance.

4 CHEMICAL WEATHER FORECAST FOR FLIGHT PLANNING AND NEAR-REAL TIME ANALYSIS DURING THE LAKE MICHIGAN OZONE STUDY (LMOS) FILED CAMPAIGN

Abstract

The Lake Michigan Ozone Study (LMOS 2017) field experiment was conducted from 22 May to 22 June 2017, to address high ozone episodes in coastal communities surrounding Lake Michigan. Aircraft, ship, mobile lab, and ground-based sites were used to measure meteorological variables, ozone, ozone precursors, and particulate matter. The University of Iowa produced high-resolution (4x4 km horizontal resolution and 53 vertical levels) daily forecast products using the WRF-Chem modeling system in support of flight planning during LMOS 2017. We used WRF-Chem 3.6.1 and an updated version of the National Emission Inventory (NEI-2011v2). The forecast model successfully captured diurnal and synoptic meteorology fields and ozone concentrations. However, the forecast model under-predicted peak ozone at coastal locations during high ozone episodes and on average overestimated NOx.

In the post-campaign analysis, we tested the sensitivity of the meteorological skills, biogenic emission, and ozone formation to the selection of initial and boundary conditions and land surface model parametrization. Selection of High-Resolution Rapid Refresh (HRRR) model as initial and boundary condition, and the Noah land surface model, significantly improved comparison of meteorology variables to both ground-based and aircraft data. Biogenic isoprene emission and ozone concentration did not show a strong sensitivity to the increase in temperature within the domain of this study.

we investigated the sensitivity of ozone production in the model to hydrocarbon (biogenic and anthropogenic) and NOx emissions and to the WRF-Chem chemical mechanism. Reduction in

the NOx emissions had a marginal impact on the ozone production and concentrations in the model. Increases in hydrocarbon emissions increased ozone production especially over the Lake Michigan, which led to reduction in model errors.

4.1 Introduction

Ozone (O_3) is a secondary pollutant and is created by photochemical reaction of nitrogen oxides (NOx) with Volatile Organic Compounds (VOCs) (Seinfeld and Pandis, 2012). Ground-level ozone is associated with negative health (Anenberg et al., 2010) and environmental (Van Dingenen et al., 2009) impacts. The US National Ambient Air Quality Standard (NAAQS) for maximum 8-hr average ozone is 70ppb (United States Environmental Protection Agency (EPA), 2015). Both urban and rural regions around Lake Michigan have persistently recorded high ozone concentrations in exceedance of NAAQS standard. Currently, the Chicago nonattainment area and Sheboygan County (WI) are designated nonattainment for the 2008 ozone NAAQS (United States Environmental Protection Agency (EPA), 2018).

The unique meteorology caused by Lake Michigan and the biogenic, urban and industrial emission sources are some of the reasons for the high ozone concentrations in the region. The differences between air temperature over water and land drive land/lake breeze flows. In summer during the nighttime, higher air temperature over the lake than land creates land breeze (offshore flows). Opposite happens during the daytime and generates lake breeze (onshore flows). Lake breeze has been associated with high ozone concentrations along the shoreline of Lake Michigan (Harris and Kotamarthi, 2005; Lennartson and Schwartz, 1999; Lyons and Olsson, 1973). The Lake Michigan Air Quality Study 1991 (Dye et al., 1995) and the Lake Michigan Air Director of Consortium (LADCO) Air Craft Project (LAP 1994-2003) (Foley et al., 2011) are two important field experiments that used measurements systematically to better understand ozone formation

and transport over and around Lake Michigan. Typically morning land breeze (flow from land to the lake) transports pollutants (including ozone precursors) over the lake. Dye et al. (1995) showed that a shallow (up to 200m) stable layer (conduction layer) over the lake in summer with limited vertical and horizontal mixing traps emissions from off-shores sources in high concentrations. With high concentrations of ozone precursors, stable condition, and slower deposition rate over the lake, ozone is produced and accumulated over the lake in the conduction layer. Southerly and southwesterly winds transport ozone northward over the lake and afternoon lake breeze eventually transports ozone over the shore. During the LAP field experience high concentrations of reactive nitrogen (NOy) and VOC over the Lake were observed (Foley et al., 2011). Measurements by the Lake Express Ferry from 2008 to 2010 (from spring to fall) indicated on average ~4ppb higher ozone concentration over the lake compared to the shoreline in Kenosha, WI (Cleary et al., 2015). Foley et al. (2011) determined that 200m above the lake ozone production is VOC-limited (ozone production constrained by VOC concentration) in the mornings and becomes NOx-limited (ozone production constrained by NOx concentration) in the afternoon. Above 200m ozone formation is NOx-limited throughout the day.

Although the transport pattern over Lake Michigan and the surrounding region and its impact on high ozone events have been discussed, studies on assessing the performance of Chemical Transport Models (CTMs) in the region are limited. Models often fail to capture ozone behavior in the Lake Michigan region accurately (McNider et al., 2018). Discrepancies between predicted summertime ozone by different operational air quality models has been observed. For example, on 2 June 2017 high concentrations of ozone were measured by the stations along the west shore of Lake Michigan in the late afternoon. Figure 4-1 shows that predicted surface ozone by three different operation models (GEM-MACH, NAM-CMAQ, and WRF-Chem) have very different patterns and values over the lake and along the shore.

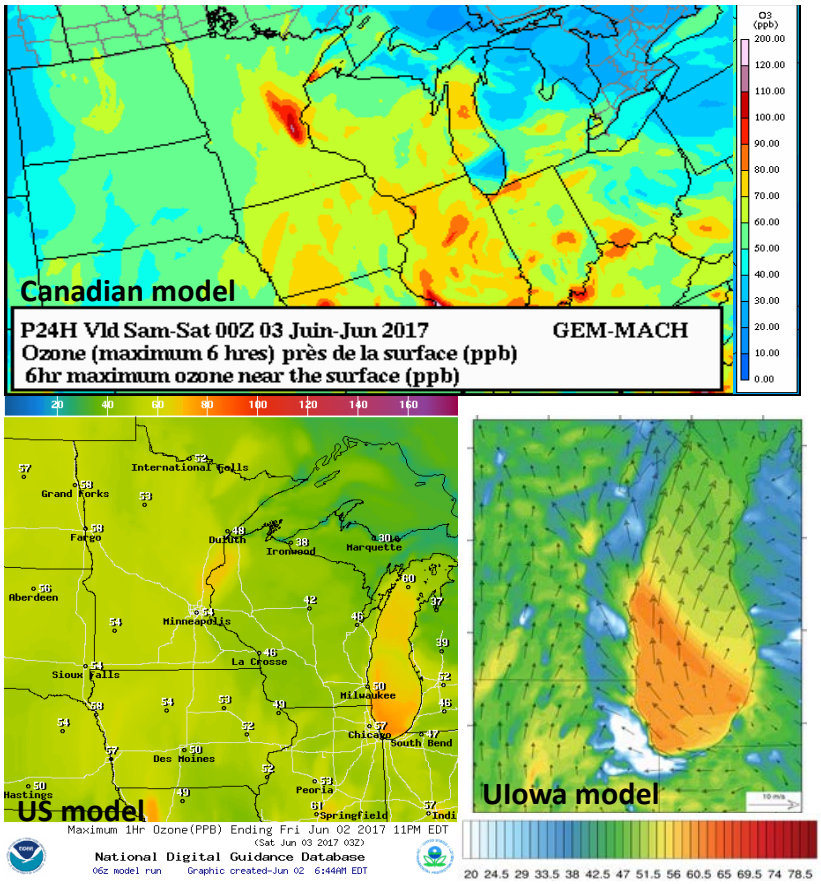

Figure 4-1 Predicted surface ozone concentration by GEM-MACH (Canadian; https://weather.gc.ca), NAM-CMAQ (US NOAA; https://airquality.weather.gov/), and WRF-Chem (University of Iowa; https://bio.cgrer.uiowa.edu/LMOS/) operational models for the late afternoon of 2 June 2017. Note the different legends for each plot

The Eureleian Gas and Aerosol Scalable Unified System Model (PEGASUS) meteorological-chemical model designed by Fast and Heilman (2003) overestimated ozone concentrations over the lake in summer 1999. Similarly, Cleary et al. (2015) observed high bias of ozone concentration over the lake in the NAM-CMAQ operational forecast in June and September 2009. It should be noted that both these models had 12km x 12km horizontal resolution which may not be able to capture lake breeze structure in the domain. Goldberg et al. (2014) Used nested WRF-CMAQ simulations with the highest horizontal resolution of 1.33km x 1.33km to simulate summertime ozone over Chesapeake Bay in 2011 and found high bias in predicted ozone concentration. Uncertainties in biogenic and anthropogenic emission inventories, errors in

capturing regional meteorology and physics of the stable layer in the model, and errors in chemical parametrizations are some of the potential reasons for the disagreements between models and measurements (Goldberg et al., 2014; McNider et al., 2018).

In this study, we use high-resolution (4km x 4km) WRF-Chem model and measurements from the Lake Michigan Ozone Study (LMOS 2017) to better understand the ozone formation and transport over the Lake Michigan and the surrounding regions. Some of the objectives of this study are to:

- assess the WRF-Chem performance in capturing meteorology and transport in the domain
- assess the WRF-Chem performance in capturing primary pollutant (such as NOx) and ozone concentrations and high ozone events associated with lake breeze
- assess the sensitivity of ozone concentration to different WRF-Chem physical parametrizations
- assess the sensitivity of ozone concentration to NOx and Hydrocarbon (HC) emissions

4.2 Method

4.2.1 LMOS field experiment

Lake Michigan Ozone Study (LMOS 2017) field experiment was conducted from 22 May to 21 June 2017 to address the ozone enhancements in the coastal communities around Lake Michigan. Two aircraft (NASA King Air and Scientific Aviation Mooney) and two ground-based super sites (Zion, IL and Sheboygan, WI) along with several remote sensing and in situ measurement sites and mobile sampling platforms were deployed during this field experiment to measure meteorological variables, ozone, ozone precursors, and particulate matter. The main goal of this field experiment was to better understand the ozone formation and transport over Lake Michigan and the surrounding region.

4.2.1.1 Measurements

NASA King Air and Scientific Aviation Mooney aircraft were used during the LMSO field experiment. NASA King Air aircraft conducted 21 flights in "raster" patterns and was equipped with Geostationary Trace gas and Aerosol Sensor Optimization instrument (GeoTASO) to measure NO_2 column and the University of Maryland-Baltimore Airborne Hyper Angular Rainbow Polarimeter (AirHARP) for cloud and aerosol measurements. Scientific Aviation operated Mooney aircraft and flew 22 flights in "spiral" patterns and measured temperature, relative humidity, H_2O, wind, in-situ ozone, NO_2, CO_2, and CH_4. The preliminary flight objectives for these two aircrafts were to sample along western shore of Lake Michigan during high-ozone event, characterize NO_2 emissions, and characterize costal gradients west of Lake Michigan.

Two main measurement stations were located at Zion super-site, IL (42.47N, -87.81W) and Sheboygan, WI (43.75N, -87.71W) to measure meteorological variables such as vertically resolved coastal winds, temperature, water vapor and in-situ ozone, NOx, NOy, formaldehyde (HCHO), VOCs, nitric acid, hydrogen peroxide, and aerosol characterization. A Microwave radiometer and acoustic wind profiler or Sonic Detection And Ranging (SODAR) measured wind profiles every 10m from 30 to 200m above ground level at Zion super-site. Remote sensing instruments such as ceilometers and UV/visible grating spectrometers (Pandora) were deployed to various sites across the domain (Figure 4-2). Two mobile platforms, EPA Region 5 Geospatial Monitoring of Air Pollution (GMAP) and UW-Eau Clair automobile platform, were deployed to measure in-situ ozone and ozone gradient between different locations. The LADCO Synthesis report (LMOS 2017 Study Team, 2018) includes details about all the instruments involved in LMOS 2017 field experiment.

Figure 4-2 Schematic of type of measurements and the approximate location of ground sites

4.2.1.2 University of Iowa Forecasting system

During the LMOS 2017 field experiment, forecast products from the 4km x 4km WRF-Chem modeling system were used as aids during the flight planning briefings. Besides University of Iowa model, operational NAM-CMAQ air quality forecasts from the National Weather Service (NWS) were used in the daily flight planning. We used a single domain WRF-Chem v3.6.1 to simulate the atmospheric transport and chemistry around Lake Michigan. Figure 4-3 illustrates the domain and the underlying terrain map. The domain covers Minnesota, Iowa, Missouri, Wisconsin, Illinois, Michigan, Indiana, and Ohio (37.6-48.8N and 95.45-81.46E) with 4km x 4km horizontal resolution or 310 x 260 grids. The domain has 53 vertical levels with domain top at 50hPa (~11 layers within the lowest 1km).

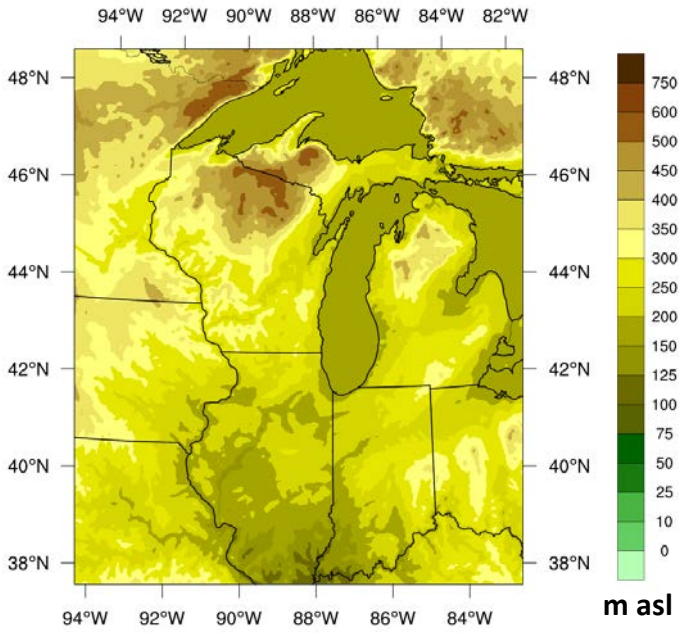

Figure 4-3 WRF-Chem domain and the underlying terrain map

Meteorological initial and boundary fields were retrieved from the National Center for Environmental Prediction (NCEP) Global Forecasting System (GFS) (National Centers for Environmental Prediction, National Weather Service, NOAA, 2000) (NCEP-FNL). European Centre for Medium-Range Weather Forecasts Monitoring Atmospheric Composition and Climate reanalysis (MACC) (Inness et al., 2013) was used as chemical boundary conditions. Table 4-1 summarizes the main WRF-Chem configurations used in the forecast simulations.

Table 4-1 Summary of WRF-Chem configuration used in forecast

Horizontal resolution	4km
Vertical resolution	53 layers (11 within the lowest 1km)
PBL Scheme	MYNN3
Surface layer	MYNN surface layer
Land Surface	5-layer thermal diffusion
Microphysics	Morrison double-moment scheme
Shortwave radiation	Goddard shortwave
longwave radiation	RRTMG scheme

Cumulus Parametrization	Grell-Freitas scheme
Gas-phase chemistry	RACM-ESRL
Biogenic emission	MEGAN
Lightening	OFF
Land use	USGS

We utilized the Regional Atmospheric Chemistry Mechanism using Earth System Research Laboratory (RACM-ESRL) (Stockwell et al., 1997) with updated reaction table for gas phase chemistry for the simulation. RACM_ESRL (Kim et al., 2009) is an updated version of RACM mechanism and includes 23 photolysis and 221 chemical reactions (Ahmadov et al., 2015a). The Modal Aerosol Dynamics Model/Secondary Organic Aerosol Model (MADE/SORGAM) was used for the aerosol option.

We used the Model of Emissions of Gases and Aerosols from Nature (MEGAN) version 2 for the biogenic emission in the simulations (Guenther et al., 2006). We did not include any fire emissions in the forecast simulations. The National Emission Inventory (NEI-2011v2) with 4kmx4km horizontal and hourly temporal resolution was re-gridded for the domain and used as anthropogenic emission inventory. Two separate 72-hr forecasts were initialized daily using re-gridded NEI-2011v2. In the base anthropogenic emission inventory, we decreased the NO_x emissions by 28% to account for the reduction in NO_x emission from 2011 to 2017 (https://www.epa.gov/air-emissions-inventories/air-pollutant-emissions-trends-data). In the second forecast NO_x emissions were reduced to 78% of total to account for uncertainties in NO_x emissions in NEI-2011v2 and test the sensitivity of ozone to NO_x concentrations in the forecast mode.

NCAR Command Language (UCAR/NCAR/CISL/TDD, 2017) was used to create surface map, cross-sections, ground-site time series (curtain plots) using the daily forecasts. These plots were

then uploaded to the website designed for the LMSO field experiment: https://bio.cgrer.uiowa.edu/LMOS. Spatial plots of 11 chemical species, 4 columns, and 10 meteorological products could be viewed at four pressure levels and the full domain or zoomed onto Lake Michigan. The cross-sectional plots with cloud and NO_2 contours overlaid on color contours of 10 chemical species were produced for three west-east and two north-south transects of the domain. Also, 11 ground sites were chosen to show curtain plots and time series graphs of nine chemical species, relative humidity, and temperature. We ran the two daily forecasts on the University of Iowa Argon cluster using 224 cores and each set of 72-hr forecast took about 9 hours to finish. Figure 4-4 illustrates the schematics of the forecasting system.

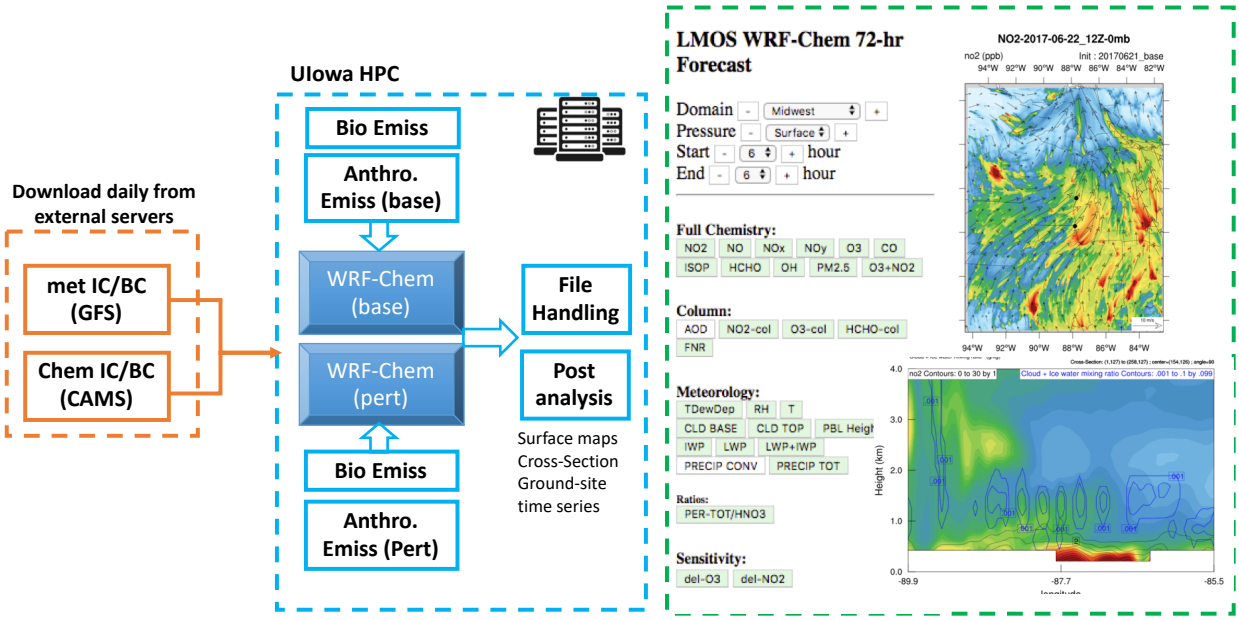

Figure 4-4 Schematics of UIowa WRF-Chem forecasting system

4.2.2 Post-campaign model description and sensitivity analysis

In the post-campaign analysis, the base WRF-Chem case used the same configurations as the forecast with some modifications. MODIS land use category was used in the post-campaign simulations. We re-initialized meteorological field daily at 00Z (7pm Local Time (LT)) using

NCEP-FNL fields and discard the first 6 hours to account for sufficient spin-up time and keep the next 24 hours (6Z or 1am LT to 6Z of the next day). MACC is used for chemical boundary conditions and initial conditions of the first cycle. For all the other cycles we used chemical fields from previous cycle.

We tested the sensitivity of the model to selection of meteorological boundary condition, initial condition, land surface model parameterization, planetary boundary layer scheme, and update of SST. We also evaluated the sensitivity of ozone and ozone production to changes in NOx, Hydrocarbon (HC) and biogenic NOx emissions. Table 4-2 shows the list of sensitivity tests.

Table 4-2 List of sensitivity tests and main configurations and emissions

	Sim ID	Emission	LSM	Met IC/BC	PBL	SST	Chem Mech.
Physical parametrizations	base	NEI11-0.72NOx	5-layer	GFS (1 deg)	MYNN3	Default	RACM
	Base_sst	NEI11-0.72NOx	5-layer	GFS (1 deg)	MYNN3	GLERST SST	RACM
	Base_HRRR	NEI11-0.72NOx	5-layer	HRRR (3km)	MYNN3	Default	RACM
	HRRR_noah	NEI11-0.72NOx	Noah	HRRR (3km)	MYNN3	Default	RACM
Emission Scenarios	0.22NOx	0 NEI11-.22NOx	5-layer	GFS (1 deg)	MYNN3	Default	RACM
	0.72NOx_5HC	NEI11-0.72NOx_5HC	5-layer	GFS (1 deg)	MYNN3	Default	RACM
	0.72NOx_10HC	NEI11-0.72NOx_5HC	5-layer	GFS (1 deg)	MYNN3	Default	RACM
	0.72NOx_2Iso	NEI11-0.72NOx_2Iso	5-layer	GFS (1 deg)	MYNN3	Default	RACM
	HRRR_0.72NOx_5HC	NEI11-0.72NOx_5HC	5-layer	HRRR (3km)	MYNN3	Default	RACM

4.3 Overall Model Performance

4.3.1 Meteorology

In this section we discuss the base model performance in capturing meteorology and chemistry fields over the course of the campaign (22 May to 21 June 2017). Figure 4-5 shows temperature and dewpoint temperature in the base model and hourly measurements at Waukegan National Airport (42.42N, -87.87W) which is the closest METeorological Aerodrome Report (METAR) station to the Zion super-site (~16km southwest of Zion super-site and ~26km from the shoreline). Overall, the base model captured the synoptic variability of temperature well but had low biases in minimum and maximum temperature. Model overestimated Dewpoint temperature specially during 28 May to 15 June 2017. Most of the sensitivity simulations do not cover 22 May to 31 May 2017 to reduce the computational costs. Thus, to calculate statistics in the base case and be able to compare with other sensitivity simulations we only considered 31 May to 21 June 2017. Table 4-3 summarizes the model performance during the campaign period. Overall, high correlation (R), and Index of Agreement (IOA) between measured and base model temperature and dewpoint temperature were observed which indicate that model captured the variations well. Negative bias in temperature and positive bias in dewpoint temperature resulted in MB of -1.45^{o}C and 1.87^{o}C, respectively.

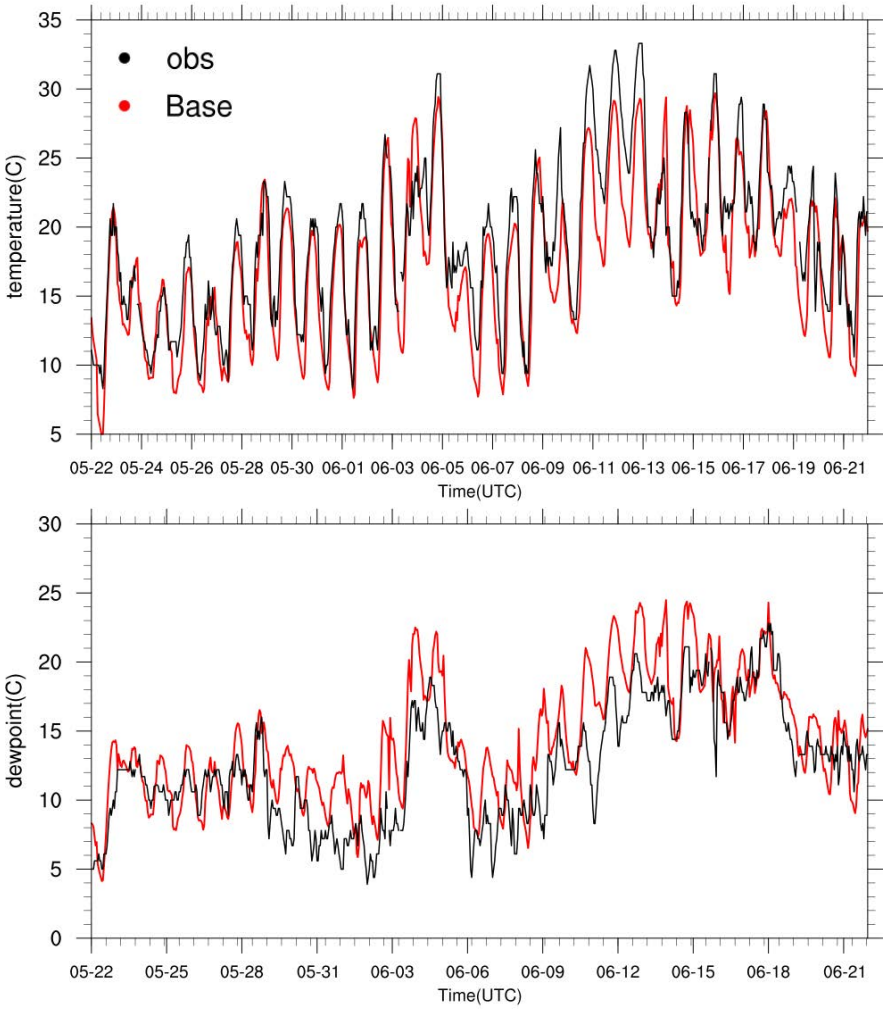

Figure 4-5 Timeseries of modeled and measured hourly temperature and dewpoint temperature at Waukegan National Airport (Zion, IL)

Table 4-3 Model performance in capturing temperature and dewpoint temperature at Waukegan National Airport (Zion, IL) from May 31 to June 21, 2017

BASE	R	MAE	RMSE	MB	MNE	MNB	IOA
T (C)	0.89	2.48	2.97	-1.45	0.14	-0.07	0.92
Dew Point (C)	0.81	2.52	3.25	1.87	0.26	0.20	0.86

Comparisons of modeled temperature at other METAR stations across the domain (Figure 4-6) shows daytime (10am-6pm LT) biases up to -4°C along the shore of Lake Michigan and daytime biases up to -8°C on the east of the lake. Positive biases were observed during the nighttime

(10pm-6am LT) across the domain. South of the domain showed slight positive biases (up to 3°C) during daytime and higher positive biases (up to 8°C) during nighttime. Overall, dewpoint temperature was overestimated during both daytime and nighttime and across the domain. South and southwest of the domain show larger biases (up to 8°C) and east of lake Michigan show smaller biases (up to 2 °C).

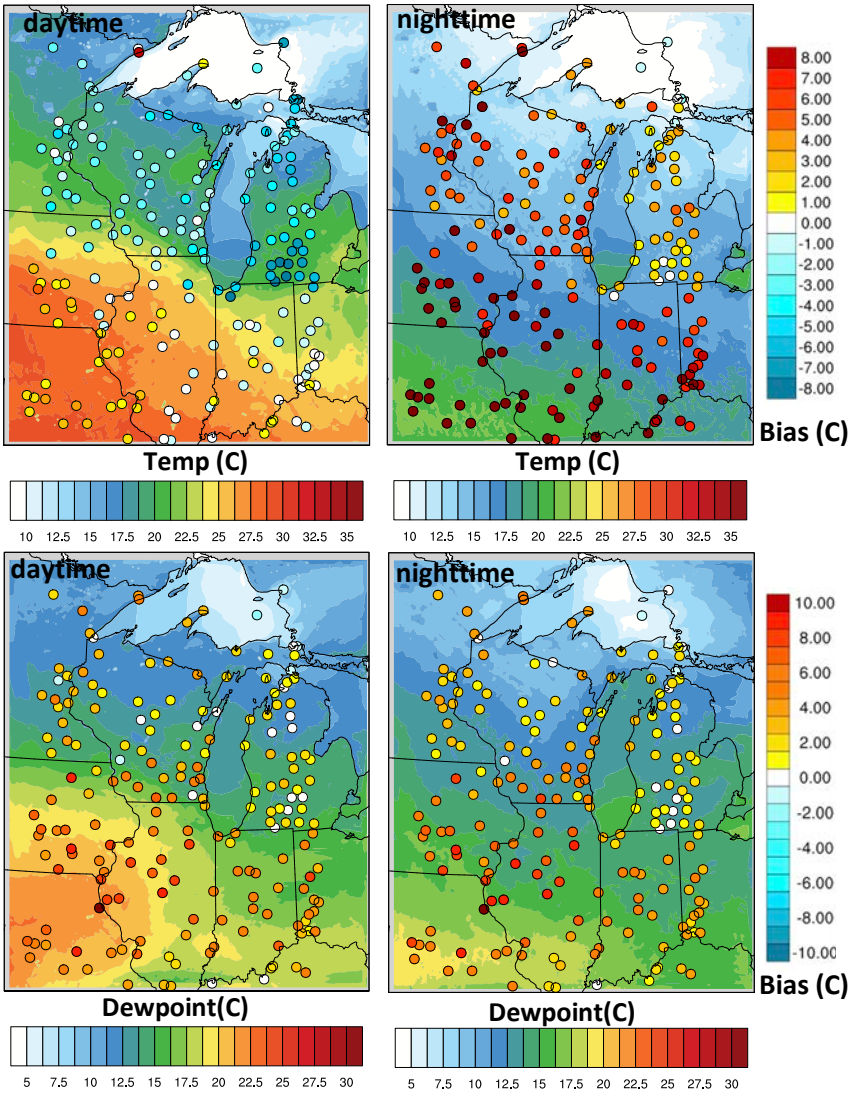

Figure 4-6 Average biases in base model temperature and dewpoint temperature at METAR stations at daytime (10am-6pm LT) and nighttime (10pm-6am LT) during 31 May to 21 June 2017

We compared the base model temperature and relative humidity with measurements by Scientific Aviation (SA) aircraft during the spirals over land and over the lake. Figure 4-7 shows that the model very well captured the vertical changes in the temperature and relative humidity. The variation (length of the boxplot) in each bin was well captured in model for both temperature and relative humidity. The biases observed in the ground-based stations can be observed at higher altitudes aircraft measurements. Model underestimated temperature over both land and lake and at higher altitudes. Model predicted higher relative humidity with higher biases over the lake and lower altitudes.

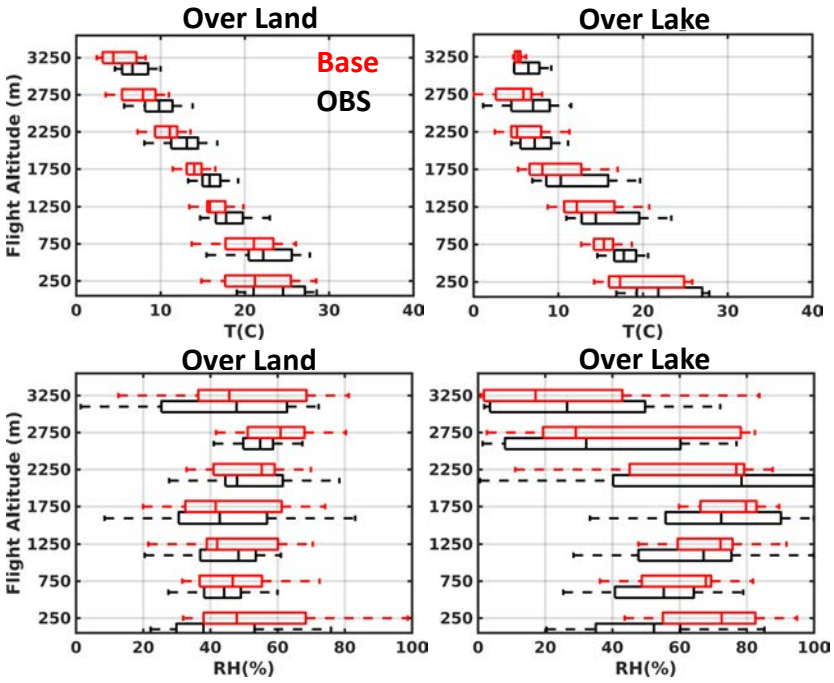

Figure 4-7 Vertical distribution of temperature and relative humidity measured by Scientific Aviation spirals over land and over the lake and the corresponding base model values during 31 May to 22 June, 2017

Wind fields are also important parameters impacting the atmospheric transport. In general, base model captured the diurnal variation of wind speed and direction well at Waukegan National Airport (Zion, IL) (Figure 4-8). During 29 May to 1 June 2017 westerly wind with low variation

in wind direction were measured. Model overestimated the wind speed in this period but capture the low variation in the wind direction correctly. On 2 June, a shift from afternoon southwesterly to southeasterly winds were capture in the model but with a couple of hours of delay. Comparisons of modeled wind speed with other METAR stations indicates overall good agreement with daytime measurements with small negative bias in stations close to the shore. Although model predicted lower nighttime wind speed over the land, but even lower wind speeds were measured at most the stations across the domain.

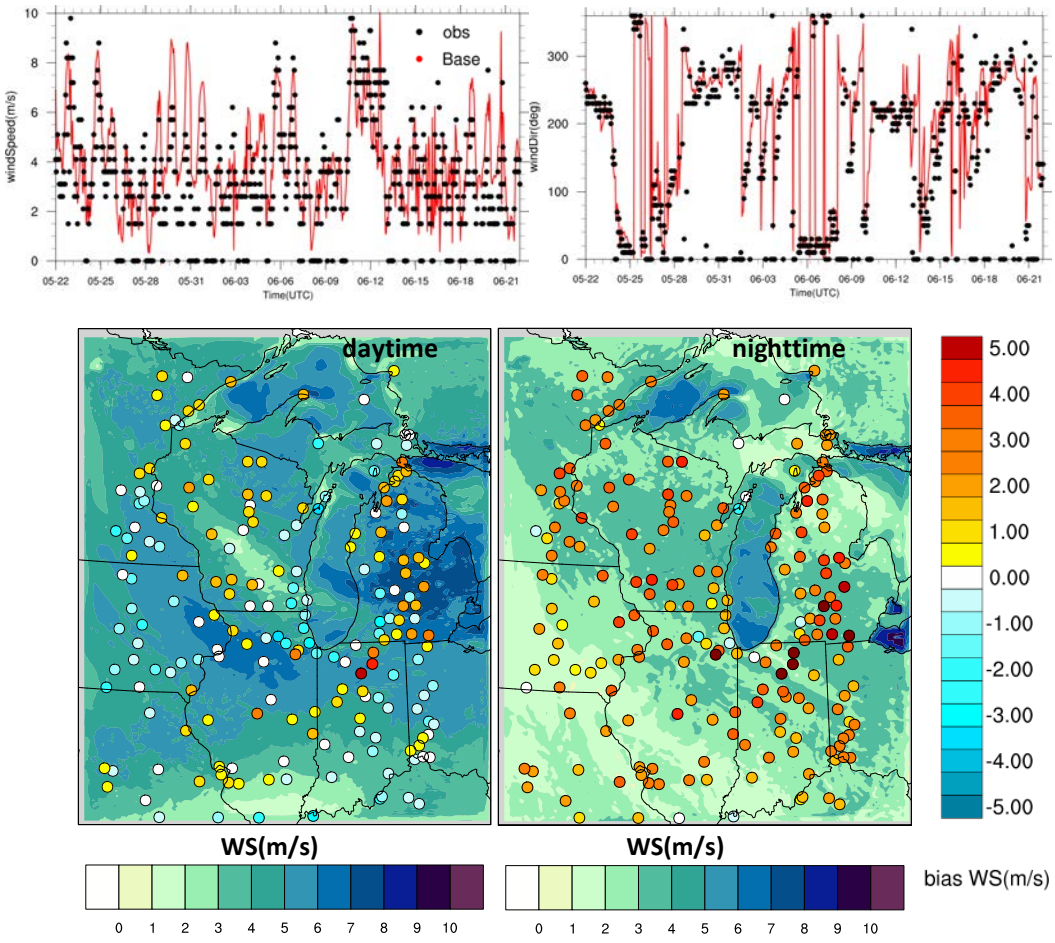

Figure 4-8 Top row plots: timeseries of base modeled and measured wind speed and direction at Waukegan National Airport (Zion, IL). Bottom row plots: average biases in base model nighttime and daytime wind speed at METAR stations at daytime and nighttime during 31 May to 21 June 2017

The negative biases in temperature and positive biases in relative humidity (and dewpoint temperature) suggests an error in partition of latent heat and sensible heat in the model. Soil moisture is one of the factors that can impact this partitioning (Huang et al., 2017; Jin et al., 2010). The 5-layer thermal diffusion LSM used in the base model is a simplified LSM which calculates the soil temperature in 5 layers but does not account for soil moisture. Using a more detailed LSM such as Noah (Chen and Dudhia, 2001) was tested as one of the sensitivity tests. Having a low bias in temperature at higher altitude was the main motivation for testing different meteorological boundary condition such as High-Resolution Rapid Refresh (HRRR) forecast.

4.3.2 Chemistry

In this section we discuss general trends of ozone and NOx in the domain and the model performance. Measurements of other species such as formaldehyde and isoprene are available and are discussed in section 4.6 emission sensitivity

Comparison between measured ozone at the EPA monitors at Zion (42.5N, -87.81W) and Chicago (42.1N, -87.9W), Figure 4-9, shows that model generally reproduced the diurnal variability in observed ozone, however consistently underpredicted the maximum ozone values. Lower nighttime ozone was measured at Chicago site due to destruction of ozone with other available pollutants in the urban environment which was captured by the model.

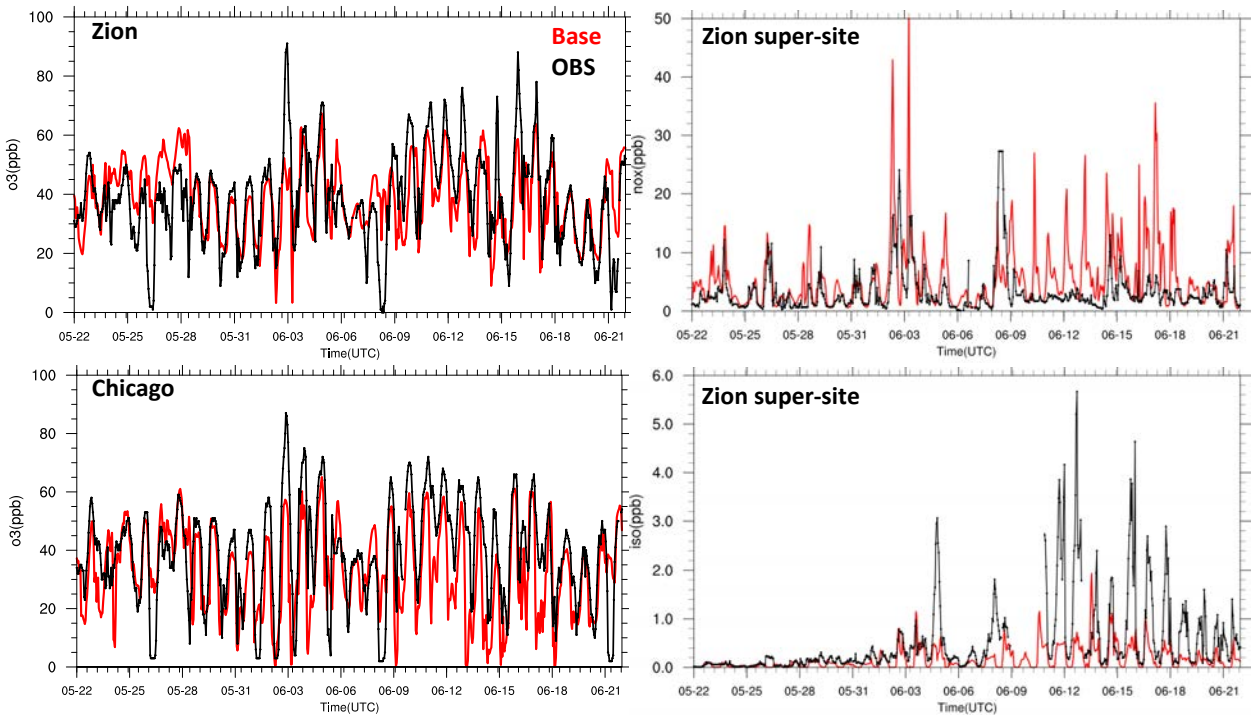

Figure 4-9 Timeseries of modeled and measured hourly ozone at EPA sites in Zion and Chicago and NOx and isoprene (iso) at Zion super-site

Model captured the NOx concentration at Zion super-site well on the first half of the campaign (22 May to 6 June 2017) and the second half model predicted high NOx concentration and strong diurnal variation which was not observed in the measurements (Figure 4-9). Unlike the model, measurements showed very weak diurnal variation in NOx in the second half compared to the first half of the campaign.

Isoprene is one of the major biogenic Volatile Organic Compounds (VOCs) with a short lifetime (1-2 hours) (Guenther et al., 2012). Low concentration of isoprene was measured from 22 May to 3 June 2017 and model successfully captured these low values. With increase in green vegetation fraction and increase in biogenic emissions in June higher isoprene concentration was measured. Model also showed an increase in isoprene concentration in June but at a much lower magnitude.

Table 4-4 summarizes hourly and 8-hr maximum model performance for ozone at Zion and Chicago sites. On average higher ozone concentrations were measured at Zion (with higher absolute bias) compared to Chicago. 8-hr maximum statistics showed bias of -5.3 ppb at Zion and 1.2 ppb at Chicago.

Table 4-4 Summary of hourly and 8-hr peak statistics of base model performance in capturing ozone at EPA sites (Zion and Chicago)

0.72NOx (base)	Hourly O3 (ppb)						8hr peak O3 (ppb)				
	n	R2	RMSE	mod mean	obs mean	bias	n	R2	mod mean	obs mean	bias
Zion	467	0.35	14.2	38.1	41.5	-3.4	19	0.38	51.3	56.6	-5.3
Chicago	466	0.56	11.3	33.8	34.3	-0.5	18	0.7	49.2	48	1.2

Daytime mean bias at other EPA stations also show negative bias for ozone across the domain except for south side of the domain. During the nighttime model mostly, overestimated ozone concentration with higher biases for south of the domain. The high bias in the south can be due biases in ozone in boundary conditions (MACC model).

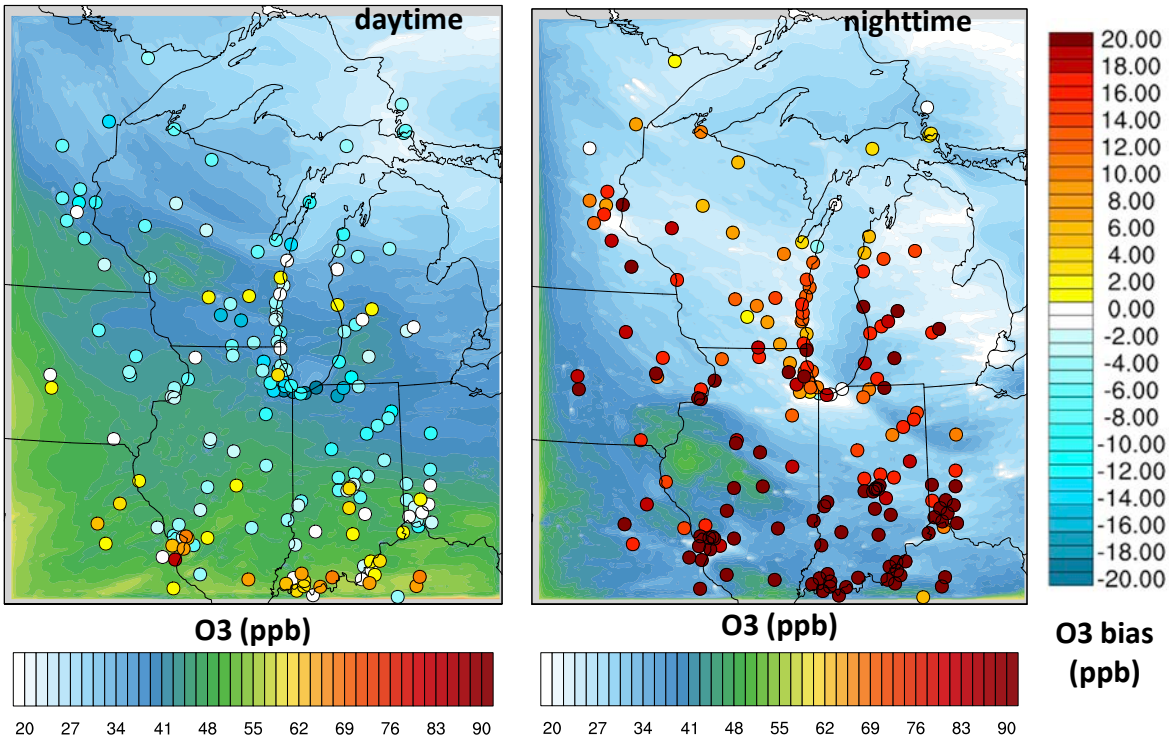

Figure 4-10 average mean surface ozone and mean bias for base model at EPA stations separated by daytime (10am-6pm LT) and nighttime (10pm-6am LT)

We assessed the sensitivity of ozone and ozone production to changes in NOx, HC, and biogenic emissions by running WRF-Chem with different emission scenarios. In NOx-reduction scenarios, we reduced NOx by different factors to better match the measurements. In HC-increased scenarios we increased the anthropogenic emissions and in biogenic-increased we increased the biogenic isoprene emissions by different factors. Section 4.5 includes details on each of the emission scenarios.

4.4 Sensitivity to Physical Parametrization

To improve the model performance in capturing temperature and relative humidity we tested different model configurations and set-ups such as updating lake surface temperature with measured data, using more sophisticated Land Surface Model (LSM), and using High-Resolution Rapid Refresh (HRRR) meteorological initial and boundary conditions. In this section we

describe the sensitivity of temperature, relative humidity, wind fields, and ozone to each of these changes.

4.4.1 Lake surface temperature

Lake surface temperature (hereafter SST) can play a role in transport and stability of its surrounding region. Fast and Heilman (2003) showed changes of 5°C in Lake Michigan temperature can change ozone concentration by up to 50ppb which can be minimized to up to 10ppb by the stronger synoptic forcing.

In the default set-up WRF uses simple interpolation to calculate SST fields from the intermediate files (created from global model output) which may have a low resolution (i.e., 1 degree for NCEP-FNL). In the base simulation SST varies daily. For the sensitivity simulation we replaced the default SST with the NCEP Global Data Assimilation System (GDAS) 1/12th degree SST analysis. Figure 4-11 shows the WRF simulation with updated SST predicted up to 5°C warmer SST compared to the base simulation. These differences are higher on the east side of the lake and resulted in 0°C to 4°C increase in the air temperature above the lake. The changes in air temperature had a small impact on surface wind over the lake and the shore (not shown). Similarly, ozone did not show a strong sensitivity to increase in air temperature (less than 2ppb on the East side). The ozone sensitivity to changes in air temperature over the lake contradicts with high sensitivities discussed by Fast and Heilman (2003) in 1999. This can be due to differences between chemical mechanism used in the two simulations or different chemical regime caused by different emission rates in 1999 compared to 2017.

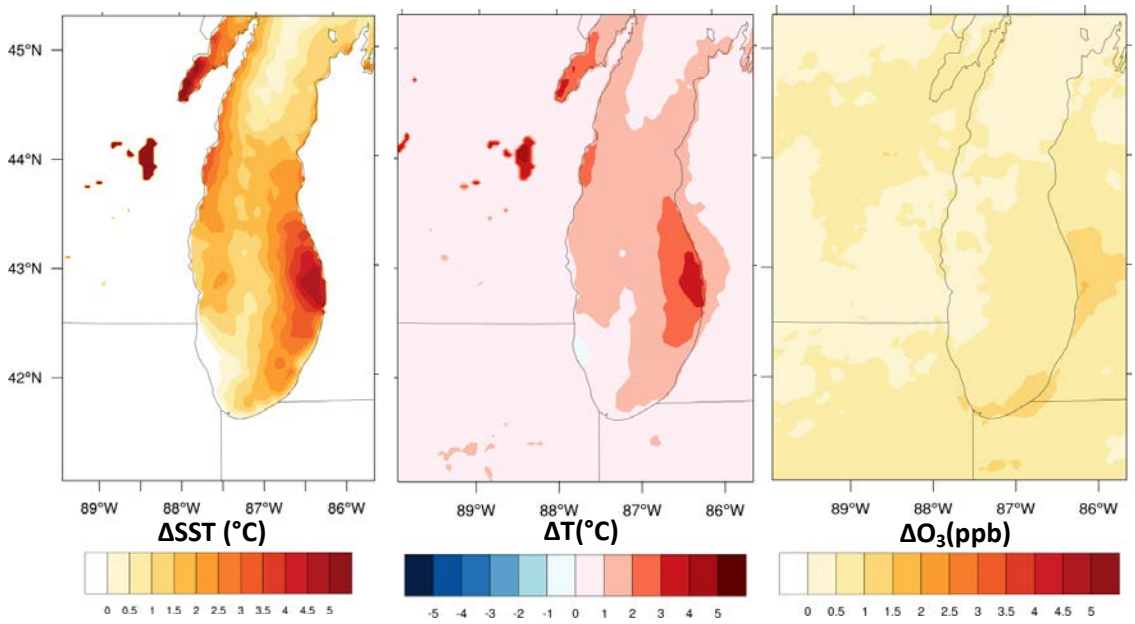

Figure 4-11 differences in SST, surface temperature (T), and ozone between updated SST (with NCEP GDAS) and base simulation. $\Delta x = X_{base\_SST} - X_{base}$

4.4.2 Meteorological initial and boundary conditions

The single WRF-Chem domain designed for the LMOS experiment is a relatively small. Thus, we expect to see large influence of meteorological boundary conditions on the model performance. NCEP-FNL with 1-degree resolution was used in the base simulation. High-Resolution Rapid Refresh (HRRR) is a high resolution (3km x 3km) hourly updating, cloud-resolving, convection-allowing operational forecast system with assimilation (Benjamin et al., 2016). We downloaded HRRRv2 from HRRR archive at University of Utah (Blaylock et al., 2017) for the period of LMOS field experiment. We did not conduct any nudging in these two simulations; however, reinitialized the simulation every day (with 6 hours spin up).

Simulation with HRRR meteorological initial and boundary conditions (base_HRRR) predicted on average up to 3°C higher surface temperature compared to simulation with NCEP-FNL meteorological initial and boundary conditions (base) with higher sensitivity on the east side of the domain (Figure 4-12). Increase in temperature resulted in up to 4ppb increase in ozone

(mostly East of the domain). Dewpoint temperature and windspeed showed lower sensitivity to this change (not shown).

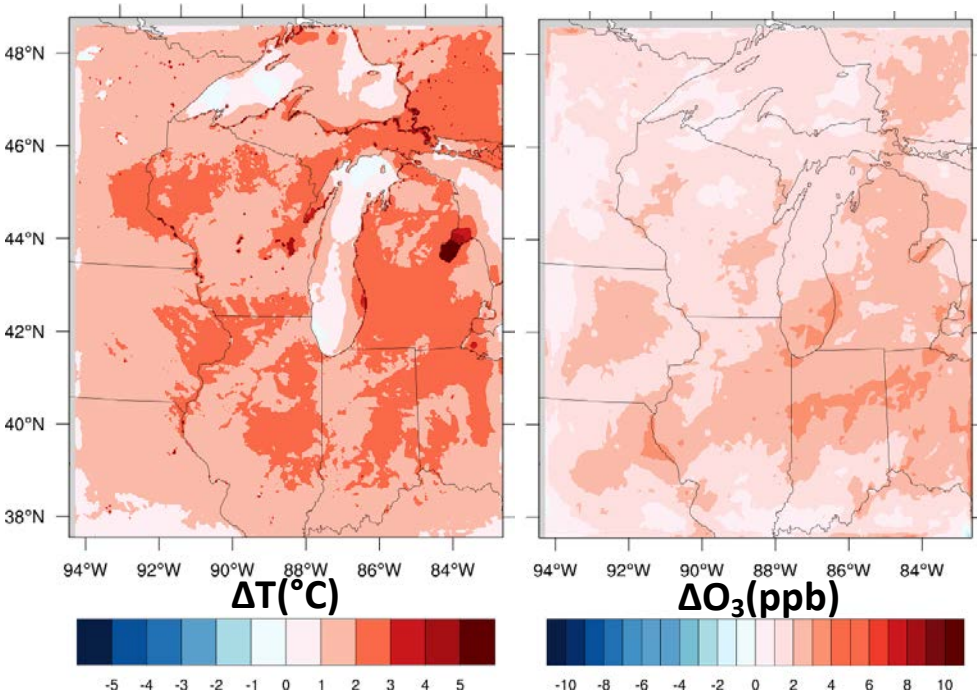

Figure 4-12 differences between base_HRRR and base model mean surface temperature and mean surface ozone. $\Delta x = X_{base\_HRRR} - X_{base}$

Comparisons with Waukegan National Airport (Zion, IL) measurements (Figure 4-13) show improvements in capturing minimum temperature values in base_HRRR simulation but not in dewpoint temperature, windspeed, and wind direction. Timeseries of ozone at EPA Zion and Chicago sites do not show strong sensitivity of ozone to the changes in temperature at these sites (Figure 4-13). Overall, base_HRRR simulation slightly improved the model performance in capturing temperature but did not have a large impact on dewpoint temperature or ozone on the westside of the Lake. The increase in the temperature only increased isoprene concentration by up to than 0.4ppb (not shown).

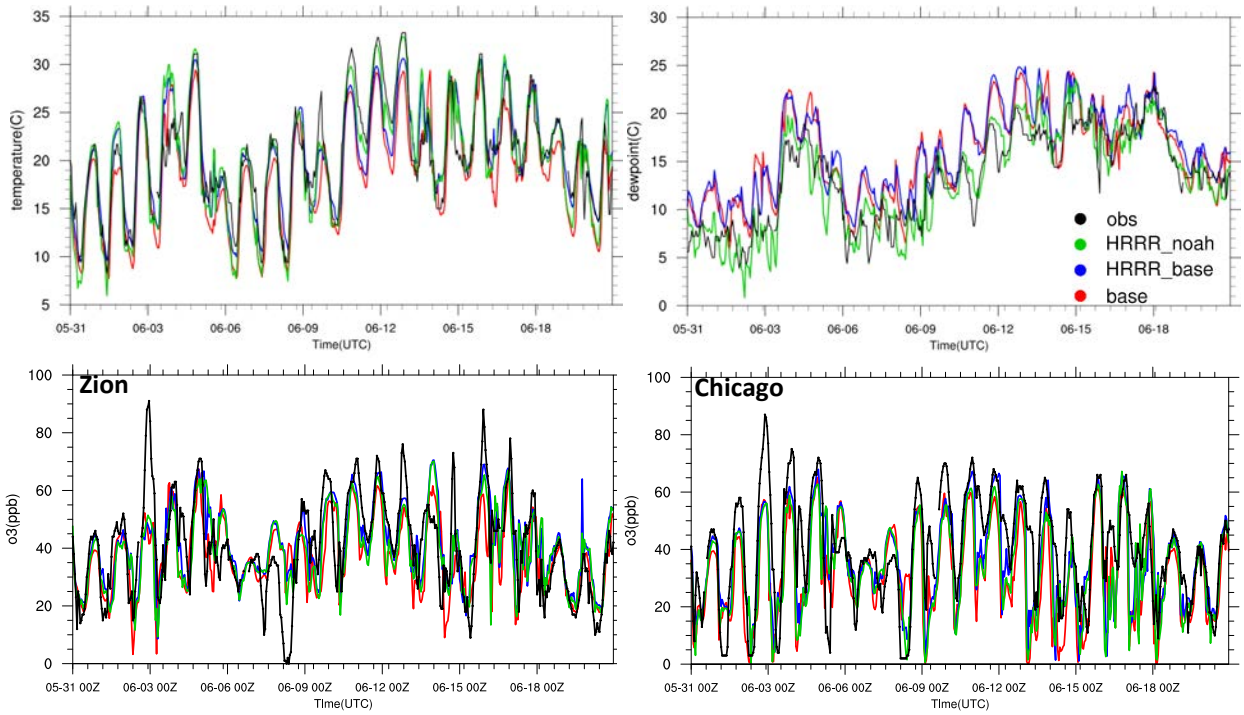

Figure 4-13 Top row: timeseries of modeled and measured hourly temperature, dewpoint temperature at Waukegan National Airport (Zion, IL). Bottom row: timeseries of modeled and measured hourly ozone at EPA Zion and Chicago sites

4.4.3 Land surface model

Land Surface Model (LSM) can play an important role in regional climate. It involves the interaction between land surface and atmosphere through exchange of energy, mass, and momentum (Chen et al., 2014). We compared the performance of a simple LSM (5-layer) thermal diffusion with a more sophisticated LSM (Noah). Noah LSM (Chen and Dudhia, 2001) with four soil layer thicknesses of 0.1m, 0.3m, 0.6m, and 1m calculates soil moisture for each layer. Soil moisture can play an important role in partitioning between latent heat and sensible heat in the model and thus air temperature and relative humidity. We used HRRR meteorological initial and boundary conditions in the LSM simulation test (HRRR_noah) because of its prior performance in capturing temperature. Additionally, by using HRRR model we provide high

resolution soil moisture initial values in the simulation. Table 4-2 includes details on the HRRR_noah simulation.

Changes in surface temperature in HRRR_noah simulation (Figure 4-14) is very similar to base_HRRR which suggest that changes in temperature is mostly influence by to using HRRR meteorological initial and boundary conditions. HRRR_noah simulation predicted up to 5^{o}C lower dewpoint temperature across the domain with largest sensitivity at the south of the Lake. Changes in ozone is very similar to base_HRRR with slightly lower sensitivity.

Comparisons with ground-based measurements (Figure 4-13) show improvement in capturing minimum and maximum temperature in HRRR_noah simulation especially on 10, 11, and 12 June 2017. Dewpoint temperature was largely improved in the HRRR_noah simulation at Waukegan National Airport (Zion, IL) (Figure 4-13) and across the domain (Figure 4-14). This shows the significant impact of soil moisture on dewpoint temperature and temperature in this region. The changes in temperature and dewpoint temperature had small impact on ozone (Figure 4-14) and isoprene (not shown) concentration at EPA Zion and Chicago sites.

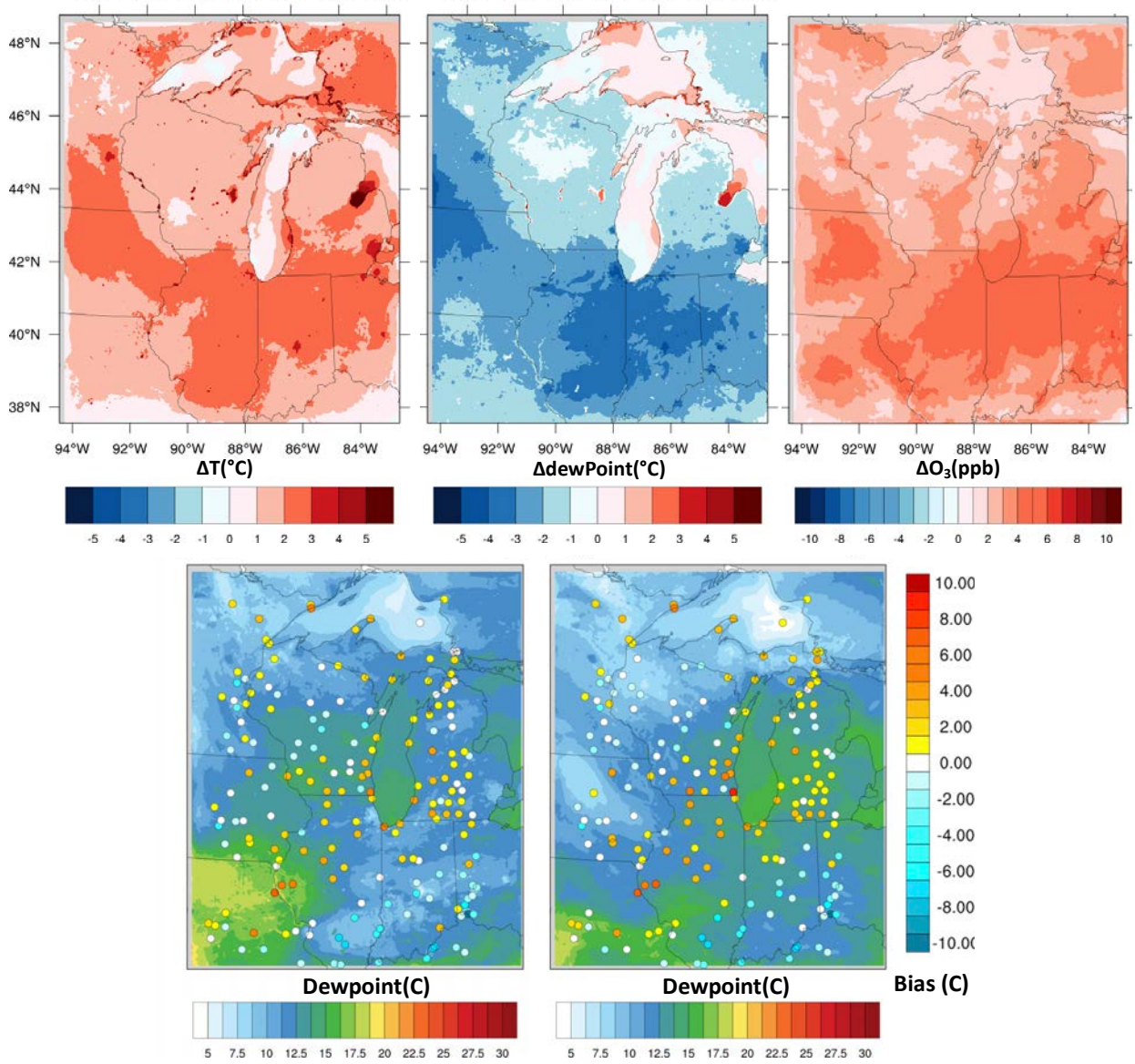

Figure 4-14 Top row: differences between HRRR_noah and base model mean surface temperature, mean surface dewpoint temperature, and mean surface ozone. $\Delta x = X_{HRRR\_noah} - X_{base}$. Bottom row: average biases in HRRR_noah model dewpoint temperature at METAR stations at daytime (10am-6pm LT) and nighttime (10pm-6am LT)

Figure 4-15 shows the vertical distribution of temperature and dewpoint temperature measured by Scientific Aviation (SA) and the corresponding base, base_HRRR, and HRRR_noah values over land and over the lake. The temperature over both land and the Lake was improved in HRRR_base and HRRR_noah simulations, especially at the lowest altitude. Overall, HRRR_base and HRRR_noah predicted similar temperature with slightly higher (improved)

prediction by HRRR_noah at the lowest altitude over land. Relative humidity was more sensitive to the changes in the meteorology initial and boundary conditions compared to temperature. Base_HRRR and HRRR_noah simulations both predicted lower relative humidity (closer to the measurements) over land and over the Lake within the PBL height. At higher altitudes relative humidity is higher in Base_HRRR and HRRR_noah compared to the base simulation and measurements, especially over the Lake. This could indicate a high bias in relative humidity of HRRR model compared to aircraft measurements.

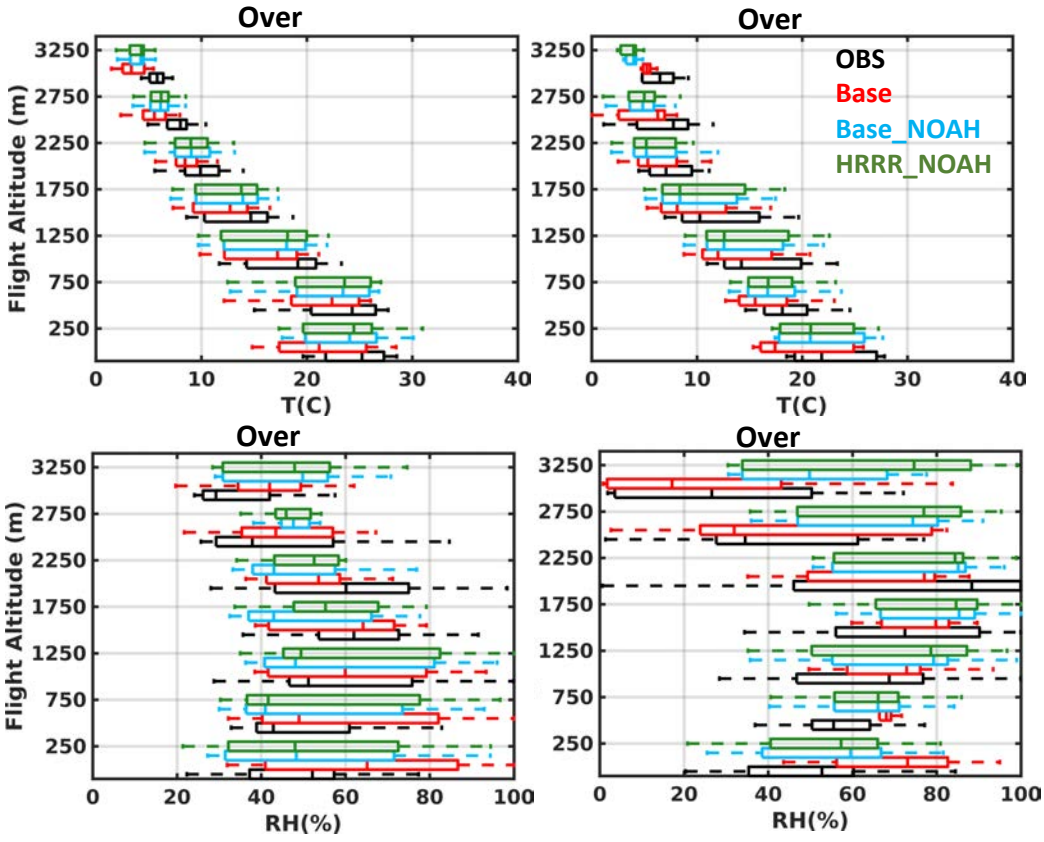

Figure 4-15 Vertical distribution of temperature and relative humidity measured by Scientific Aviation spirals over land and over the Lake and the corresponding base, base_HRRR, and HRRR_noah model values

4.5 2 June 2017 High Ozone Event

During the LMOS field experiment, high ozone events occurred on 2 June, 11-12 June, and 14-16 June 2017. The highest ozone concentrations were recorded on 2 June 2017 and the maximum ozone concentration at EPA Zion site was ~90ppb. The Model did not capture the enhancements min the ozone concentration on 2 June and had a bias of ~-50ppb at EPA Zion site and ~-30ppb at Chicago site.

On 2 June 2017 a strong lake breeze occurred which resulted in high ozone concentrations along the west shore of Lake Michigan in the afternoon. SODAR measurements at Zion super-site (Figure 4-16) shows a shift from southwesterly winds to southeasterly winds at 15 UTC (10am LT). The base model predicted a stronger westerly component prior to occurrence of the lake breeze. The lake breeze occurred later in the day in the base model at 19 UTC (2pm LT). HRRR_noah simulation precited the lake breeze earlier in the day at 16 UTC (11am LT) (not shown).

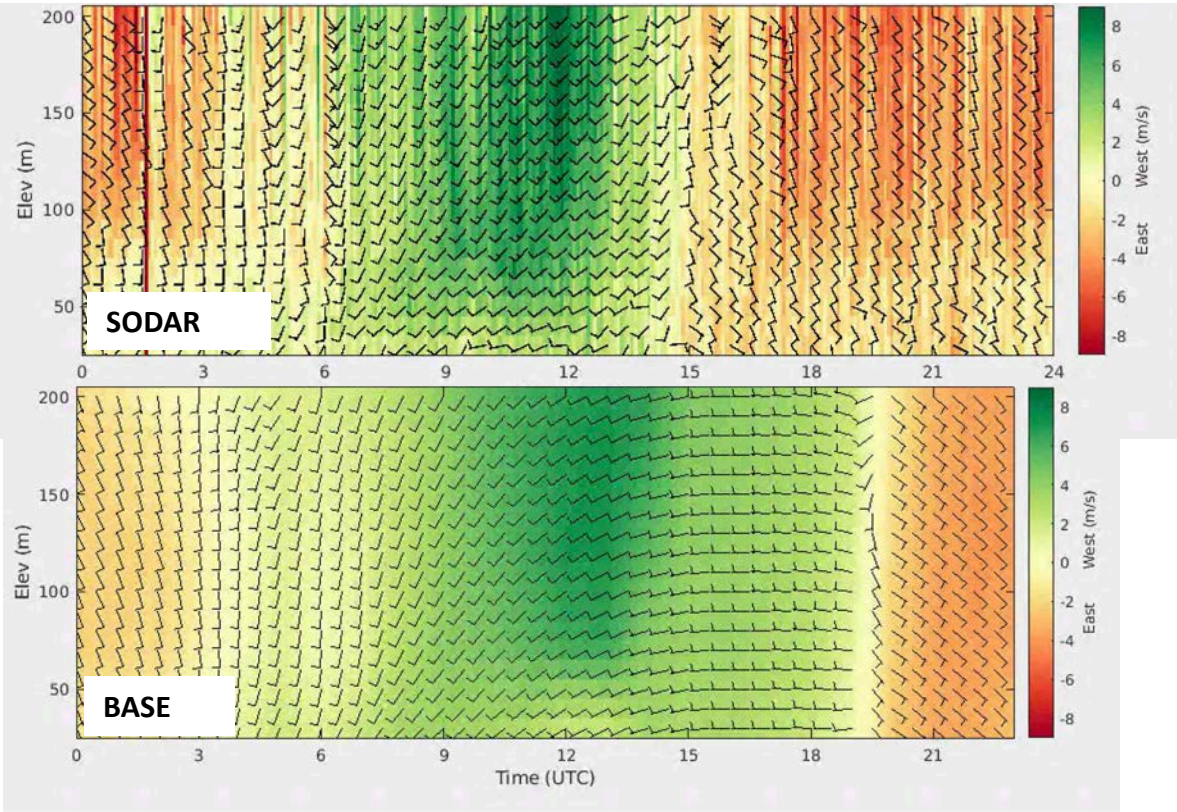

Figure 4-16 SODAR measurement and base model wind at Zion super-site on 2 June 2017

Surface concentrations of ozone and NOx at 2pm LT and 6pm LT and measured ozone concentration at the EPA sites are shown in Figure 4-17. The lake breeze (Starting at 10am LT) transported the air over the lake to the land. High ozone concentrations were measured at the stations along the shore. A sharp gradient in the ozone concentration, from high values to low values, between the shore and further inland was observed by the mobile platform (LMOS 2017 Study Team, 2018).

Model predicted high concentrations of NOx and low concentrations of ozone over the lake at 2pm. Later in the afternoon strong lake breeze with southwesterly winds transported the high NOx-low ozone plume northward over the lake and inland and resulted in a band of high NOx-low ozone along the shore. Model captured the gradient (band) caused by the lake breeze but

instead of high concentrations of ozone, the model predicted low values of ozone along the shore.

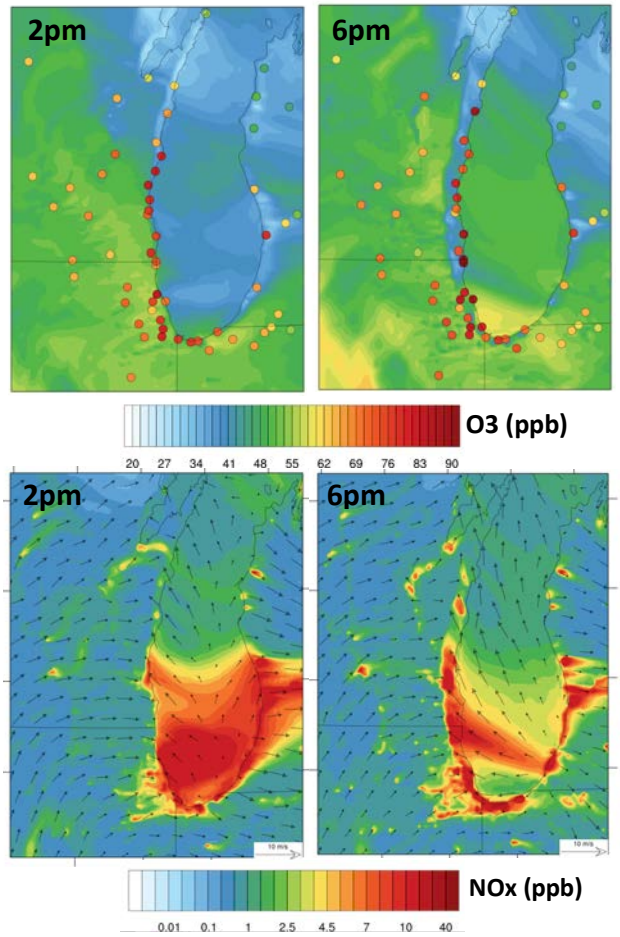

Figure 4-17 Surface ozone (top row) and surface NOx (bottom row) concentrations on 2 June during the Lake breeze event. Circles show the measured ozone concentration at EPA sites

4.5.1 Sensitivity to NOx and HC emissions

We further investigated the ozone formation in the domain on 2 June 2017 by testing the sensitivity of ozone formation and concentration to NOx and Hydrocarbon (HC) emissions in the WRF-Chem simulation. We changed the emission rates of anthropogenic NOx and anthropogenic HC and biogenic isoprene in the domain. Table 4-2 includes details about each of

sensitivity simulations. Base simulation set-ups and parametrizations were used for the emission sensitivity simulations.

Figure 4-18 shows the sensitivity of ozone and NOx concentrations to changes in HC (left column) and NOx (right column) emissions. Peak ozone concentration on 2 June did not show strong sensitivity to changes in emission at EPA Chicago site but showed sensitivity to changes in HC emissions at EPA Zion site. The HC sensitivities increased the HC emissions across the board by a factor of 5 (5HC) and 10 (10HC). Increasing the HC emissions by a factor of 5 (0.72NOx_5HC and 0.5NOx_5HC) increased the simulated ozone by ~50 ppb at EPA Zion and ~5 ppb at the EPA Chicago site. Increasing the HC emissions by a factor of 10 (0.72NOx_10HC) produced additional simulated ozone at Zion but resulted in no significant change in ozone at the Chicago site. Doubled biogenic isoprene emission (in 0.72NOx_2Iso) did not have a large impact on ozone concentration.

In a reduced NOx simulation, NO_x emissions (from all sources) were decreased by 50% ($0.22NO_x$). This sensitivity resulted in ~20ppb increase in ozone concentrations at EPA Zion site and ~10ppb reduction in ozone concentrations at the EPA Chicago site. Peak NOx concentration measure on June 2 at 18Z (1pm LT) at Zion super-site was not captured in any of the simulations which suggests an error in transport. All simulations except 0.22NOx overestimated NOx concentrations at Zion super-site during this event.

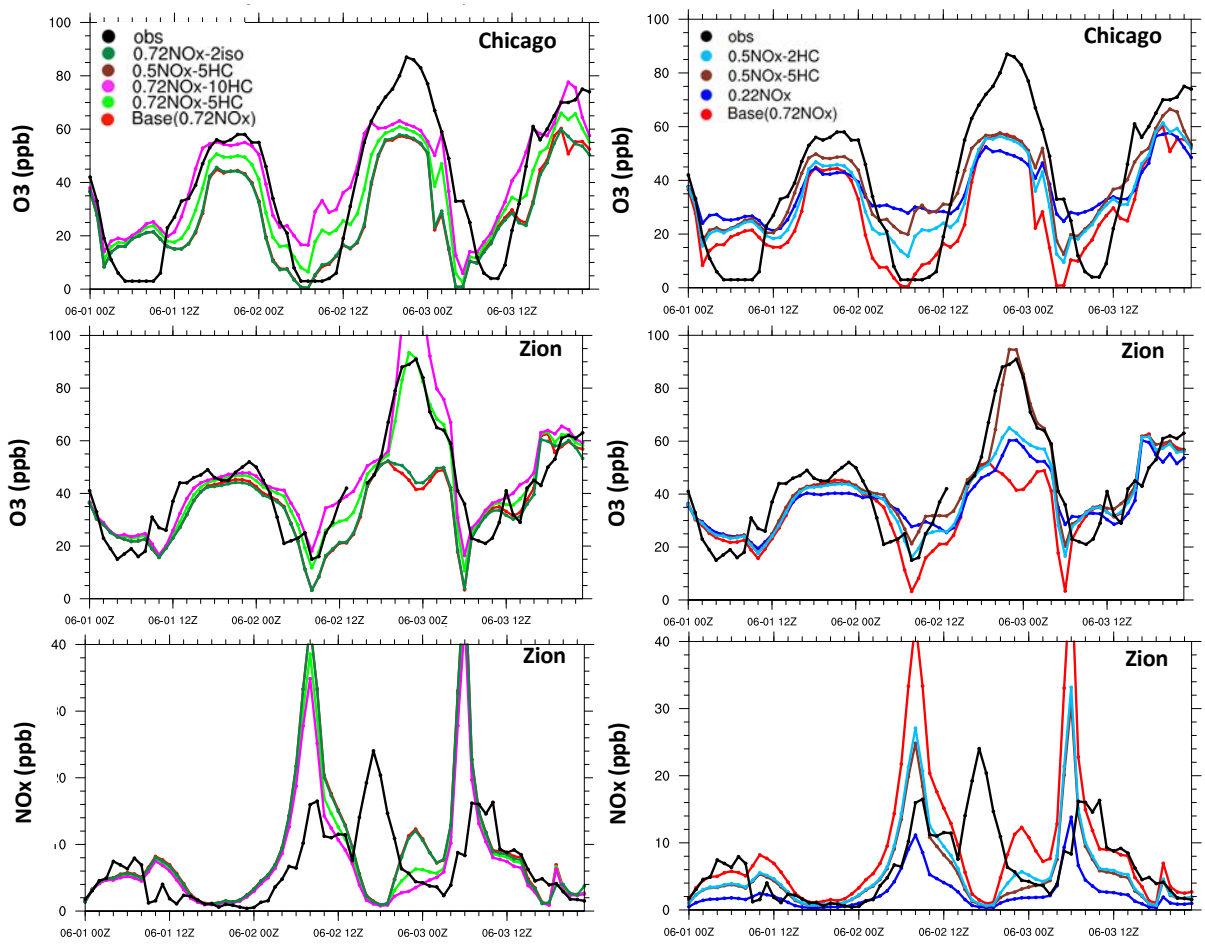

Figure 4-18 Timeseries of ozone at EPA Zion and Chicago sitrs and NOx at Zion super-site from June 1 to 4. Left column includes the HC sensitivity simulations and right column includes NOx sensitivity simulations

4.5.2 Biogenic emissions

Terrestrial ecosystems produce significant amounts of VOCs (Lamarque et al., 2010) and can impact the atmospheric chemistry. Isoprene (C_5H_8) is the most abundant biogenic VOC (BVOC) with a short life-time of 1-2 hours (Seinfeld and Pandis, 2012). Methacrolein (MACR) and methyl vinyl ketone (MVK) are stable products of high-NO oxidation of isoprene. Formaldehyde and glyoxal are also other important products of isoprene oxidation. We used the Model of Emissions of Gases and Aerosols from Nature (MEGAN) version 2 (Guenther et al., 2006) to calculate biogenic emissions on-line (using meteorology from WRF simulation) for the domain.

MEGAN uses inputs such as Leaf Area Index (LAI), meteorological parameters (solar radiation, temperature, and moisture) to calculate hourly biogenic emissions.

Overall, the model underestimated isoprene concentration at Zion super-site especially in the second half of the campaign when isoprene emissions increased due to increase in green vegetation fraction in June compared to May (Figure 4-19). We ran simulations with doubled biogenic isoprene emissions (2Iso) for 31 May to June 20 2017. The 2Iso simulation better captured the magnitude of isoprene concentration at Zion super-site in the second half of the campaign but with negative bias (Figure 4-19).

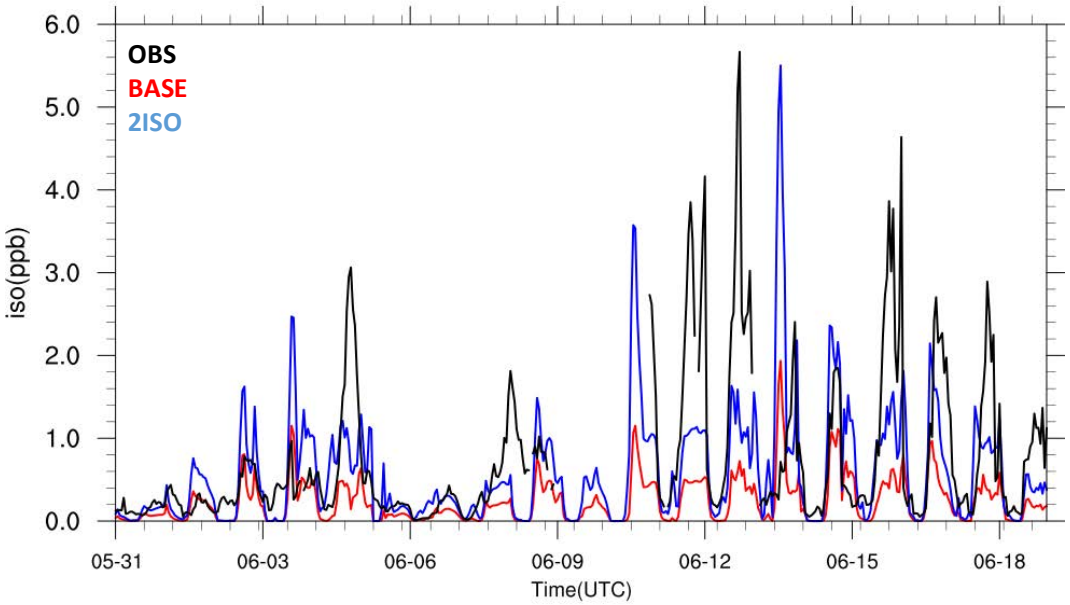

Figure 4-19 Timeseries of measured and modeled (base and 2ISO) isoprene concentration at Zion super-site

Averaged daytime isoprene emission map shows that most of the biogenic activities and emissions occur south and to smaller magnitude northwest of the domain (Figure 4-20). Although increase in biogenic emissions resulted in increase in isoprene concentrations, but it largely impacted south and northwest parts of the domain. Low concentrations of isoprene and weak sensitivity of isoprene concentration to doubled isoprene emissions on 2 June can explain

the low sensitivity of ozone concentrations to changes in isoprene emissions observed in Figure 4-18. On average, with increase of 5ppb in isoprene concentrations in the south of the domain 2Iso simulation ozone only increased by up to 1ppb. Although isoprene concentration over the lake only increased marginally in 2Iso simulation (less than 1ppb) but this also resulted in 1ppb increase in ozone concentrations over the lake which indicates the high sensitivity of ozone production to changes in VOC concentrations over the lake or the domination of a VOC-limited regime.

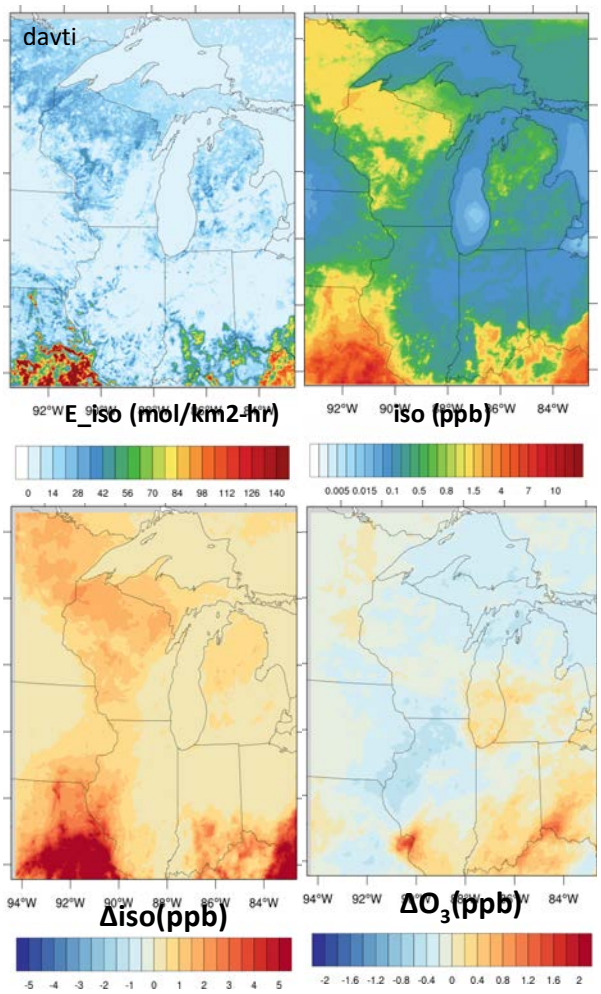

Figure 4-20 Top plot: Top rows: mean isoprene emissions during the daytime (10am-6pm LT)(left plot) and mean isoprene concentration in base simulation (right plot). Bottom plots: Mean differences in isoprene (left plot) and ozone (right plot) concentration in base and 2iso simulation. all averages are from 31 May to 20 June 2017. $\Delta x = X_{2iso} - X_{base}$

4.5.3 Back-trajectories

To better understand the transport patterns in the domain on the 2 June ozone event we ran back-trajectories with the base simulation meteorology and FLEXible PARTicle (FLEXPART). FLEXPART is a Lagrangian Particle Dispersion Model that uses WRF (or other models) wind field predictions to determine the trajectory of air parcels in a forward or a backward mode. 1000 particles were released at 100m altitudes from different release points along the Lake. We compared the trajectory of air parcels released on 2 June (7pm LT) with 3 June (7pm LT) to investigate the impact of lake breeze on the air parcel trajectories. In the back-trajectory simulations the air parcels were followed for 24 hours backward from the release time.

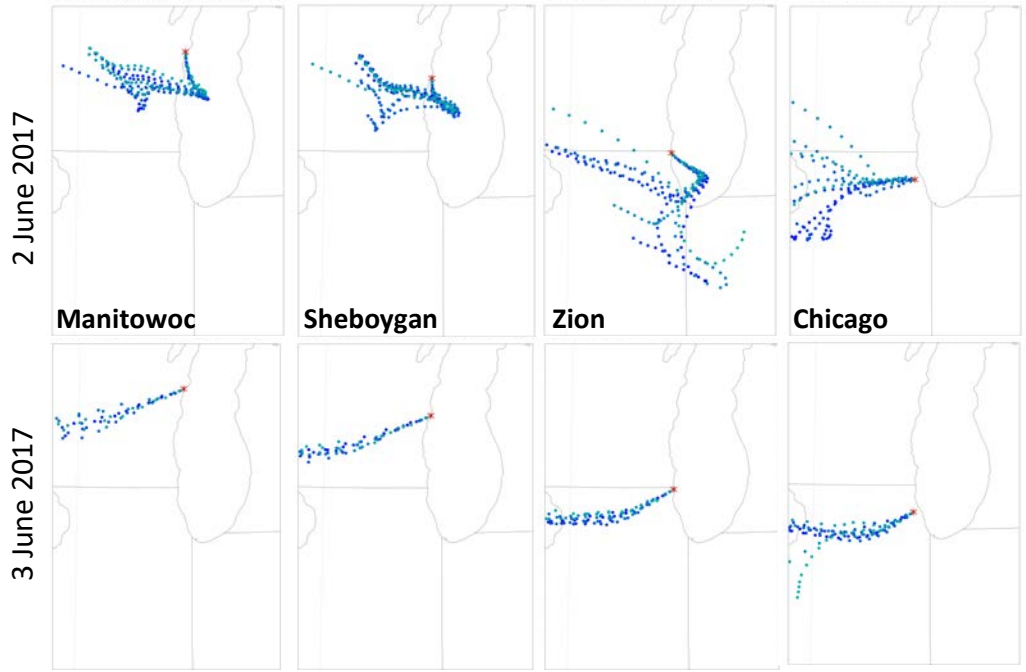

Figure 4-21 24 hours back-trajectory of tracers released from different points along the shore on 2 and 3 June 2017

The strong lake breeze on 2 June recirculated the air parcels over the lake (Figure 4-21). Specifically, air parcels that arrived at Zion had passed over Chicago (large emission source), stayed over the lake for ~7 hours, and then arrived at Zion. The air parcels arrived at Manitowoc

and Sheboygan also followed a similar pattern of recirculation but did not pass over Chicago. Air parcels that arrived at Chicago release point (further inland) were not influenced by the lake breeze. This explains the low sensitivity of ozone at EPA Chicago site to changes in the HC or NOx emissions (Figure 4-18). It can be concluded that ozone production over the lake is more sensitive to changes in HC emissions compared to over the land. On 3 June (non-lake breeze day) westerly winds were dominant in the region and transport the air parcels from the west to the release point.

4.5.4 Ozone tendencies

We used the online forward trajectory tool available in WRF-Chem v3.9 (and later) which keeps track of different variables (set in a namelist) in an air parcel released at a certain location and time in the model timestep (in our case 30 second). We combined this tool with diagnostics option in WRF-Chem that provides extra parameters such as tendencies (chemical production, horizontal and vertical advection, and vertical mixing) of different species in the model. We extracted the ozone tendencies along the air parcel trajectories released from different release points at different altitudes and time. We focused on trajectories over the lake because the largest sensitivity of ozone to HC emissions occurred over the lake (Figure 4-23). Figure 4-22 shows a forward trajectory of an air parcel released from Chicago at 10am LT on 2 June and the ozone concentrations and tendencies along the air parcel trajectory. This particular air parcel was followed for 15 hours (10am to 1am LT), reached the lake after one hour from the release time and traveled from southwest of the lake to north for 14 hours. The parcel altitude remained below 700m along the trajectory with slightly higher altitude in the first 8 hours (10am to 6pm LT). The model predicted stronger vertical mixing (blue triangle bottom row) and higher PBL height (solid line in the middle row plot) over the land compared to over the water, which is due to lower temperature and weaker vertical mixing over the water. As the air parcel reached over

the lake the vertical mixing became small. In the base simulation the maximum ozone chemical production (red circle) reached to 2ppb/hr during the day and reduced to zero during the nighttime. In the HC increased (0.72NOx_5HC) case ozone chemical production reached to ~7ppb/hr in the afternoon (3pm LT). Higher ozone production rate in the 0.72NOx_5HC simulation resulted in ~ 15ppb higher ozone concentrations.

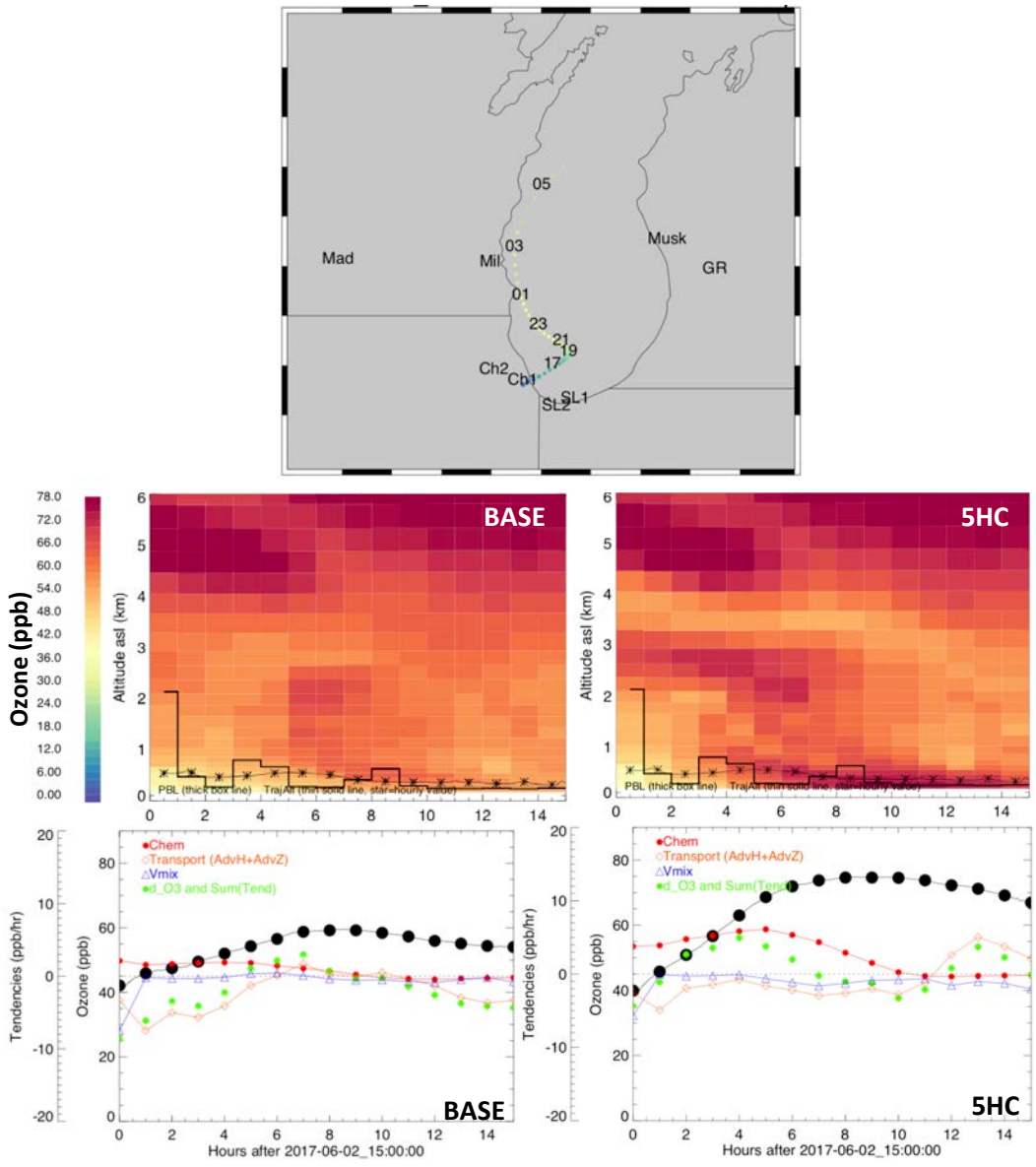

Figure 4-22 Top plot: trajectory of an air parcel released at 15 UTC (10am LT) on 2 June 2017 from Chicago at altitude of 0.54km above the ground. Middle row: vertical cross-section of ozone concentration along the air parcel trajectory in the base (left plot) and 0.72NOx_5HC (right plot)

simulations. Solid line shows the PBL height in the model along the air parcel trajectory and asterisk show the air parcel elevation. Bottom row: ozone and ozone tendency along the air parcel trajectory in the base (left plot) and 0.72NOx_5HC (right plot) simulations. Black circles show ozone concentration, red circles show ozone tendency due to chemical production/loss, orange diamond show ozone loss due to vertical or horizontal advection, and blue triangle show ozone loss due to vertical mixing. Green circles are the sum of all ozone tendencies

4.6 Overall Performance of Increased HC Simulations

Simulation with 5 times increase in HC (0.72NOx_5HC) successfully captured the maximum ozone concentration on 2 June at the EPA Zion site but not at Chicago site. To better understand the discrepancies between ozone sensitivity to HC emissions at different locations and times, we ran 0.72NOx_5HC simulation for a longer period from 30 May to 21 June 2017. Table 4-5 includes a summary of hourly and 8-hr peak statistics for all the emission sensitivity simulations at EPA Zion and EPA Chicago sites. Overall, the base simulation performance at the Chicago site is acceptable with hourly bias of -0.5ppb and 8-hr peak bias of 1.2ppb. The performance is poorer at Zion site with hourly bias of -3.4ppb and 8-hr peak bias of -5.3ppb. The 0.72NOx_5HC simulation increased the model errors at the Chicago site with hourly bias of 3.9ppb and 8-hr peak bias of 6.6ppb but improved the model performance at Zion site with hourly bias of 0.7ppb and 8-hour peak of -5.3ppb.

Table 4-5 Summary of model performance in capturing ozone at EPA Chicago and Zion sites

Chicago	Hourly O3 (ppb)						8hr peak O3 (ppb)				
	n	R2	RMSE	mod mean	obs mean	bias	n	R2	mod mean	obs mean	bias
0.72NOx (base)	466	0.56	11.3	33.8	34.3	-0.5	18	0.7	49.2	48	1.2
0.72NOx_5HC	466	0.57	12.2	38.2	34.3	3.9	18	0.72	54.6	48	6.6

Zion	Hourly O3 (ppb)						8hr peak O3 (ppb)				
	n	R2	RMSE	mod mean	obs mean	bias	n	R2	mod mean	obs mean	bias

0.72NOx (base)	467	0.35	14.2	38.1	41.5	-3.4	19	0.38	51.3	56.6	-5.3
0.72NOx_5HC	467	0.44	13.3	42.2	41.5	0.7	19	0.54	58.2	56.6	1.6

Figure 4-23 compares the modeled ozone concentration in base and 0.72NOx_5HC simulations with measurements at EPA Zion and Chicago site. It should be noted that at the Zion site 5 times increase in HC emissions only increased the peak ozone concentrations on some of the days and did not impact the nighttime minimum ozone concentrations.

At the Chicago site, 0.72NOx_5HC predicted higher ozone concentrations and closer to measurements but predicted lower nighttime ozone concentrations compared to base simulation and measurements. On average 0.72NOx_5HC predicted up to 6ppb higher surface ozone concentrations mostly over the lake.

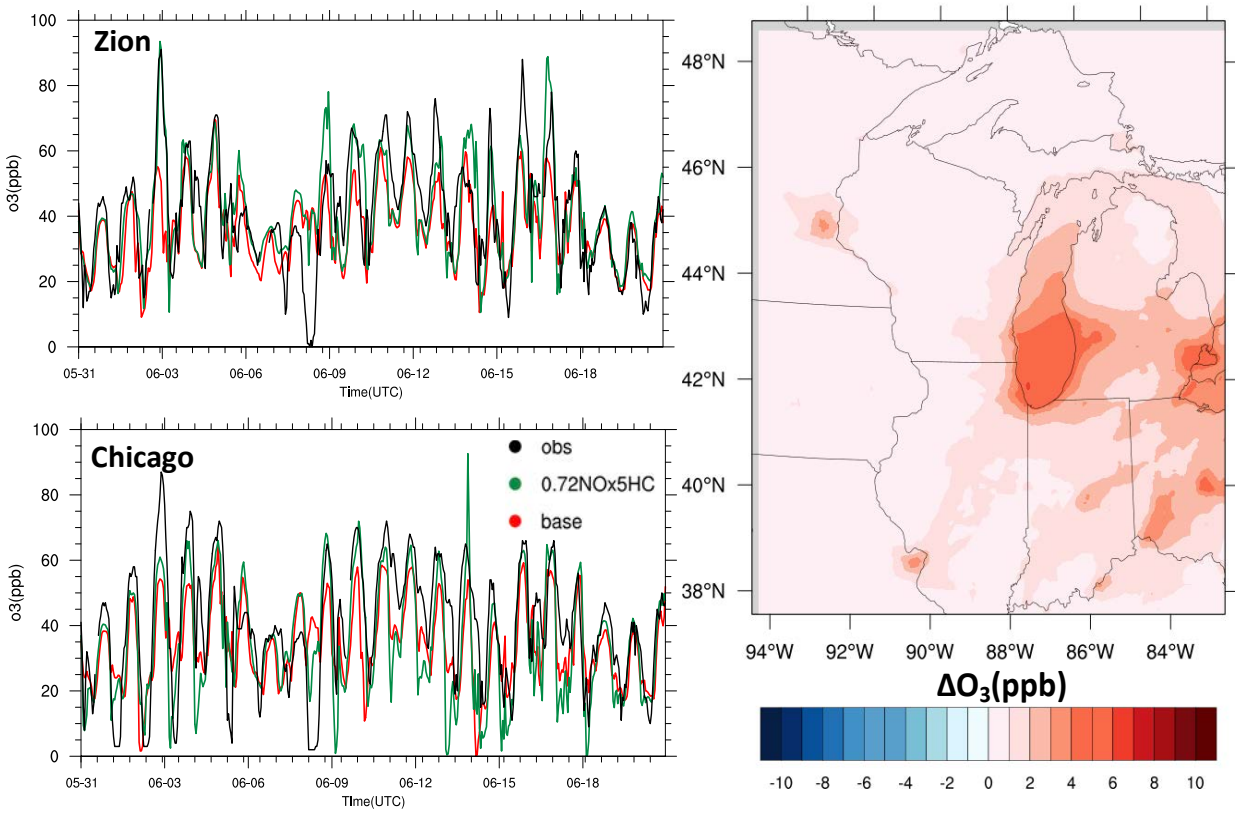

Figure 4-23 Left column: Timeseries of modeled ozone in base and 0.72NOx_5HC and measurements at EPA Zion and Chicago sites. Right panel: average differences of surface ozone between 0.72NOx_5HC and base from May 31 to Jun 21. $\Delta O3 = O3_{0.72NOx\_5HC} - O3_{base}$

Formaldehyde (HCHO) has both primary and secondary sources and plays an important role in total VOC reactivity and ozone formation. Primary sources of formaldehyde are the transport sector, combustion, biogenic sources, and biomass burning (Luecken et al., 2012). Secondary formaldehyde is the product of VOC degradation by OH, which is the dominant source of atmospheric formaldehyde. Formaldehyde concentration measurements at Sheboygan super-site indicates a negative bias in the base simulation (Figure 4-24). In the increased HC case (0.72NOx_5HC) primary anthropogenic emission of formaldehyde was not increased. However, model performance in capturing formaldehyde concentration was improved in 0.72NOx_5HC case. The increase in formaldehyde concentration is due to increase in VOC (formaldehyde precursor) concentrations that increases the chemical production of formaldehyde.

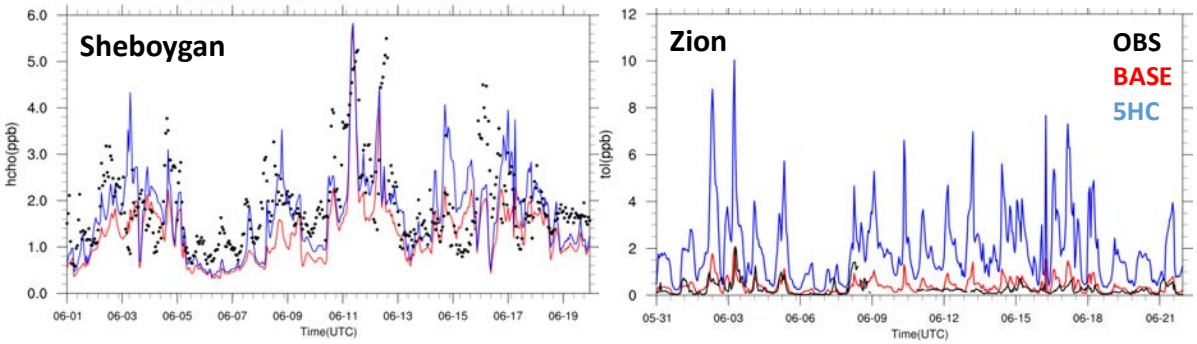

Figure 4-24 Timeseries of formaldehyde (HCHO) measurements and modeled (base and 0.72NOx_5HC) at Sheboygan super-site (Left). Timeseries of TOL (toluene+benzene) measurements and modeled (base and 0.72NOx_5HC) at Zion super-site (Left)

Toluene and benzene are lumped together in the RACM chemical mechanism under "TOL" (Stockwell et al., 1997). The transport sector is a strong source of toluene and benzene. We compared simulated TOL with the sum of toluene and benzene concentrations measured at Zion super-site. TOL concentration in the base simulation agreed well with the measurements and the 0.72NOx_5HC simulation over estimated TOL concentration.

4.7 Indicator of Surface Ozone-NOx-VOC Sensitivity

The sensitivity of zone formation to changes in NOx and VOC emission is nonlinear. It is important to understand how changes in the ozone precursors can impact the ozone formation as this information is needed to design effective mitigation policies. In the NOx-limited regions reductions in NOx emissions result in reduction in ozone formation. In the VOC or HC-limited regimes reduction in VOC reduces ozone formation. In the emission sensitivity analysis, we detected high sensitivity of ozone formation to HC emissions over the lake. Different indicators such as HCHO/NO_2 and H_2O_2/HNO_3 have been developed and used to reflect the nonlinear sensitivity of ozone to NOx and HC (Sillman, 1995; Tonnesen and Dennis, 2000). Column HCHO/NO_2 or column FNR is often used to reflect the reactivity of VOC and NOx with OH.

The threshold of column FNR less than 1 has been used to represent a HC-limited regime and column FNR greater than 2 represents NOx-limited regime (Duncan et al., 2010).

We calculated the mean hourly FNR for base simulation and hourly FNR for base and 0.72NOx_5HC simulations (Figure 4-25). On average, column FNR over south of the lake varies from 1 to 2 which indicates a transition region. Over Chicago are column FNR is less than 0.6 indicating a HC-limited region. On 2 June 2017, air over the lake was influenced by Chicago plume thus model predicted column FNR less than 0.6 and a HC-limited regime over the lake. This agrees with sensitivity of ozone formation to changes in HC emissions in different emission scenarios. In 0.72NOx_5HC simulation, column FNR over the lake reached values between 1 and 2.5 indicating mostly a transition regime over the lake. It should be noted that base simulation underestimated formaldehyde concentration at Sheboygan site and overall over estimated NO_2 concentration. It can be concluded that real FNR values are larger compared to base simulation. Column formaldehyde and NO2 observation from remote sensing instruments such as Ozone Monitoring Instrument (OMI) or GeoTASO can be used to compare measured and modeled FNR values. Jin et al. (2017) used OMI measurements to show that NOx-limited regime dominates over the northeast US. Observed FNR (OMI) varies interannually over Chicago and shifts from NOx-limited to HC-limited regimes but is dominantly NOx-limited.

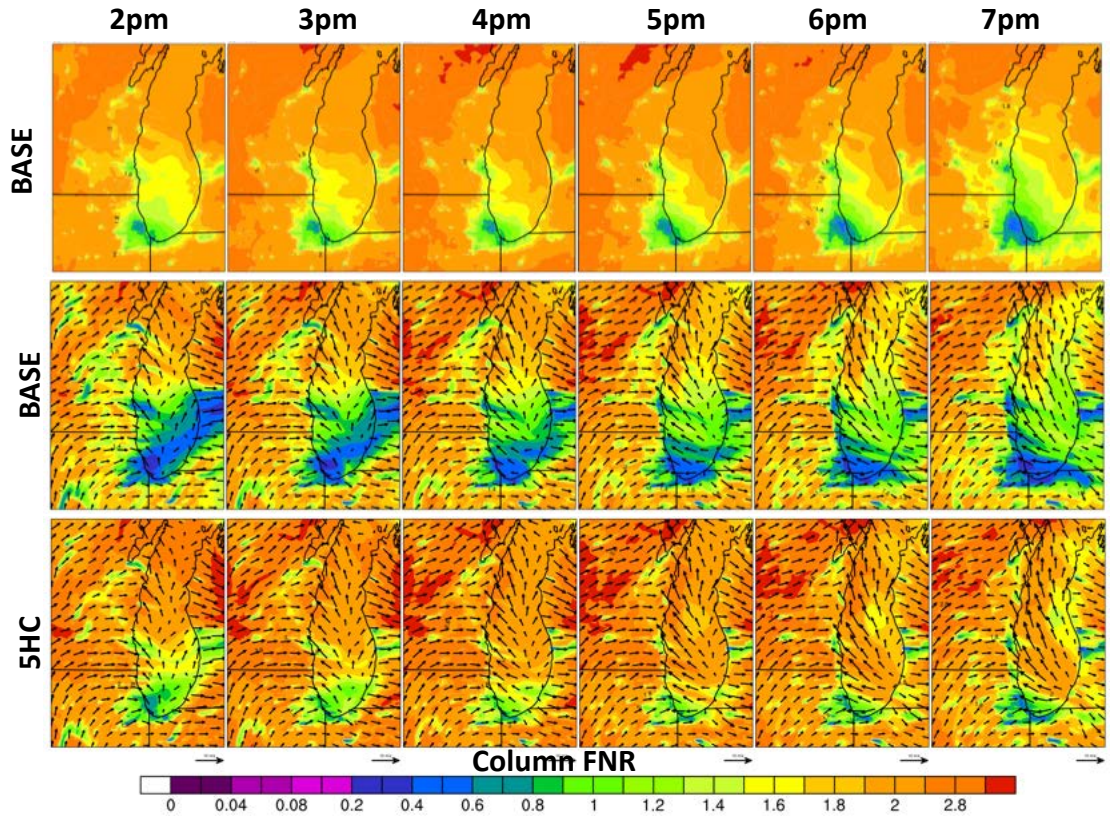

Figure 4-25 Top row: Mean hourly column FNR in base simulation averaged over 31 May to 20 June 2017. Middle row: hourly column FNR in base simulation on 2 June 2017. Bottom plot: hourly column FNR in 0.72NOx_5HC simulation on 2 June 2017

Measurements of H_2O_2 and HNO_3 are available at Zion super-site. Similar to FNR, H_2O_2 to HNO_3 ratio have been used as indicator to identify NOx or HC-limited regimes. H_2O_2/HNO_3 less than 0.4 indicates a HC-limited regime. Comparisons of measured with base and 0.72NOx_5HC values (Figure 4-26) show that model underestimates H_2O_2 especially in the second half of the campaign when measured H_2O_2 increased. Model better captured HNO_3 concentrations and diurnal variations. The increase in HC emissions did not impact H_2O_2 or HNO_3 in the model. Measured H_2O_2 to HNO_3 ratios at Zion super-site are mostly greater than 0.4 which indicates a NOx-limited regime. Because of the large underestimation in H_2O_2 by the model, predicted H_2O_2 to HNO_3 ratios are mostly very small which puts the model in HC-limited regime.

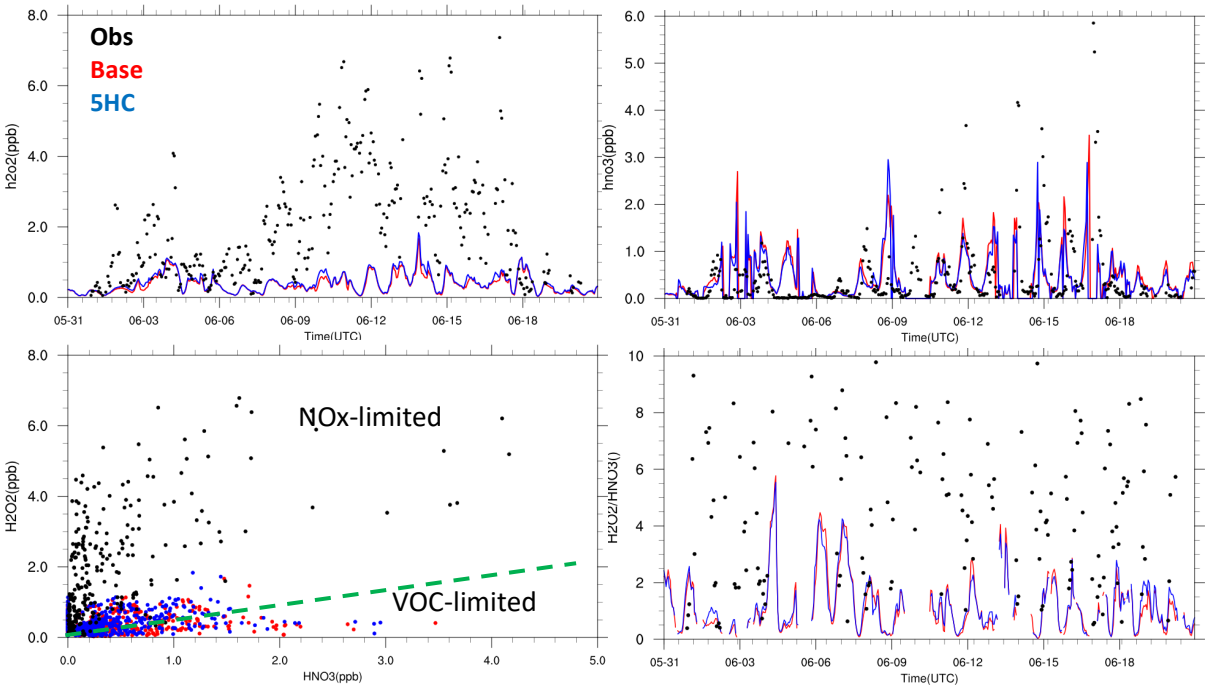

Figure 4-26 Top row: timeseries of H_2O_2 and HNO_3 concentrations for measured, base model, and 0.72NOx_5HC model. Bottom row: scatter plot of measured and modeled H_2O_2 vs. HNO_3. The green line shows 0.4 ratio. Timeseries of H_2O_2/HNO_3 for measured and modeled values

4.8 Conclusions

WRF-Chem model (with NEI-2011v2 emissions) and measurements from the Lake Michigan Ozone Study (LMOS) 2017 field experiment were used to investigate the ozone formation over Lake Michigan and transport of ozone and ozone precursors by the land and lake breeze. WRF-Chem simulation with HRRR meteorological initial and boundary condition and Noah land surface model successfully represented the temperature and relative humidity in the domain. Updating SST fields in the model with GDAS 1/12th measurements increased the air temperature over the east of the lake by up to 4ºC. This increased only impacted ozone concentration by up to 2ppb. WRF-Chem simulation captures the diurnal cycles and trends of ozone concentration but consistently underestimated the maximum ozone concentrations. Overall, NOx concentration was overestimated in the simulation especially in the second part of the campaign. Isoprene

concentration increased in June due to increase in green vegetation which was captured in the model but at a smaller magnitude.

On 2 June 2017 a strong lake breeze occurred and resulted in high ozone concentrations along the west shoreline of the lake. Model predicted the lake breeze but failed to capture high concentrations of ozone at sites along the shore. We conducted simulations for the 2 June high ozone event with perturbed NOx and HC emissions to investigate the sensitivity of ozone formation to changes in emissions. 50% reduction in NOx resulted in ~20ppb increase in ozone concentrations at the EPA Zion site and ~10ppb reduction in ozone concentration at the Chicago site. Ozone formation showed sensitivity to increase in HC emissions. 5 times increase in HC emissions (0.72NOx_5HC) resulted in ~50ppb increase in ozone concentration at EPA Zion site and ~5ppb increase at Chicago site. Modeled ozone did not show strong sensitivity to doubled biogenic isoprene emissions on 2 June event.

FLEXPART backtrajectory tests indicate that on 2 June 2017 in the morning land breeze transported the ozone precursors from Chicago area over the lake. Ozone was formed over the lake and then transported to the north and then reach the shoreline by strong southeasterly winds (lake breeze).

We ran the simulation with 5 times increased in HC for a longer period. On overage, ozone formation over the lake was very sensitive to the changes in HC emissions. 5 times increase in HC emissions resulted in up to 6ppb increase in surface ozone concentration over the lake. Maximum ozone concentrations were better captured in the 0.72NOx_5HC simulation on most of the days. Low column FNR in the model over the lake also confirm a HC-limited regime over the lake in the model world. Column FNR can be retrieved from different remote sensing instruments and compared against the model values.

Integrated Reaction Rate is a new tool in the latest version of WRF-Chem (4.0) which will be used to better understand the ozone formation process over the lake. This tool creates hourly output files with reaction rates of all reactions in a 3D field in the domain. By using this tool we can calculate the OH reactivity to different VOC and compare the values across different emission sensitivity simulations.

To further investigate the uncertainties in the emissions, we will implement the variational inverse modeling technique discussed in Chapter 3 to constrain NOx emissions. NOx measurements by GeoTASO and TROPOMI instrument along with airborne (by scientific aviation aircraft) and ground-based measurements will be incorporated into the inversion algorithm.

5 GENERAL CONCLUSIONS

5.1 Summary of Results

In chapter 2, We used WRF-Chem and National Emission Inventory (NEI-2011v2) to understand the sensitivity of pollutant transport at a high horizontal resolution to different model configurations with the focus on oil and NG emissions. Comparisons between measured and model ethane (a tracer of oil and NG) showed a large underestimation of ethane in regions close to oil and NG activities with biases up to -14.9 ppb (NMB up to -80.5%). This underestimation was observed in all sensitivity simulations which suggests that NEI-2011v2 under-predicts oil and NG emissions. We used Normalized Mean Bias (NMB) variability between different simulations as a proxy for variability in the model performance caused by model configurations. The largest sensitivity occurred in the initialization test (comparing daily re-initialization with free-run simulation) with ethane NMB variability up to 57.3%, followed by the horizontal resolution test (comparing horizontal resolution of 12 km × 12 km with 4 km × 4 km) and the PBL parametrization test (comparing local with non-local PBL schemes) with ethane NMB variability up to 33.3% and 32.4%, respectively.

We compared measured ethane, CO, lumped alkanes (HC3), lumped toluene and benzene (TOL), and xylene to corresponding modeled values and assessed the changes in the model performance when doubling oil and NG emissions. Doubling oil and NG emissions in the emission inventory resulted in an improvement during the morning and an overestimation of ethane during the afternoon which suggests possible incorrect representation of the diurnal variation of ethane emission rates in the NEI-2011v2. It was concluded that CO is predominantly emitted from sources other than oil and NG due its low sensitivity in the changes to emissions from this sector in the emission inventory. Comparisons with CO measurements indicated that the model tends to

overestimate CO over the Denver region and underestimates CO over the oil and NG region. Model underestimated HC3, TOL, and xylene over oil and NG facilities and the ethane to VOC ratios in the measurement did not match the model based on NEI-2011v2 inventory.

Chapter 3 focuses on developing and implementing a variational inverse modeling method to constrain ethane emissions from oil and NG sector in the Northern Front Range (NFR) Colorado. Hourly tracers were added into the WRF-Chem simulation and were linked to ethane emissions from oil and NG sources in NEI-2011v2. The result indicated that the measured ethane in the NFR region is predominantly emitted from sources in Denver-Julesburg (DJ) basin. Hourly ethane emission rates in the Wattenberg field were low by up to a factor of 6 in the NEI-2011v2 and the total ethane emissions from oil and NG sector derived from the inverse modeling solution is between 11% to 15% higher than the NEI-2011v2.

Chapter 4 describes the WRF-Chem model and NEI-2011v2 emission inventory performance in capturing transport and ozone and ozone precursors concentrations in Lake Michigan region. WRF-Chem simulation with HRRR meteorological initial and boundary condition and Noah land surface model successfully represented the temperature and relative humidity in the domain. The diurnal cycles and trends of ozone concentration were captured in the model but with negative biases at the maximum ozone concentrations. NOx was overestimated in the simulations. Emission sensitivity analysis showed that 5 times increase in Hydrocarbon (HC) emissions resulted in an increase in maximum ozone concentrations and improved the overall model performance especially on days when lake breeze occurred. Low column formaldehyde to NOx ratio (FNR) also confirmed an HC-limited regime over the lake I the model.

5.2 Future Directions

The inverse modeling method performed in chapter 3 showed promising capabilities in constraining ethane emissions. Conducting the inversion method using a different model configuration (e.g., PBL scheme) can provide a range of scaling factor and increase the confidence level and robustness in the final emission estimates.

The ethane to methane or other VOCs (such as toluene, benzene, and alkanes) ratios can be used to constrain the emission rates of these species. These calculations can help reduce the uncertainties in the emission inventories and better assess the impact of oil and NG sector on regional and global air quality and climate. One of the main challenges is the attribution of methane (or other VOCs) to the oil and NG sector. Methane has other major anthropogenic sources besides oil and NG sector such as agriculture sector (i.e., feedlots) which includes high uncertainties in the emission rates (Kille et al., 2017).

Estimating the ethane emission rates in other oil and NG fields in the US using measurements from the NOAA Shale Oil and Natural Gas Nexus (SONGNEX 2015) can provide a broader overview on the total ethane (or other species) emission rates from oil and NG sector in the US.

Although WRF-Chem simulation captured the transport and chemistry over the Lake Michigan region, more investigation is required to better understand the uncertainties in the emission inventories. Using some of the newly developed tools in WRF-Chem (4.0) such as Integrated Reaction Rate can be used to better understand the ozone formation process by analyzing the reaction rates in the simulations at each simulation hour. By using this tool, we can calculate the OH reactivity to different VOC and compare the values across different emission sensitivity simulations.

A sectoral analysis regarding the impact of uncertainties in the emission rates of different sectors and their impact of predicting ozone over Lake Michigan can be beneficial for the policymakers. The inverse modeling technique used in chapter 3 can be implemented to constrain NOx emissions from the west shore of Lake Michigan. Hourly tracers linked to NOx emissions can be assigned to different regions in the domain or different sector (requires a sector-based gridded emission inventory). Remote sensing measurements by GeoTASO equipment and TROPOMI along with the available airborne and ground-based NO_2 and NOx measurements can provide us with an acceptable coverage of the domain. By incorporating these measurements into the inverse modeling algorithm optimal scaling factor for the hourly tracers can be calculated.

5.3 Final Remarks

The main goal of this dissertation was to understand, quantify, and improve the uncertainties in the WRF-Chem model and emission inventories by using various suites of measurements. The abundance of atmospheric measurement from ground-sites, field experiments, and satellites, provides an opportunity to study and address the shortcomings of atmospheric chemistry and transport models in much more details using systematic data-driven methods. This work highlights some of the capabilities of the WRF-Chem model and discusses the capabilities of data-driven methods such as inverse modeling in reducing the uncertainties in the emission inventories.

REFERENCES

Abdi-Oskouei, M., Pfiester, G., Flocke, F., Sobhani, N., Saide, P. and Carmichael, G.: Impacts of physical parametrization on prediction of ethane concentrations for oil and gas emissions, Atmos. Chem. Phys. Discuss., 2018.

Ahmadov, R., McKeen, S., Trainer, M., Banta, R., Brewer, A., Brown, S., Edwards, P. M., De Gouw, J. A., Frost, G. J., Gilman, J., Helmig, D., Johnson, B., Karion, A., Koss, A., Langford, A., Lerner, B., Olson, J., Oltmans, S., Peischl, J., Pétron, G., Pichugina, Y., Roberts, J. M., Ryerson, T., Schnell, R., Senff, C., Sweeney, C., Thompson, C., Veres, P. R., Warneke, C., Wild, R., Williams, E. J., Yuan, B. and Zamora, R.: Supplement of Understanding high wintertime ozone pollution events in an oil- and natural gas-producing region of the western US, Atmos. Chem. Phys., 15(1), 411–429, doi:10.5194/acp-15-411-2015, 2015a.

Ahmadov, R., McKeen, S., Trainer, M., Banta, R., Brewer, A., Brown, S., Edwards, P. M., De Gouw, J. A., Frost, G. J., Gilman, J., Helmig, D., Johnson, B., Karion, A., Koss, A., Langford, A., Lerner, B., Olson, J., Oltmans, S., Peischl, J., Pétron, G., Pichugina, Y., Roberts, J. M., Ryerson, T., Schnell, R., Senff, C., Sweeney, C., Thompson, C., Veres, P. R., Warneke, C., Wild, R., Williams, E. J., Yuan, B. and Zamora, R.: Understanding high wintertime ozone pollution events in an oil- and natural gas-producing region of the western US, Atmos. Chem. Phys. Discuss., 15(1), 411–429, doi:10.5194/acp-15-411-2015, 2015b.

Ahmadov, R., McKeen, S., Trainer, M., Banta, R., Brewer, A., Brown, S., Edwards, P. M., De Gouw, J. A., Frost, G. J., Gilman, J., Helmig, D., Johnson, B., Karion, A., Koss, A., Langford, A., Lerner, B., Olson, J., Oltmans, S., Peischl, J., Pétron, G., Pichugina, Y., Roberts, J. M., Ryerson, T., Schnell, R., Senff, C., Sweeney, C., Thompson, C., Veres, P. R., Warneke, C., Wild, R., Williams, E. J., Yuan, B. and Zamora, R.: Understanding high wintertime ozone pollution events in an oil- and natural gas-producing region of the western US, Atmos. Chem. Phys., 15(1), 411–429, doi:10.5194/acp-15-411-2015, 2015c.

Allen, D.: Attributing Atmospheric Methane to Anthropogenic Emission Sources, Acc. Chem. Res., 49(7), 1344–1350, doi:10.1021/acs.accounts.6b00081, 2016a.

Allen, D. T.: Emissions from oil and gas operations in the United States and their air quality implications, J. Air Waste Manage. Assoc., 66(6), 549–575, doi:10.1080/10962247.2016.1171263, 2016b.

Allen, D. T., Torres, V. M., Thomas, J., Sullivan, D. W., Harrison, M., Hendler, A., Herndon, S. C., Kolb, C. E., Fraser, M. P., Hill, A. D., Lamb, B. K., Miskimins, J., Sawyer, R. F. and Seinfeld, J. H.: Measurements of methane emissions at natural gas production sites in the United States, Proc. Natl. Acad. Sci., 110(44), 17768–17773, doi:10.1073/pnas.1304880110, 2013.

Alvarez, R. A., Pacala, S. W., Winebrake, J. J., Chameides, W. L. and Hamburg, S. P.: Greater focus needed on methane leakage from natural gas infrastructure., Proc. Natl. Acad. Sci. U. S. A., 109(17), 6435–40, doi:10.1073/pnas.1202407109, 2012.

Anenberg, S. C., Horowitz, L. W., Tong, D. Q. and West, J. J.: An estimate of the global burden of anthropogenic ozone and fine particulate matter on premature human mortality using atmospheric modeling, Environ. Health Perspect., 118(9), 1189–1195, doi:10.1289/ehp.0901220, 2010.

Angevine, W. M., Eddington, L., Durkee, K., Fairall, C., Bianco, L. and Brioude, J.: Meteorological model evaluation for CalNex 2010, Mon. Weather Rev., 3885–3906, doi:10.1175/MWR-D-12-00042.1, 2012.

Arakawa, A., Jung, J. H. and Wu, C. M.: Toward unification of the multiscale modeling of the atmosphere, Atmos. Chem. Phys., 11(8), 3731–3742, doi:10.5194/acp-11-3731-2011, 2011.

Barkley, Z. R., Lauvaux, T., Davis, K. J., Deng, A., Miles, N. L., Richardson, S. J., Cao, Y., Sweeney, C., Karion, A., Smith, M., Kort, E. A., Schwietzke, S., Murphy, T., Cervone, G., Martins, D. and Maasakkers, J. D.: Quantifying methane emissions from natural gas production in north-eastern Pennsylvania, Atmos. Chem. Phys, 17, 13941–13966, doi:10.5194/acp-17-13941-2017, 2017.

Benjamin, S. G., Weygandt, S. S., Brown, J. M., Hu, M., Alexander, C. R., Smirnova, T. G., Olson, J. B., James, E. P., Dowell, D. C., Grell, G. A., Lin, H., Peckham, S. E., Smith, T. L., Moninger, W. R., Kenyon, J. S. and Manikin, G. S.: A North American Hourly Assimilation and Model Forecast Cycle: The Rapid Refresh, Mon. Weather Rev., 144(4), 1669–1694, doi:10.1175/MWR-D-15-0242.1, 2016.

Bergamaschi, P., Houweling, S., Segers, A., Krol, M., Frankenberg, C., Scheepmaker, R. A., Dlugokencky, E., Wofsy, S. C., Kort, E. A., Sweeney, C., Schuck, T., Brenninkmeijer, C., Chen, H., Beck, V. and Gerbig, C.: Atmospheric CH<inf>4</inf> in the first decade of the 21st century: Inverse modeling analysis using SCIAMACHY satellite retrievals and NOAA surface measurements, J. Geophys. Res. Atmos., 118(13), 7350–7369, doi:10.1002/jgrd.50480, 2013.

Blaylock, B. K., Horel, J. D. and Liston, S. T.: Cloud archiving and data mining of High-Resolution Rapid Refresh forecast model output, Comput. Geosci., 109(August), 43–50, doi:10.1016/j.cageo.2017.08.005, 2017.

Brandt, A. R., Heath, G. A., Kort, E. A., O'Sullivan, F., Petron, G., Jordaan, S. M., Tans, P., Wilcox, J., Gopstein, a M., Arent, D., Wofsy, S., Brown, N. J., Bradley, R., Stucky, G. D., Eardley, D. and Harriss, R.: Methane Leaks from North American Natural Gas Systems, Science (80-.)., 343(6172), 733–735, doi:10.1126/science.1247045, 2014.

Caulton, D. R.: Toward a better understanding and quantification of methane emissions from shale gas development-Supplement material, Proc. Natl. Acad. Sci. U. S. A., 128, 1–32, doi:10.1002/0471250953.bi1007s36, 2011.

Cheadle, L. C., Oltmans, S. J., Pétron, G., Schnell, R. C., Mattson, E. J., Herndon, S. C., Thompson, A. M., Blake, D. R. and Mcclure-begley, A.: Surface ozone in the Northern Front Range and the influence of oil and gas development on ozone production during FRAPPE / DISCOVER-AQ, Elem. Sci. Anthr., 6, doi:http://doi.org/10.1525/elementa.254, 2017.

Chen, F. and Dudhia, J.: Coupling an Advanced Land Surface–Hydrology Model with the Penn State–NCAR MM5 Modeling System. Part II: Preliminary Model Validation, Mon. Weather Rev., 129(4), 587–604, doi:10.1175/1520-0493(2001)129<0587:CAALSH>2.0.CO;2, 2001.

Chen, F., Liu, C., Dudhia, J. and Chen, M.: A sensitivity study of high-resolution regional climate simulations to three land surface models over the western United States, J. Geophys. Res., 7271–7291, doi:10.1002/2014JD021827.Received, 2014.

Chou, M.-D. and Suarez, M. J.: Technical Report Series on Global Modeling and Data Assimilation A Thermal Infrared Radiation Parameterization for Atmospheric Studies Revised May 2003 i, Nasa Tech. Memo., 15(104606), 40, 1999.

Cleary, P. A., Fuhrman, N., Schulz, L., Schafer, J., Fillingham, J., Bootsma, H., McQueen, J., Tang, Y., Langel, T., McKeen, S., Williams, E. J. and Brown, S. S.: Ozone distributions over southern Lake Michigan: Comparisons between ferry-based observations, shoreline-based DOAS observations and model forecasts, Atmos. Chem. Phys., 15(9), 5109–5122, doi:10.5194/acp-15-5109-2015, 2015.

Colorado Oil and Gas Conservation Commission: COGIS - Production Data Inquiry, [online] Available from: http://cogcc.state.co.us/data.html#/cogis (Accessed 1 January 2017), 2017.

Compton, J. C., Delgado, R., Berkoff, T. A. and Hoff, R. M.: Determination of planetary boundary layer height on short spatial and temporal scales: A demonstration of the covariance wavelet transform in ground-based wind profiler and lidar measurements, J. Atmos. Ocean. Technol., 30(7), 1566–1575, doi:10.1175/JTECH-D-12-00116.1, 2013.

Conley, S., Franco, G., Faloona, I., Blake, D. R., Peischl, J. and Ryerson, T. B.: Methane emissions from the 2015 Aliso Canyon blowout in Los Angeles, CA, Science (80-.)., 2348(October 2015), 2–7, doi:10.1126/science.aaf2348, 2016.

Cuchiara, G. C., Li, X., Carvalho, J. and Rappenglück, B.: Intercomparison of planetary boundary layer parameterization and its impacts on surface ozone concentration in the WRF/Chem model for a case study in Houston/Texas, Atmos. Environ., 96, 175–185, doi:dx.doi.org/10.1016/j.atmosenv.2014.07.013, 2014.

Cui, Y. Y., Brioude, J., Frost, G. J., Peischl, J., Ryerson, T., Trainer, M., Wofsy, S. C., Santoni, G. W. and Kort, E. a.: Top-Down Estimate of Methane Emissions in California Using a Mesoscale Inverse Modeling Technique, 13th Annu. C. Conf., 1–6, doi:10.1002/2014JD023002, 2014.

Cui, Y. Y., Brioude, J., McKeen, S. A., Angevine, W. M., Kim, S. W., Frost, G. J., Ahmadov, R., Peischl, J., Bousserez, N., Liu, Z., Ryerson, T. B., Wofsy, S. C., Santoni, G. W., Kort, E. A., Fischer, M. L. and Trainer, M.: Top-down estimate of methane emissions in California using a mesoscale inverse modeling technique: The San Joaquin Valley, J. Geophys. Res. Atmos., 122, 3686–3699, doi:10.1002/2014JD023002, 2017.

Van Dingenen, R., Dentener, F. J., Raes, F., Krol, M. C., Emberson, L. and Cofala, J.: The global impact of ozone on agricultural crop yields under current and future air quality legislation, Atmos. Environ., 43(3), 604–618, doi:10.1016/j.atmosenv.2008.10.033, 2009.

Dingle, J. H., Vu, K., Bahreini, R., Apel, E. C., Campos, T. L., Flocke, F., Fried, A., Herndon, S., Hills, A. J., Hornbrook, R. S., Huey, G., Kaser, L., Montzka, D. D., Nowak, J. B., Reeves, M., Richter, D., Roscioli, J. R., Shertz, S., Stell, M., Tanner, D., Tyndall, G., Walega, J., Weibring, P. and Weinheimer, A.: Aerosol optical extinction during the front range air pollution and photochemistry Éxperiment (FRAPPÉ) 2014 summertime field campaign, Colorado, USA, Atmos. Chem. Phys., 16(17), 11207–11217, doi:10.5194/acp-16-11207-2016, 2016.

Duncan, B. N., Yoshida, Y., Olson, J. R., Sillman, S., Martin, R. V., Lamsal, L., Hu, Y., Pickering, K. E., Retscher, C., Allen, D. J. and Crawford, J. H.: Application of OMI observations to a space-based indicator of NOxand VOC controls on surface ozone formation, Atmos. Environ., 44(18), 2213–2223, doi:10.1016/j.atmosenv.2010.03.010, 2010.

Dye, T. S., Robert, P. T. and Korc, M. E.: Observations of Transport Processes for Ozone and Ozone Precursors during the 1991 Lake Michigan Ozone Study, J. Appl. Meteorol., 34(8), 1877–1889, 1995.

Emmons, L. K., Walters, S., Hess, P. G., Lamarque, J., Pfister, G. G., Fillmore, D. and Granier, C.: Model Development Description and evaluation of the Model for Ozone and Related chemical Tracers , version 4 (MOZART-4), , 43–67, 2010.

Energy information administration of US Department of Energy.: International energy outlook 2016-Natural gas, in International energy outlook 2016, pp. 37–60., 2016.

European Centre for Medium-Range Weather Forecasts (ECMWF): ERA-Interim Project, , doi:10.5065/D6CR5RD9, 2009.

Fast, J. D. and Heilman, W. E.: The Effect of Lake Temperatures and Emissions on Ozone Exposure in the Western Great Lakes Region, J. Appl. Meteorol., 42(9), 1197–1217, doi:10.1175/1520-0450(2003)042<1197:TEOLTA>2.0.CO;2, 2003.

Field, R. A., Soltis, J., McCarthy, M. C., Murphy, S. and Montague, D. C.: Influence of oil and gas field operations on spatial and temporal distributions of atmospheric non-methane hydrocarbons and their effect on ozone formation in winter, Atmos. Chem. Phys., 15(6), 3527–3542, doi:10.5194/acp-15-3527-2015, 2015.

Fiore, A. M., Naik, V., Spracklen, D. V., Steiner, A., Unger, N., Prather, M., Bergmann, D., Cameron-Smith, P. J., Cionni, I., Collins, W. J., Dalsøren, S., Eyring, V., Folberth, G. a., Ginoux, P., Horowitz, L. W., Josse, B., Lamarque, J.-F., MacKenzie, I. a., Nagashima, T., O'Connor, F. M., Righi, M., Rumbold, S. T., Shindell, D. T., Skeie, R. B., Sudo, K., Szopa, S., Takemura, T. and Zeng, G.: Global air quality and climate, Chem. Soc. Rev., 41(19), 6663–6683, doi:10.1039/c2cs35095e, 2012.

Foley, T., Betterton, E. A., Robert Jacko, P. E. and Hillery, J.: Lake Michigan air quality: The 1994-2003 LADCO Aircraft Project (LAP), Atmos. Environ., 45(18), 3192–3202, doi:10.1016/j.atmosenv.2011.02.033, 2011.

Franco, B., Mahieu, E., Emmons, L. K., Tzompa-Sosa, Z. A., Fischer, E. V, Sudo, K., Bovy, B., Conway, S., Griffin, D., Hannigan, J. W., Strong, K. and Walker, K. A.: Evaluating ethane and methane emissions associated with the development of oil and natural gas extraction in North America, Environ. Res. Lett., 11(4), 044010, doi:10.1088/1748-9326/11/4/044010, 2016.

Fried, A.: Fast Airborne Spectroscopic Measurements of Formaldehyde and Ethane During the 2014 Front Range Air Pollution and Photochemistry Éxperiment (FRAPPÉ), Color. Dep. Public Heal. Environ., 1–6, 2015.

Gilman, J. B., Lerner, B. M., Kuster, W. C. and De Gouw, J. A.: Source signature of volatile organic compounds from oil and natural gas operations in northeastern Colorado, Environ. Sci. Technol., 47(3), 1297–1305, doi:10.1021/es304119a, 2013.

Ginoux, P., Chin, M., Tegen, I., Prospero, J., Holben, B., Dubovik, O. and Lin, S.-J.: Sources and distributions of dust aerosols simulated with the GOCART model, J. Geophys. Res., 106(D17), 20255–20273, 2001.

Goldberg, D. L., Loughner, C. P., Tzortziou, M., Stehr, J. W., Pickering, K. E., Marufu, L. T. and Dickerson, R. R.: Higher surface ozone concentrations over the Chesapeake Bay than over the adjacent land: Observations and models from the DISCOVER-AQ and CBODAQ campaigns, Atmos. Environ., 84, 9–19, doi:10.1016/j.atmosenv.2013.11.008, 2014.

Grell, G. A. and Freitas, S. R.: A scale and aerosol aware stochastic convective parameterization for weather and air quality modeling, Atmos. Chem. Phys. Discuss., 14(10), 5233–5250, doi:10.5194/acp-14-5233-2014, 2014.

Grell, G. A., Peckham, S. E., Schmitz, R., McKeen, S. A., Frost, G., Skamarock, W. C. and Eder, B.: Fully coupled "online" chemistry within the WRF model, Atmos. Environ., 39(37), 6957–6975, doi:10.1016/j.atmosenv.2005.04.027, 2005.

Guenther, A., Karl, T., Harley, P., Wiedinmyer, C., Palmer, P. I. and Geron, C.: Estimates of global terrestrial isoprene emissions using MEGAN (Model of Emissions of Gases and Aerosols from Nature), Atmos. Chem. Phys., 6(11), 3181–3210, doi:10.5194/acp-6-3181-2006, 2006.

Guenther, A. B., Jiang, X., Heald, C. L., Sakulyanontvittaya, T., Duhl, T., Emmons, L. K. and Wang, X.: The model of emissions of gases and aerosols from nature version 2.1 (MEGAN2.1): An extended and updated framework for modeling biogenic emissions, Geosci. Model Dev., 5(6), 1471–1492, doi:10.5194/gmd-5-1471-2012, 2012.

Halliday, H., Thompson, A. M., Wisthaler, A., Blake, D. R., Hornbrook, R. S., Mikoviny, T., Muller, M., Eichler, P., Apel, E. C. and Hills, A. J.: Atmospheric benzene observations from oil and gas production in the Denver-Julesburg Basin in July and August 2014, J. Geophys. Res. Atmos., 121(18), doi:10.1002/ 2016JD025327., 2016.

Hansen, P. C.: Rank-deficient and discrete ill-posed problems: numerical aspects of linear inversion, Siam., 2005.

Harris, L. and Kotamarthi, V. R.: The Characteristics of the Chicago Lake Breeze and Its Effects on Trace Particle Transport: Results from an Episodic Event Simulation, J. Appl. Meteorol., 44(11), 1637–1654, doi:10.1175/JAM2301.1, 2005.

Harrison, M. R., Galloway, K. E., Shires, T. M. and Allen, D.: Natural Gas Industry Methane Emission Factor Improvement Study Final Report, , (December 2011), 1–53 [online] Available from: http://www.utexas.edu/research/ceer/GHG/files/FReports/XA_83376101_Final_Report.pdf, 2011.

Hausmann, P., Sussmann, R. and Smale, D.: Contribution of oil and natural gas production to renewed increase in atmospheric methane (2007-2014): Top-down estimate from ethane and methane column observations, Atmos. Chem. Phys., 16(5), 3227–3244, doi:10.5194/acp-16-3227-2016, 2016.

Helmig, D., Rossabi, S., Hueber, J., Tans, P., Montzka, S. A., Masarie, K., Thoning, K., Plass-Duelmer, C., Claude, A., Carpenter, L. J., Lewis, A. C., Punjabi, S., Reimann, S., Vollmer, M. K., Steinbrecher, R., Hannigan, J. W., Emmons, L. K., Mahieu, E., Franco, B., Smale, D. and Pozzer, A.: Reversal of global atmospheric ethane and propane trends largely due to US oil and natural gas production, Nat. Geosci., 9(July), 490–495, doi:10.1038/ngeo2721, 2016.

Henze, D. K., Hakami, A. and Seinfeld, J. H.: Development of the adjoint of GEOS-Chem, Atmos. Chem. Phys. Discuss., 6(5), 10591–10648, doi:10.5194/acpd-6-10591-2006, 2006.

Henze, D. K., Seinfeld, J. H. and Shindell, D. T.: Inverse modeling and mapping US air quality influences of inorganic $PM_{2.5}$ precursor emissions using the adjoint of GEOS-Chem, Atmos. Chem. Phys. Discuss., 8, 15031–15099, doi:10.5194/acpd-8-15031-2008, 2008.

Hong, S.-Y., Noh, Y. and Dudhia, J.: A new vertical diffusion package with an explicit treatment of entrainment processes., Mon. Weather Rev., 134(9), 2318–2341, doi:10.1175/MWR3199.1, 2006.

Howarth, R. W., Santoro, R. and Ingraffea, A.: Methane and the greenhouse-gas footprint of natural gas from shale formations, Clim. Change, 106(4), 679–690, doi:10.1007/s10584-011-0061-5, 2011.

Hu, X. M., Nielsen-Gammon, J. W. and Zhang, F.: Evaluation of three planetary boundary layer schemes in the WRF model, J. Appl. Meteorol. Climatol., 49(9), 1831–1844, doi:10.1175/2010JAMC2432.1, 2010.

Huang, M., Carmichael, G. R., Crawford, J. H., Wisthaler, A., Zhan, X., Hain, C. R., Lee, P. and Guenther, A. B.: Biogenic isoprene emissions driven by regional weather predictions using different initialization methods: Case studies during the SEAC4RS and DiSCOVER-AQ airborne campaigns, Geosci. Model Dev., 10(8), 3085–3104, doi:10.5194/gmd-10-3085-2017, 2017.

Iacono, M. J., Delamere, J. S., Mlawer, E. J., Shephard, M. W., Clough, S. A. and Collins, W. D.: Radiative forcing by long-lived greenhouse gases: Calculations with the AER radiative transfer models, J. Geophys. Res. Atmos., 113(13), 2–9, doi:10.1029/2008JD009944, 2008.

Inness, A., Baier, F., Benedetti, A., Bouarar, I., Chabrillat, S., Clark, H., Clerbaux, C., Coheur, P., Engelen, R. J., Errera, Q., Flemming, J., George, M., Granier, C., Hadji-Lazaro, J., Huijnen, V., Hurtmans, D., Jones, L., Kaiser, J. W., Kapsomenakis, J., Lefever, K., Leitão, J., Razinger, M., Richter, A., Schultz, M. G., Simmons, A. J., Suttie, M., Stein, O., Thépaut, J. N., Thouret, V., Vrekoussis, M. and Zerefos, C.: The MACC reanalysis: An 8 yr data set of atmospheric composition, Atmos. Chem. Phys., 13(8), 4073–4109, doi:10.5194/acp-13-4073-2013, 2013.

Janjic, Z.: Nonsingular Implementation of the Mellor-Yamada Level 2.5 Scheme in the NCEP Meso model, Natl. Centers Environ. Predict., 1–61, 2001.

Janjic, Z., Emanuel, K. and M., Z.-R.: Comments on “Development and Evaluation of a Convection Scheme for Use in Climate Models,” J. Atmos. Sci., 57(21), 3686–3686, 2000.

Jin, J., Miller, N. L. and Schlegel, N.: Sensitivity Study of Four Land Surface Schemes in the WRF Model, Adv. Meteorol., 2010, 1–11, doi:10.1155/2010/167436, 2010.

Jin, X., Fiore, A. M., Murray, L. T., Valin, L. C., Lamsal, L. N., Duncan, B., Folkert Boersma, K., De Smedt, I., Abad, G. G., Chance, K. and Tonnesen, G. S.: Evaluating a Space-Based Indicator of Surface Ozone-NOx-VOC Sensitivity Over Midlatitude Source Regions and Application to Decadal Trends, J. Geophys. Res. Atmos., 122(19), 10439–10461, doi:10.1002/2017JD026720, 2017.

Karion, A., Sweeney, C., Pétron, G., Frost, G., Michael Hardesty, R., Kofler, J., Miller, B. R., Newberger, T., Wolter, S., Banta, R., Brewer, A., Dlugokencky, E., Lang, P., Montzka, S. A., Schnell, R., Tans, P., Trainer, M., Zamora, R. and Conley, S.: Methane emissions estimate from airborne measurements over a western United States natural gas field, Geophys. Res. Lett., 40(16), 4393–4397, doi:10.1002/grl.50811, 2013.

Karion, A., Sweeney, C., Kort, E. A., Shepson, P. B., Brewer, A., Cambaliza, M., Conley, S. A., Davis, K., Deng, A., Hardesty, M., Herndon, S. C., Lauvaux, T., Lavoie, T., Lyon, D., Newberger, T., Pétron, G., Rella, C., Smith, M., Wolter, S., Yacovitch, T. I. and Tans, P.: Aircraft-Based Estimate of Total Methane Emissions from the Barnett Shale Region, Environ. Sci. Technol., 49(13), 8124–8131, doi:10.1021/acs.est.5b00217, 2015.

Kille, N., Baidar, S., Handley, P., Ortega, I., Sinreich, R., Cooper, O. R., Hase, F., Hannigan, J. W., Pfister, G. and Volkamer, R.: The CU Mobile Solar Occultation Flux instrument: structure functions and emission rates of NH3, NO2, C2H6, Atmos. Meas. Tech. Discuss., (October), 1–46, doi:10.5194/amt-2016-190, 2017.

Kim, S. W., Heckel, A., Frost, G. J., Richter, A., Gleason, J., Burrows, J. P., McKeen, S., Hsie, E. Y., Granier, C. and Trainer, M.: NO2 columns in the western United States observed from space and simulated by a regional chemistry model and their implications for NOx emissions, J. Geophys. Res. Atmos., 114(11), 1–29, doi:10.1029/2008JD011343, 2009.

Kirschke, S., Bousquet, P., Ciais, P., Saunois, M., Canadell, J. G., Dlugokencky, E. J., Bergamaschi, P., Bergmann, D., Blake, D. R., Bruhwiler, L., Cameron-Smith, P., Castaldi, S., Chevallier, F., Feng, L., Fraser, A., Heimann, M., Hodson, E. L., Houweling, S., Josse, B., Fraser, P. J., Krummel, P. B., Lamarque, J.-F., Langenfelds, R. L., Le Quéré, C., Naik, V., O'Doherty, S., Palmer, P. I., Pison, I., Plummer, D., Poulter, B., Prinn, R. G., Rigby, M., Ringeval, B., Santini, M., Schmidt, M., Shindell, D. T., Simpson, I. J., Spahni, R., Steele, L. P., Strode, S. a., Sudo, K., Szopa, S., van der Werf, G. R., Voulgarakis, A., van Weele, M., Weiss, R. F., Williams, J. E. and Zeng, G.: Three decades of global methane sources and sinks, Nat. Geosci., 6(September), 813–823, doi:10.1038/ngeo1955, 2013.

Kort, E. A., Frankenberg, C., Costigan, K. R., Lindenmaier, R., Dubey, M. K., Wunch, D. and Al, K. E. T.: Four corners: The largest US methane anomaly viewed from space, Geophys. Res. Lett., 6898–6903, doi:10.1002/2014GL061503.Received, 2014.

Kort, E. A., Smith, M. L., Murray, L. T., Gvakharia, A., Brandt, A. R., Peischl, J., Ryerson, T. B., Sweeney, C. and Travis, K.: Fugitive emissions from the Bakken shale illustrate role of shale production in global ethane shift, Geophys. Res. Lett., 43(9), 4617–4623, doi:10.1002/2016GL068703, 2016.

Lamarque, J. F., Bond, T. C., Eyring, V., Granier, C., Heil, A., Klimont, Z., Lee, D., Liousse, C., Mieville, A., Owen, B., Schultz, M. G., Shindell, D., Smith, S. J., Stehfest, E., Van Aardenne, J., Cooper, O. R., Kainuma, M., Mahowald, N., McConnell, J. R., Naik, V., Riahi, K. and Van Vuuren, D. P.: Historical (1850-2000) gridded anthropogenic and biomass burning emissions of reactive gases and aerosols: Methodology and application, Atmos. Chem. Phys., 10(15), 7017–7039, doi:10.5194/acp-10-7017-2010, 2010.

Lelieveld, J., Barlas, C., Giannadaki, D. and Pozzer, A.: Model calculated global, regional and megacity premature mortality due to air pollution, Atmos. Chem. Phys., 13(14), 7023–7037, doi:10.5194/acp-13-7023-2013, 2013.

Lelieveld, J., Evans, J. S., Fnais, M., Giannadaki, D. and Pozzer, A.: The contribution of outdoor air pollution sources to premature mortality on a global scale, Nature, 525(7569), 367–371, doi:10.1038/nature15371, 2015.

Lennartson, G. J. and Schwartz, M. D.: A synoptic climatology of surface-level ozone in Eastern Wisconsin, USA, Clim. Res., 13(3), 207–220, doi:10.3354/cr013207, 1999.

Levi, M.: Climate consequences of natural gas as a bridge fuel, Clim. Change, 118(3–4), 609–623, doi:10.1007/s10584-012-0658-3, 2013.

LMOS 2017 Study Team: 2017 Lake Michigan Ozone Study (LMOS) Preliminary Finding Report. [online] Available from: https://www.ladco.org/wp-content/uploads/Documents/LMOS_LADCO_report_final_draft_20180719.pdf, 2018.

Luecken, D. J., Hutzell, W. T., Strum, M. L. and Pouliot, G. A.: Regional sources of atmospheric formaldehyde and acetaldehyde, and implications for atmospheric modeling, Atmos. Environ., 47(2), 477–490, doi:10.1016/j.atmosenv.2011.10.005, 2012.

Lyon, D. R.: Methane Emissions from the Natural Gas Supply Chain, in Environmental and Health Issues in Unconventional Oil and Gas Development, pp. 33–48, Elsevier Inc., 2015.

Lyons, W. A. and Olsson, L. E.: Detailed mesometeorological studies of air pollution dispersion in the Chicago lake breeze, Mon. Weather Rev., 101(5), 387–403, doi:10.1175/1520-0493(1973)1012.3.CO;2, 1973.

McDuffie, E. E., Edwards, P. M., Gilman, J. B., Lerner, B. M., Dube, W. P., Trainer, M., Wolfe, D. E., Angevine, W. M., DeGouw, J., Williams, E. J., Tevlin, A. G., Murphy, J. G., Fischer, E. V., McKeen, S., Ryerson, T. B., Peischl, J., Holloway, J. S., Aikin, K., Langfor, A. O., Sneff, C. J., Alvarez II, R. J., Hall, S. R., Ullmann, K., Lantz, K. O. and Brown, S. S.: Influence of oil and gas emissions on summertime ozone in the Colorado Northen Front Range, J. Geophys. Res., 1–19, doi:doi:10.1002/2016JD025265., 2016.

McJeon, H., Edmonds, J., Bauer, N., Clarke, L., Fisher, B., Flannery, B. P., Hilaire, J., Krey, V., Marangoni, G., Mi, R., Riahi, K., Rogner, H. and Tavoni, M.: Limited impact on decadal-scale climate change from increased use of natural gas, Nature, 514(7523), 482–485, doi:10.1038/nature13837, 2014.

McKenzie, L. M., Witter, R. Z., Newman, L. S. and Adgate, J. L.: Human health risk assessment of air emissions from development of unconventional natural gas resources, Sci. Total Environ., 424, 79–87, doi:10.1016/j.scitotenv.2012.02.018, 2012.

McNider, R. T., Pour-Biazar, A., Doty, K., White, A., Wu, Y., Qin, M., Hu, Y., Odman, T., Cleary, P., Knipping, E., Dornblaser, B., Lee, P., Hain, C. and McKeen, S.: Examination of the Physical Atmosphere in the Great Lakes Region and its Potential Impact on Air Quality - Over-Water Stability and Satellite Assimilation, J. Appl. Meteorol. Climatol., JAMC-D-17-0355.1, doi:10.1175/JAMC-D-17-0355.1, 2018.

Miller, S. M., Wofsy, S. C., Michalak, A. M., Kort, E. A., Andrews, A. E., Biraud, S. C., Dlugokencky, E. J., Eluszkiewicz, J., Fischer, M. L., Janssens-Maenhout, G., Miller, B. R., Miller, J. B., Montzka, S. a, Nehrkorn, T. and Sweeney, C.: Anthropogenic emissions of methane in the United States., Proc. Natl. Acad. Sci. U. S. A., 110(50), 20018–22, doi:10.1073/pnas.1314392110, 2013.

Nakanishi, M. and Niino, H.: Development of an Improved Turbulence Closure Model for the Atmospheric Boundary Layer, J. Meteorol. Soc. Japan, 87(5), 895–912, doi:10.2151/jmsj.87.895, 2009.

Natarajan, M., Pierce, R. B., Schaack, T. K., Lenzen, A. J., Al-Saadi, J. A., Soja, A. J., Charlock, T. P., Rose, F. G., Winker, D. M. and Worden, J. R.: Radiative forcing due to enhancements in tropospheric ozone and carbonaceous aerosols caused by Asian fires during spring 2008, J. Geophys. Res. Atmos., 117(6), 1–18, doi:10.1029/2011JD016584, 2012.

National Centers for Environmental Prediction, National Weather Service, NOAA, U. S. D. of C.: NCEP FNL Operational Model Global Tropospheric Analyses, continuing from July 1999, , doi:10.5065/D6M043C6, 2000.

Nielsen-Gammon, J. W., Powell, C. A., Mahoney, M. J., Angevine, W. M., Senff, C., White, A., Berkowitz, C., Doran, C. and Knupp, K.: Multisensor Estimation of Mixing Heights over a Coastal City, J. Appl. Meteorol. Climatol., 27–43, doi:10.1175/2007JAMC1503.1, 2008.

Nisbet, E. G., Dlugokencky, E. J. and Bousquet, P.: Methane on the rise--again., Science, 343(6170), 493–5, doi:10.1126/science.1247828, 2014.

Nisbet, E. G., Dlugokencky, E. J., Manning, M. R., Lowry, D., Fisher, R. E., France, J. L., Michel, S. E., Miller, J. B., White, J. W. C., Vaughn, B., Bousquet, P., Pyle, J. A., Warwick, N. J., Cain, M., Brownlow, R., Zazzeri, G., Lanoiselle, M., Manning, A. C., Gloor, E., Worthy, D. E. J., Bunke, E.-G., Labuschagne C., Wolfe, E. W. and Ganesan, A. L.: Rising atmospheric methane: 2007-1014 growth and isotopic shift, Glob. Biogeochem. Cycles, 30, 1–15, doi:10.1002/2015GB005326.Received, 2016.

Olaguer, E. P.: The potential near-source ozone impacts of upstream oil and gas industry emissions, J. Air Waste Manag. Assoc., 62(8), 966–977, doi:10.1080/10962247.2012.688923, 2012.

Oltmans, S. J., Karion, a., Schnell, R. C., Pétron, G., Sweeney, C., Wolter, S., Neff, D., Montzka, S. a., Miller, B. R., Helmig, D., Johnson, B. J. and Hueber, J.: A high ozone episode in winter 2013 in the Uinta Basin oil and gas region characterized by aircraft measurements, Atmos. Chem. Phys. Discuss., 14(14), 20117–20157, doi:10.5194/acpd-14-20117-2014, 2014.

Omara, M., Sullivan, M. R., Li, X., Subramian, R., Robinson, A. L. and Presto, A. A.: Methane Emissions from Conventional and Unconventional Natural Gas Production Sites in the Marcellus Shale Basin, Environ. Sci. Technol., 50(4), 2099–2107, doi:10.1021/acs.est.5b05503, 2016.

Peischl, J., Karion, A., Sweeney, C., Kort, E. A., Smith, M. L., Brandt, A. R., Yeskoo, T., Aikin, K. C., Conley, S. A., Gvakharia, A., Trainer, M., Wolter, S. and Ryerson, T. B.: Quantifying atmospheric methane emissions from oil and natural gas production in the Bakken shale region of North Dakota, J. Geophys. Res. Atmos., 121, 6101–6111, doi:10.1002/2015JD024631, 2016.

Peischl, J., Eilerman, S. J., Neuman, J. A., Aikin, K. C., de Gouw, J., Gilman, J. B., Herndon, S. C., Nadkarni, R., Trainer, M., Warneke, C. and Ryerson, T. B.: Quantifying Methane and Ethane Emissions to the Atmosphere From Central and Western U.S. Oil and Natural Gas Production Regions, J. Geophys. Res. Atmos., 123(14), 7725–7740, doi:10.1029/2018JD028622, 2018.

Pétron, G., Frost, G., Miller, B. R., Hirsch, A. I., Montzka, S. A., Karion, A., Trainer, M., Sweeney, C., Andrews, A. E., Miller, L., Kofler, J., Bar-Ilan, A., Dlugokencky, E. J., Patrick, L., Moore, C. T., Ryerson, T. B., Siso, C., Kolodzey, W., Lang, P. M., Conway, T., Novelli, P., Masarie, K., Hall, B., Guenther, D., Kitzis, D., Miller, J., Welsh, D., Wolfe, D., Neff, W. and Tans, P.: Hydrocarbon emissions characterization in the Colorado Front Range: A pilot study, J. Geophys. Res. Atmos., 117(4), 1–19, doi:10.1029/2011JD016360, 2012.

Pétron, G., Karion, A., Sweeney, C., Miller, B. R., Montzka, S. A., Frost, G. J., Trainer, M., Tans, P., Andrews, A., Kofler, J., Helmig, D., Guenther, D., Dlugokencky, E., Lang, P., Newberger, T., Wolter, S., Hall, B., Novelli, P., Brewer, A., Conley, S., Hardesty, M., Banta, R., White, A., Noone, D., Wolfe, D. and Schnell, R.: A new look at methane and nonmethane hydrocarbon emissions from oil and natural gas operations in the Colorado Denver-Julesburg Basin, J. Geophys. Res. Atmos., 119(10), 5787–5805, doi:https://doi.org/10.1002/2013JD021272, 2014.

Pfister, G., Flocke, F., Hornbrook, R., Orlando, J. and Lee, S.: Process-Based and Regional Source Impact Analysis for FRAPPÉ and DISCOVER-AQ 2014. [online] Available from: https://www.colorado.gov/airquality/tech_doc_repository.aspx?action=open&file=FRAPPE-NCAR_Final_Report_July2017.pdf, 2017a.

Pfister, G. G., Reddy, P. J., Barth, M. C., Flocke, F. F., Fried, A., Herndon, S. C., Sive, B. C., Sullivan, J. T., Thompson, A. M., Yacovitch, T. I., Weinheimer, A. J. and Wisthaler, A.: Using Observations and Source-Specific Model Tracers to Characterize Pollutant Transport During FRAPPÉ and DISCOVER-AQ, J. Geophys. Res. Atmos., 122(19), 10510–10538, doi:10.1002/2017JD027257, 2017b.

Pierce, R. B., Schaack, T., Al-Saadi, J. A., Fairlie, T. D., Kittaka, C., Lingenfelser, G. S., Natarajan, M., Olson, J. R., Soja, A. J., Zapotocny, T., Lenzen, A., Stobie, J., Johnson, D., Avery, M. A., Sachse, G. W., Thompson, A., Cohen, R., Dibb, J. E., Crawford, J. H., Rault, D. F., Martin, R., Szykman, J. and Fishman, J.: Chemical data assimilation estimates of continental U.S. ozone and nitrogen budgets during the Intercontinental Chemical Transport Experiment-North America, J. Geophys. Res. Atmos., 112(12), doi:10.1029/2006JD007722, 2007.

Prenni, A. J., Day, D. E., Evanoski-Cole, A. R., Sive, B. C., Hecobian, A., Zhou, Y., Gebhart, K. A., Hand, J. L., Sullivan, A. P., Li, Y., Schurman, M. I., Desyaterik, Y., Malm, W. C., Collett, J. L. and Schichtel, B. A.: Oil and gas impacts on air quality in federal lands in the Bakken region: An overview of the Bakken Air Quality Study and first results, Atmos. Chem. Phys., 16(3), 1401–1416, doi:10.5194/acp-16-1401-2016, 2016.

Rappenglück, B., Ackermann, L., Alvarez, S., Golovko, J., Buhr, M., Field, R. A., Soltis, J., Montague, D. C., Hauze, B., Adamson, S., Risch, D., Wilkerson, G., Bush, D., Stoeckenius, T. and Keslar, C.: Strong wintertime ozone events in the Upper Green River basin, Wyoming, Atmos. Chem. Phys., 14(10), 4909–4934, doi:10.5194/acp-14-4909-2014, 2014.

Richter, D., Weibring, P., Walega, J. G., Fried, A., Spuler, S. M. and Taubman, M. S.: Compact highly sensitive multi-species airborne mid-IR spectrometer, Appl. Phys. B Lasers Opt., 119(1), 119–131, doi:10.1007/s00340-015-6038-8, 2015.

Saide, P. E., Carmichael, G. R., Spak, S. N., Gallardo, L., Osses, A. E., Mena-Carrasco, M. A. and Pagowski, M.: Forecasting urban PM10 and PM2.5 pollution episodes in very stable nocturnal conditions and complex terrain using WRF-Chem CO tracer model, Atmos. Environ., 45(16), 2769–2780, doi:10.1016/j.atmosenv.2011.02.001, 2011.

Saide, P. E., Carmichael, G. R., Spak, S. N., Minnis, P. and Ayers, J. K.: Improving aerosol distributions below clouds by assimilating satellite-retrieved cloud droplet number, Proc. Natl. Acad. Sci., 109(30), 11939–11943, doi:10.1073/pnas.1205877109, 2012.

Saide, P. E., Peterson, D. A., Da Silva, A., Anderson, B., Ziemba, L. D., Diskin, G., Sachse, G., Hair, J., Butler, C., Fenn, M., Jimenez, J. L., Campuzano-Jost, P., Perring, A. E., Schwarz, J. P., Markovic, M. Z., Russell, P., Redemann, J., Shinozuka, Y., Streets, D. G., Yan, F., Dibb, J., Yokelson, R., Toon, O. B., Hyer, E. and Carmichael, G. R.: Revealing important nocturnal and day-to-day variations in fire smoke emissions through a multiplatform inversion, Geophys. Res. Lett., 42(9), 3609–3618, doi:10.1002/2015GL063737, 2015.

Saunois, M., Bousquet, P., Poulter, B., Peregon, A., Ciais, P., Canadell, J. G., Dlugokencky, E. J., Etiope, G., Bastviken, D., Houweling, S., Janssens-Maenhout, G., Tubiello, F. N., Castaldi, S., Jackson, R. B., Alexe, M., Arora, V. K., Beerling, D. J., Bergamaschi, P., Blake, D. R., Brailsford, G., Brovkin, V., Bruhwiler, L., Crevoisier, C., Crill, P., Curry, C., Frankenberg, C., Gedney, N., Höglund-Isaksson, L., Ishizawa, M., Ito, A., Joos, F., Kim, H.-S., Kleinen, T., Krummel, P., Lamarque, J.-F., Langenfelds, R., Locatelli, R., Machida, T., Maksyutov, S., McDonald, K. C., Marshall, J., Melton, J. R., Morino, I., O'Doherty, S., Parmentier, F.-J. W., Patra, P. K., Peng, C., Peng, S., Peters, G. P., Pison, I., Prigent, C., Prinn, R., Ramonet, M., Riley, W. J., Saito, M., Schroder, R., Simpson, I. J., Spahni, R., Steele, P., Takizawa, A., Thorton, B. F., Tian, H., Tohjima, Y., Viovy, N., Voulgarakis, A., van Weele, M., van der Werf, G., Weiss, R., Wiedinmyer, C., Wilton, D. J., Wiltshire, A., Worthy, D., Wunch, D. B., Xu, X., Yoshida, Y., Zhang, B., Zhang, Z. and Zhu, Q.: The Global Methane Budget: 2000-2012, Earth Syst. Sci. Data Discuss., (June), 1–79, doi:10.5194/essd-2016-25, 2016.

Schaefer, H., Mikaloff Fletcher, S. E., Veidt, C., Lassey, K. R., Brailsford, G. W., Bromley, T. M., Dlugokencky, E. J., Michel, S. E., Miller, J. B., Levin, I., Lowe, D. C., Martin, R. J., Vaughn, B. H., White, J. W. C., Fletcher, S. E. M., Veidt, C., Lassey, K. R., Brailsford, G. W., Bromley, T. M., Dlugokencky, E. J., Michel, S. E., Miller, J. B., Levin, I., Lowe, D. C., Martin, R. J., Vaughn, B. H. and White, J. W. C.: A 21st-century shift from fossil-fuel to biogenic methane emissions indicated by 13CH4, Science (80-.)., 351(6281), 80–84, doi:10.1126/science.aad2705, 2016.

Schneising, O., Burrows, J. P., Dickerson, R. R., Buchwitz, M. and Bovensmann, H.: Remote sensing of fugitive methane emissions from oil and gas production in North American tight geologic formations Earth ' s Future, Earth's Futur., 2(10), 1–11, doi:10.1002/2014EF000265.Received, 2014.

Seinfeld, J. and Pandis, S.: Atmospheric chemistry and physics: from air pollution to climate change, John Wiley & Sons., 2012.

Shindell, D., Kuylenstierna, J. C. I., Vignati, E., van Dingenen, R., Amann, M., Klimont, Z., Anenberg, S. C., Muller, N., Janssens-Maenhout, G., Raes, F., Schwartz, J., Faluvegi, G., Pozzoli, L., Kupiainen, K., Hoglund-Isaksson, L., Emberson, L., Streets, D., Ramanathan, V., Hicks, K., Oanh, N. T. K., Milly, G., Williams, M., Demkine, V. and Fowler, D.: Simultaneously Mitigating Near-Term Climate Change and Improving Human Health and Food Security, Science (80-.)., 335(6065), 183–189, doi:10.1126/science.1210026, 2012.

Sillman, S.: The use of NOy, H2O2, and HNO3 as indicators for ozone-NOx -hydrocarbon sensitivity in urban locations, J. Geophys. Res. Atmos., 100(D7), 14175–14188, doi:10.1029/94JD02953, 1995.

Silva, R. A., West, J. J., Zhang, Y., Anenberg, S. C., Lamarque, J. F., Shindell, D. T., Collins, W. J., Dalsoren, S., Faluvegi, G., Folberth, G., Horowitz, L. W., Nagashima, T., Naik, V., Rumbold, S., Skeie, R., Sudo, K., Takemura, T., Bergmann, D., Cameron-Smith, P., Cionni, I., Doherty, R. M., Eyring, V., Josse, B., Mackenzie, I. A., Plummer, D., Righi, M., Stevenson, D. S., Strode, S., Szopa, S. and Zeng, G.: Global premature mortality due to anthropogenic outdoor air pollution and the contribution of past climate change, Environ. Res. Lett., 8(3), doi:10.1088/1748-9326/8/3/034005, 2013.

Skamarock, W. C., Klemp, J. B., Dudhia, J., O., G. D. and Barker, D. M.: A description of the Advanced Research WRF version 3. NCAR Tech. Note NCAR/TN-4751STR, 2008.

Smith, M. L., Kort, E. A., Karion, A., Sweeney, C., Herndon, S. C. and Yacovitch, T. I.: Airborne Ethane Observations in the Barnett Shale: Quantification of Ethane Flux and Attribution of Methane Emissions, Environ. Sci. Technol., 49(13), 8158–8166, doi:10.1021/acs.est.5b00219, 2015.

Stockwell, W. R., Middleton, P., Chang, J. S. and Tang, X.: The second generation regional acid deposition model chemical mechanism for regional air quality modeling, J. Geophys. Res., 95(D10), 16343, doi:10.1029/JD095iD10p16343, 1990.

Stockwell, W. R., Kirchner, F., Kuhn, M. and Seefeld, S.: A new mechanism for regional atmospheric chemistry modeling, J. Geophys. Res., 102(D22), 25847, doi:10.1029/97JD00849, 1997.

Stull, R. B.: An introduction to boundary layer meteorology, Springer Science & Business Media., 1988.

Thompson, C. R., Hueber, J. and Helmig, D.: Influence of oil and gas emissions on ambient atmospheric non-methane hydrocarbons in residential areas of Northeastern Colorado, Elem. Sci. Anthr., 2, 000035, doi:10.12952/journal.elementa.000035, 2014.

Tonnesen, G. S. and Dennis, R. L.: Analysis of radical propagation efficiency to assess ozone sensitivity to hydrocarbons and NOx1. Local indicators of instantaneous odd oxygen production sensitivity, J. Geophys. Res. Atmos., 105(D7), 9213–9225, doi:10.1029/1999JD900371, 2000.

Townsend-Small, A., Tyler, S. C., Pataki, D. E., Xu, X. and Christensen, L. E.: Isotopic measurements of atmospheric methane in Los Angeles, California, USA: Influence of "fugitive" fossil fuel emissions, J. Geophys. Res. Atmos., 117(7), 1–11, doi:10.1029/2011JD016826, 2012.

Turner, A. J., Jacob, D. J., Wecht, K. J., Maasakkers, J. D., Lundgren, E., Andrews, a. E., Biraud, S. C., Boesch, H., Bowman, K. W., Deutscher, N. M., Dubey, M. K., Griffith, D. W. T., Hase, F., Kuze, A., Notholt, J., Ohyama, H., Parker, R., Payne, V. H., Sussmann, R., Sweeney, C., Velazco, V. a., Warneke, T., Wennberg, P. O. and Wunch, D.: Estimating global and North American methane emissions with high spatial resolution using GOSAT satellite data, Atmos. Chem. Phys., 15(12), 7049–7069, doi:10.5194/acp-15-7049-2015, 2015.

Turner, A. J., Jacob, D. J., Benmergui, J., Wofsy, S. C., Maasakkers, J. D., Butz, A., Hasekamp, O. and Biraud, S. C.: A large increase in U.S. methane emissions over the past decade inferred from satellite data and surface observations, Geophys. Res. Lett., 43(5), 2218–2224, doi:10.1002/2016GL067987, 2016.

U.S. Energy Information Administration: International Energy Outlook 2016-Electricity, in International Energy Outlook, pp. 81–100. [online] Available from: http://www.eia.gov/forecasts/ieo/pdf/0484(2016).pdf, 2016.

U.S. Environmental Protection Agency: 2011 National Emissions Inventory, version 2 Technical Support Document. [online] Available from: https://www.epa.gov/sites/production/files/2015-10/documents/nei2011v2_tsd_14aug2015.pdf, 2015.

UCAR/NCAR/CISL/TDD: The NCAR Command Language (Version 6.4.0) [Software]., 2017.

United States Environmental Protection Agency (EPA): NAAQS Table, [online] Available from: https://www.epa.gov/criteria-air-pollutants/naaqs-table, 2015.

United States Environmental Protection Agency (EPA): Current Nonattainment Counties for All Criteria Pollutants, [online] Available from: https://www3.epa.gov/airquality/greenbook/ancl.html (Accessed 10 February 2018), 2018.

United States Government Publishing Office: Electronic Code of Federal Regulations Title 40 Part 60. Standards of Performance for New Stationary Sources: Subpart OOOO – Standards of Performance for Crude Oil and Natural Gas Production, Transmission and Distribution, 2015.

Valerino, M. J., Johnson, J. J., Izumi, J., Orozco, D., Hoff, R. M., Delgado, R. and Hennigan, C. J.: Sources and composition of PM2.5 in the Colorado Front Range during the DISCOVER-AQ study, J. Geophys. Res. Atmos., 122(1), 566–582, doi:10.1002/2016JD025830, 2017.

Vu, K. T., Dingle, J. H., Bahreini, R., Reddy, P. J., Campos, T. L., Diskin, G. S., Fried, A., Herndon, S. C., Hornbrook, R. S., Huey, G., Kaser, L., Montzka, D. D., Nowak, J. B., Richter, D., Roscioli, J. R., Shertz, S., Stell, M., Tanner, D., Tyndall, G., Walega, J., Weibring, P., Weinheimer, A. J., Pfister, G. and Flocke, F.: Impacts of the Denver Cyclone on Regional Air Quality and Aerosol Formation in the Colorado Front Range during FRAPPÉ 2014, Atmos. Chem. Phys. Discuss., (3), 1–40, doi:10.5194/acp-2016-532, 2016.

Wecht, K. J., Jacob, D. J., Frankenberg, C., Jiang, Z. and Blake, D. R.: Mapping of North American methane emissions with high spatial resolution by inversion of SCIAMACHY satellite data, J. Geophys. Res. Atmos. Res., 7741–7756, doi:10.1002/2014JD021551.Received, 2014.

Wigley, T. M. L.: Coal to gas: The influence of methane leakage, Clim. Change, 108(3), 601–608, doi:10.1007/s10584-011-0217-3, 2011.

Xiao, Y., Logan, J. A., Jacob, D. J., Hudman, R. C., Yantosca, R. and Blake, D. R.: Global budget of ethane and regional constraints on U.S. sources, J. Geophys. Res. Atmos., 113(21), 1–13, doi:10.1029/2007JD009415, 2008.

Yacovitch, T. I., Herndon, S. C., Roscioli, J. R., Floerchinger, C., McGovern, R. M., Agnese, M., Pétron, G., Kofler, J., Sweeney, C., Karion, A., Conley, S. A., Kort, E. A., Nähle, L., Fischer, M., Hildebrandt, L., Koeth, J., McManus, J. B., Nelson, D. D., Zahniser, M. S. and Kolb, C. E.: Demonstration of an ethane spectrometer for methane source identification, Environ. Sci. Technol., 48(14), 8028–8034, doi:10.1021/es501475q, 2014.

Zavala-Araiza, D., Lyon, D. R., Alvarez, R. A., Davis, K. J., Harriss, R., Herndon, S. C., Karion, A., Kort, E. A., Lamb, B. K., Lan, X., Marchese, A. J., Pacala, S. W., Robinson, A. L., Shepson, P. B., Sweeney, C., Talbot, R., Townsend-Small, A., Yacovitch, T. I., Zimmerle, D. J. and Hamburg, S. P.: Reconciling divergent estimates of oil and gas methane emissions, Proc. Natl. Acad. Sci., 112(51), 15597–15602, doi:10.1073/pnas.1522126112, 2015.

Zhu, C., Byrd, R. H., Lu, P. and Nocedal, J.: Algorithm 778: L-BFGS-B: Fortran subroutines for large-scale bound-constrained optimization, ACM Trans. Math. Softw., 23(4), 550–560, doi:10.1145/279232.279236, 1997.

APPENDIX

For quantitative comparison between the simulations we used statistical measures including correlation coefficient (R), root mean square error (RMSE), mean absolute error (MAE), mean bias (MB), and normalized mean bias (NMB). Definitions of these metrics can be found below:

$$R = \frac{\overline{(C_o - \overline{C_o})(C_p - \overline{C_p})}}{\sigma_{Cp}\sigma_{Co}} \quad (1)$$

$$RMSE = \sqrt{\frac{\sum_{i=1}^{n}\left(C_{p_i} - C_{o_i}\right)^2}{n}} \quad (2)$$

$$MAE = \frac{1}{n}\sum_{i=1}^{n}\left|C_{p_i} - C_{o_i}\right| \quad (3)$$

$$MB = \frac{1}{n}\sum_{i=1}^{n}\left(C_{p_i} - C_{o_i}\right) \quad (4)$$

$$NMB = \frac{\left(\overline{C_p} - \overline{C_o}\right)}{\overline{C_o}} \times 100\% \quad (5)$$

Where C_o is the observation value, C_p is the model value, σ is the standard deviation, $\bar{C}$ is the mean value, and n is total number of observation points

Table A-1. Conversion table used to map species from NEI-2011 emission inventory to RACM chemical mechanism in and MADE/SORGAM aerosol module

Emission inventory name	WRF-Chem name	Weight	Species name
CO	e_co	1.00	Carbon monoxide
NOX	e_no	1.00	Nitrogen Oxides (NO or NO2)
SO2	e_so2	1.00	Sulfur dioxide
NH3	e_nh3	1.00	Ammonia
HC01	e_ch4	1.00	Methane
HC02	e_eth	1.00	Ethane kOH<500 /ppm/min
HC03	e_hc3	1.00	Alkane 500<kOH<2500 exclude(C3H8,C2H2,ethanol,acids)
HC04	e_hc3	1.11	Alkane 2500<kOH<5000 exlude(butanes)
HC05	e_hc5	0.97	Alkane 5000<kOH<10000 exlude(pentanes)
HC06	e_hc8	1.00	Alkane kOH>10000 exclude(ethylene glycol)
HC07	e_ol2	1.00	Ethylene
HC08	e_olt	1.00	Alkene kOH <20000 /ppm/min
HC09	e_oli	1.00	Alkene kOH >20000 /ppm/min exclude(dienes,styrenes)
HC10	e_iso	1.00	Isoprene
HC12	e_tol	1.00	Aromatic kOH <20000 /ppm/min exclude(benzene and toluene)
HC13	e_xyl	1.00	Aromatic kOH >20000 /ppm/min exclude(xylenes)
HC14	e_hcho	1.00	Formaldehyde
HC15	e_ald	1.00	Acetaldehyde
HC16	e_ald	1.00	Higher aldehydes
HC17	e_ald	1.00	Benzaldehyde
HC18	e_ket	0.33	Acetone
HC19	e_ket	1.61	Methylethyl ketone
HC20	e_ket	1.61	PRD2 SAPRAC species (aromatic ketones)
HC21	e_hc3	0.40	Methanol
HC22	e_ald	1.00	Glyoxal
HC23	e_ald	1.00	Methylglyoxal
HC24	e_ald	1.00	Biacetyl
HC25	e_csl	1.00	Phenols
HC26	e_csl	1.00	Cresols
HC27	e_ald	0.50	Methacrolein
HC27	e_olt	0.50	Methacrolein

Table A-1 continued

HC28	e_ket	0.50	Methylvinyl ketone
HC28	e_olt	0.50	Methylvinyl ketone
HC29	e_ket	1.00	IPRD SAPRAC species (>C4 unsaturated aldehydes)
HC31	e_ora2	1.00	Acetic Acid
HC32	e_ora2	1.00	>C2 Acids (SAPRC PACD species)
HC33	e_csl	1.00	Xylenols (SAPRC-11 species)
HC34	e_csl	1.00	Catechols (SAPRC-11 species)
HC36	e_olt	1.00	Propylene
HC37	e_hc3	0.40	Acetylene
HC38	e_tol	0.29	Benzene
HC39	e_hc3	1.11	Butanes
HC40	e_hc5	0.97	Pentanes
HC41	e_tol	1.00	Toluene
HC42	e_xyl	1.00	m-Xylene
HC43	e_xyl	1.00	p-Xylene
HC44	e_xyl	1.00	o-Xylene
HC45	e_hc3	0.57	Propane
HC46	e_oli	1.00	Dienes
HC47	e_olt	1.00	Styrenes
HC47	e_tol	1.00	Styrenes
HC48	e_hc3	1.20	Ethanol
HC49	e_hc8	1.14	Ethylene Glycol
PM01	e_pm25i	0.20	Unspeciated primary PM2.5 - nuclei mode
PM01	e_pm25j	0.80	Unspeciated primary PM2.5 - accumulation mode
PM02	e_so4i	0.20	Sulfate PM2.5 - nuclei mode
PM02	e_so4j	0.80	Sulfate PM2.5 - accumulation mode
PM03	e_no3i	0.20	Nitrate PM2.5 - nuclei mode
PM03	e_no3j	0.80	Nitrate PM2.5 - accumulation mode
PM04	e_orgi	0.20	Organic Carbon PM2.5 - nuclei mode
PM04	e_orgj	0.80	Organic Carbon PM2.5 - accumulation mode
PM05	e_eci	0.20	Elemental Carbon PM2.5 - nuclei mode
PM05	e_ecj	0.80	Elemental Carbon PM2.5 - accumulation mode
PM10-PRI	e_pm10	1.00	Unspeciated Primary PM10

Table A-2. Summary of model performance in capturing temperature at BAO 10m and 300m during Aug 1-15, 2014

T (C) - 10m	OBS	PBL			Met IC and BC		Initialization		Horizontal resolution	
		PBL1	PBL2	PBL3	Met5	Met6	Init4	Init5	Hor5	Hor5-12km
Mean	21.67	22.40	20.95	21.20	24.06	23.44	21.59	24.06	24.06	24.08
R		0.89	0.89	0.89	0.86	0.89	0.71	0.86	0.86	0.88
RMSE		2.05	2.03	2.01	3.25	2.63	2.99	3.25	3.25	3.18
MAE		1.56	1.62	1.59	2.60	2.05	2.30	2.60	2.60	2.53
MB		0.74	-0.72	-0.46	2.40	1.77	-0.08	2.40	2.40	2.41
NMB		3.4%	-3.3%	-2.1%	11.1%	8.2%	-0.4%	11.1%	11.1%	11.1%
T (C) - 300m	OBS	PBL1	PBL2	PBL3	Met5	Met6	Init4	Init5	Hor5	Hor5-12km
Mean		21.91	20.95	21.30	23.58	22.89	20.31	23.58	23.58	23.52
R		0.76	0.75	0.72	0.74	0.78	0.57	0.74	0.74	0.75
RMSE		2.16	2.14	2.10	2.79	2.27	3.09	2.79	2.79	2.80
MAE		1.69	1.73	1.68	2.24	1.76	2.45	2.24	2.24	2.21
MB		0.23	-0.73	-0.38	1.90	1.22	-1.37	1.90	1.90	1.85
NMB		1.1%	-3.4%	-1.8%	8.8%	5.6%	-6.3%	8.8%	8.8%	8.5%

Table A-3. Summary of model performance in capturing relative humidity (RH) at BAO 10m and 300m during Aug 1-15, 2014

		PBL			Met IC and BC		Initialization		Horizontal resolution	
RH (%)-10m	**OBS**	**PBL1**	**PBL2**	**PBL3**	**Met5**	**Met6**	**Init4**	**Init5**	**Hor5**	**Hor5-12km**
Mean	46.47	46.85	57.59	55.78	32.65	39.87	59.36	32.65	32.65	32.89
R		0.78	0.69	0.73	0.63	0.64	0.53	0.63	0.63	0.71
RMSE		10.89	16.90	15.13	19.13	14.95	22.33	19.13	19.13	18.15
MAE		8.45	14.38	12.86	15.01	11.31	18.10	15.01	15.01	14.43
MB		0.38	11.12	9.31	-13.81	-6.60	12.90	-13.51	-13.51	-13.58
NMB		0.8%	23.9%	20.0%	-29.7%	-14.2%	27.7%	-29.7%	-29.7%	-29.2%
RH (%)-300m	**OBS**	**PBL1**	**PBL2**	**PBL3**	**Met5**	**Met6**	**Init4**	**Init5**	**Hor5**	**Hor5-12km**
Mean	38.70	43.63	51.45	48.25	31.27	38.55	59.06	31.27	31.27	31.94
R		0.64	0.59	0.48	0.53	0.52	0.41	0.53	0.53	0.57
RMSE		13.06	17.92	15.25	12.66	11.14	28.39	12.66	12.66	12.11
MAE		9.92	14.78	12.77	9.73	8.60	23.19	9.73	9.73	9.29
MB		4.93	12.75	9.55	-7.43	-0.15	20.36	-7.43	-7.43	-6.76
NMB		12.7%	32.9%	24.7%	-19.2%	-0.4%	52.6%	-19.2%	-19.2%	-17.5%

Table A-4. Summary of model performance in capturing wind speed and direction at BAO 10m during Aug 1-15, 2014

			PBL			Met		Init		Horizontal Res.	
Day - 10 m		**OBS**	**PBL1**	**PBL2**	**PBL3**	**Met5**	**Met6**	**Init4**	**Init5**	**Hor5**	**Hor5-12km**
Wind Speed	**Mean**	2.46	2.99	2.68	2.20	2.63	2.83	3.30	2.63	2.63	2.58
	STD	1.25	1.47	1.55	1.27	1.41	1.51	2.02	1.41	1.41	1.33
Wind Direction	**Mean**	123.38	64.31	71.92	74.85	38.63	70.83	61.40	38.63	38.63	45.08
	STD	66.06	45.40	62.30	54.02	73.77	75.30	75.65	73.77	73.77	66.18
Night - 10 m		**OBS**	**PBL1**	**PBL2**	**PBL3**	**Met5**	**Met6**	**Init4**	**Init5**	**Hor5**	**Hor5-12km**
Wind Speed	**Mean**	2.25	2.81	2.58	2.18	2.51	2.72	2.91	2.51	2.51	2.66
	STD	0.96	1.41	0.94	0.96	1.35	1.43	1.40	1.35	1.35	1.41
Wind Direction	**Mean**	222.98	244.07	243.95	263.07	226.97	230.93	160.02	226.97	226.97	295.43
	STD	50.01	90.68	69.52	74.66	83.89	69.81	87.15	83.89	83.89	87.30

Table A-5. Summary of model performance in capturing wind speed and direction at BAO 300m during Aug 1-15, 2014

			PBL			Met		init		Horizontal Res.	
Day - 300 m		**OBS**	**PBL1**	**PBL2**	**PBL3**	**Met5**	**Met6**	**Init4**	**Init5**	**Hor5**	**Hor5-12km**
Wind Speed	Mean	3.23	3.89	3.51	2.78	2.88	3.22	3.83	2.88	2.88	2.77
	STD	2.24	2.15	2.39	1.61	1.58	1.81	2.93	1.58	1.58	1.47
Wind Direction	Mean	117.3	62.69	62.42	64.05	32.91	57.67	56.71	32.91	32.91	39.52
	STD	74.56	51.99	63.89	59.84	75.14	76.03	74.32	75.14	75.14	69.43
Night - 300 m			**PBL1**	**PBL2**	**PBL3**	**Met5**	**Met6**	**Init4**	**Init5**	**Hor5**	**Hor5-12km**
Wind Speed	Mean	3.42	5.00	4.34	3.80	4.21	4.60	5.07	4.21	4.21	4.89
	STD	2.59	2.68	2.95	2.64	2.64	2.47	3.07	2.64	2.64	3.29
Wind Direction	Mean Model	213.59	141.12	223.36	355.95	326.05	294.02	156.88	326.05	326.05	306.58
	STD Model	72.73	98.36	93.80	91.39	91.33	77.67	84.60	91.33	91.33	88.31

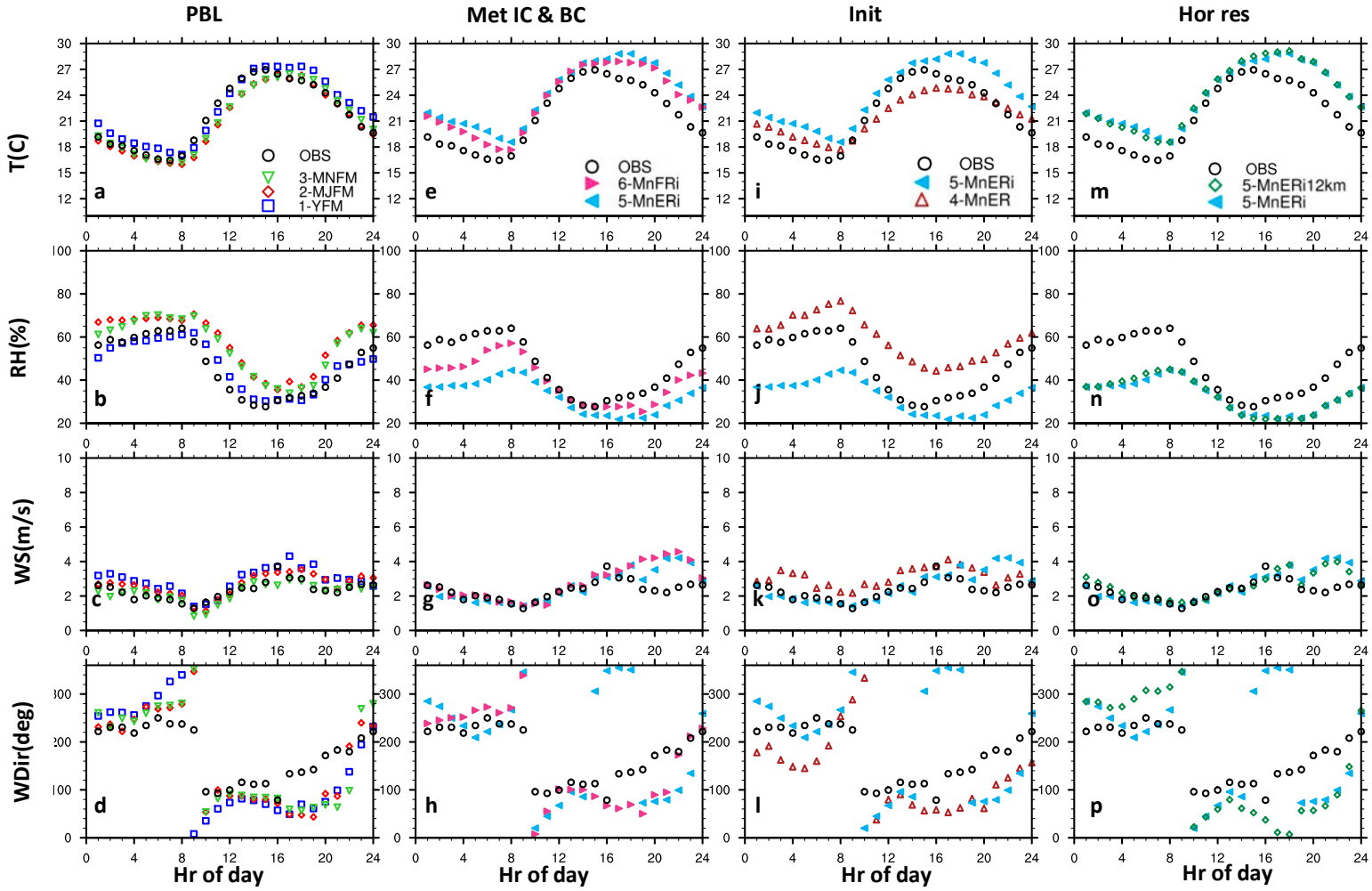

Figure A-1. Average diurnal cycle of temperature, relative humidity, wind speed, and wind direction for all test sets and observation at BAO 10m. Averages are calculated for Aug 1 to 15, 2014

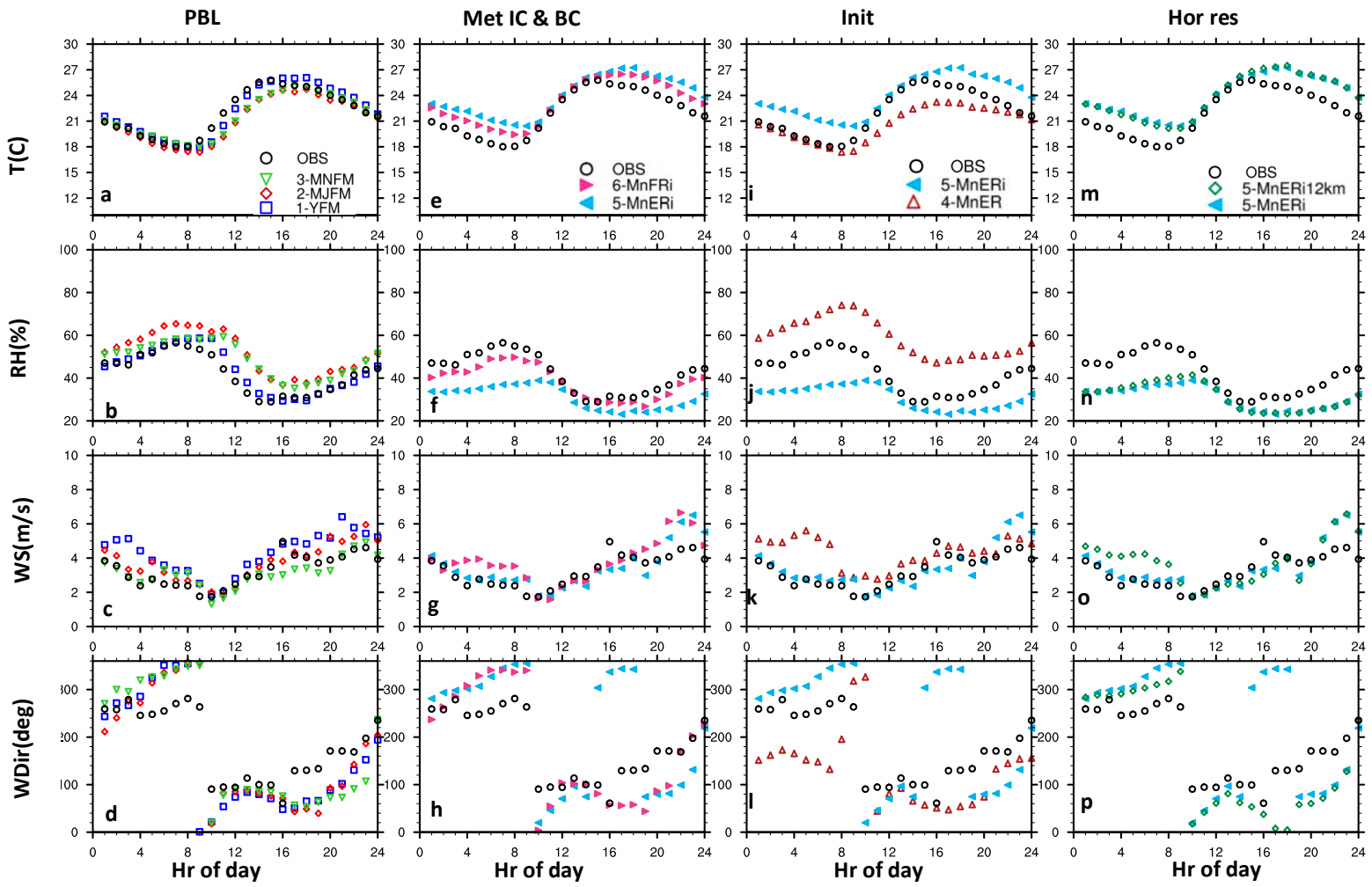

Figure A-2. Average diurnal cycle of temperature, relative humidity, wind speed, and wind direction for all test sets and observation at BAO 100m. Averages are calculated for Aug 1 to 15, 2014

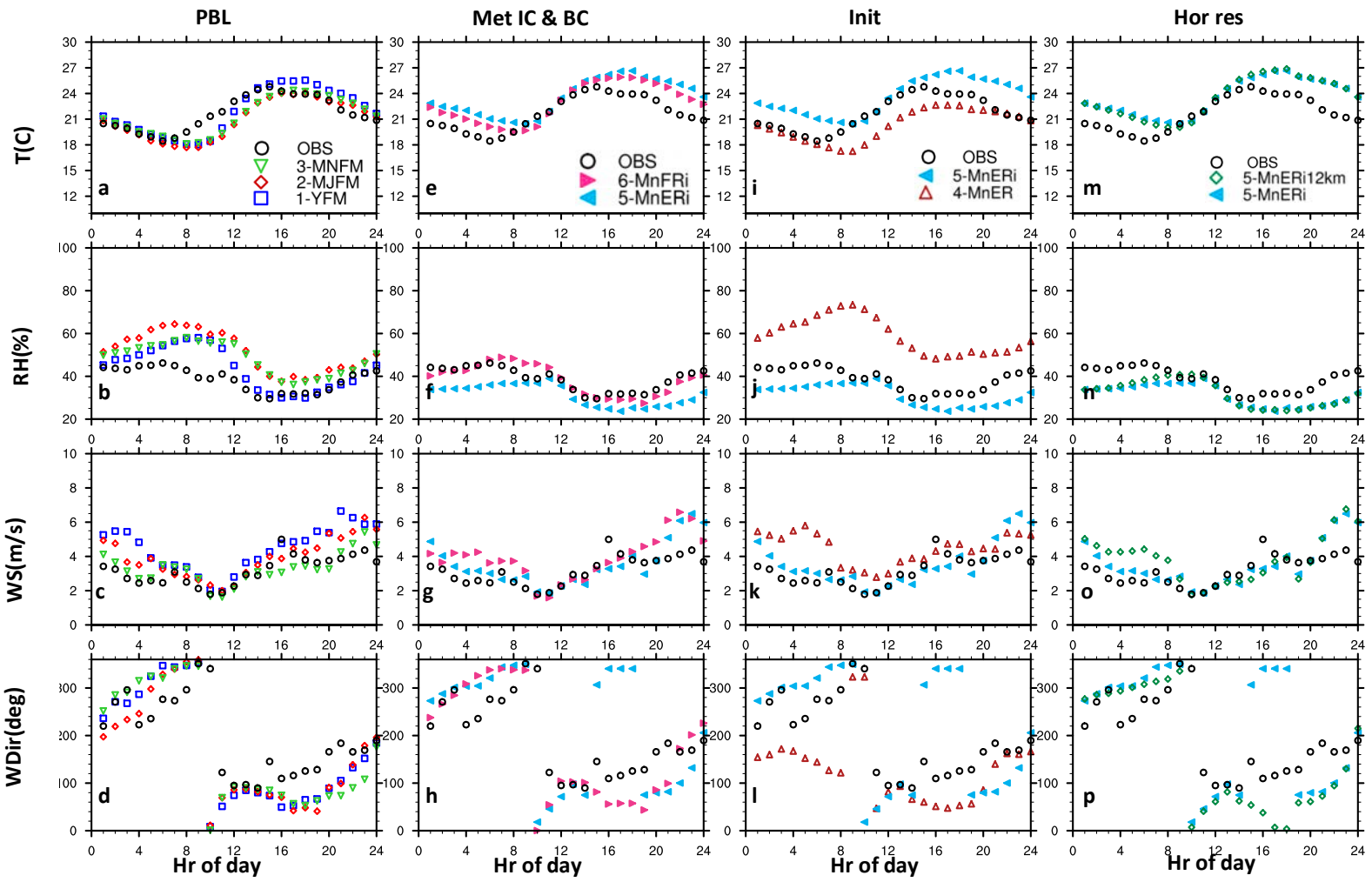

Figure A-3. Average diurnal cycle of temperature, relative humidity, wind speed, and wind direction for all test sets and observation at BAO 300m. Averages are calculated for Aug 1 to 15, 2014

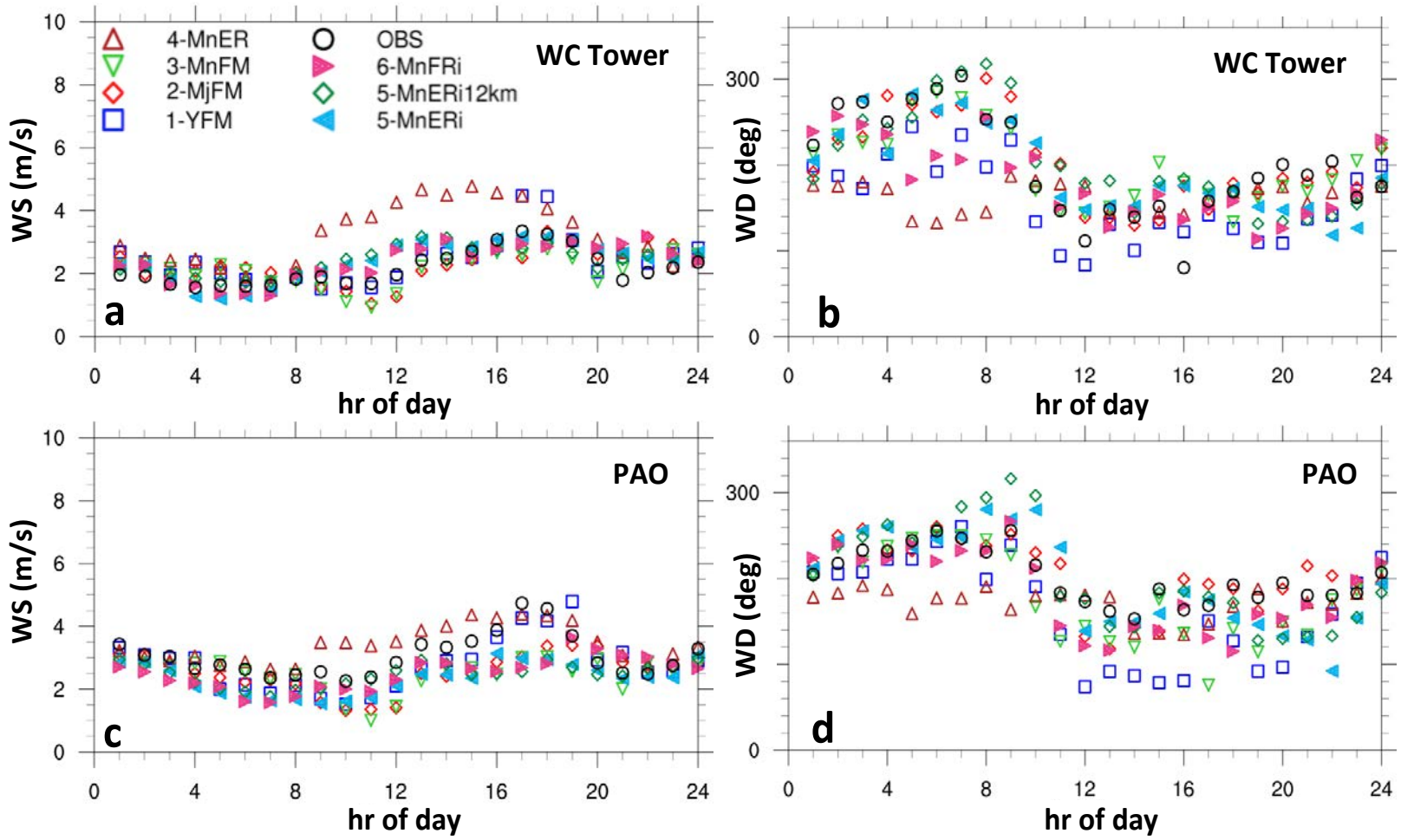

Figure A-4. Wind speed at 10m captured by different PBL schemes. averaged from 1-August to 11-August 2014

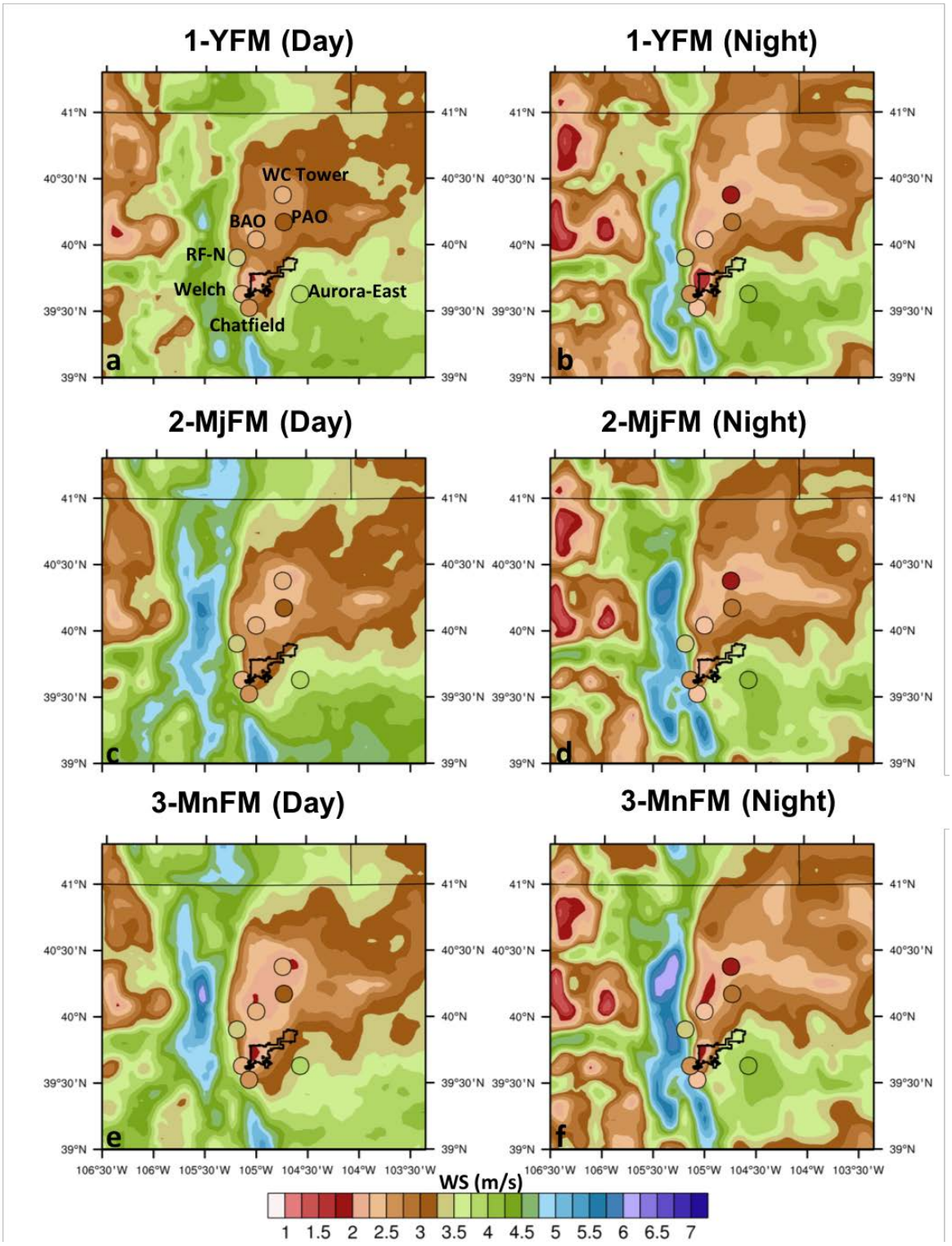

Figure A-5. Average diurnal cycle of wind speed (WS) and direction (WD) at WC Tower and PAO sites. Averages are calculated for August 1 to 11, 2014

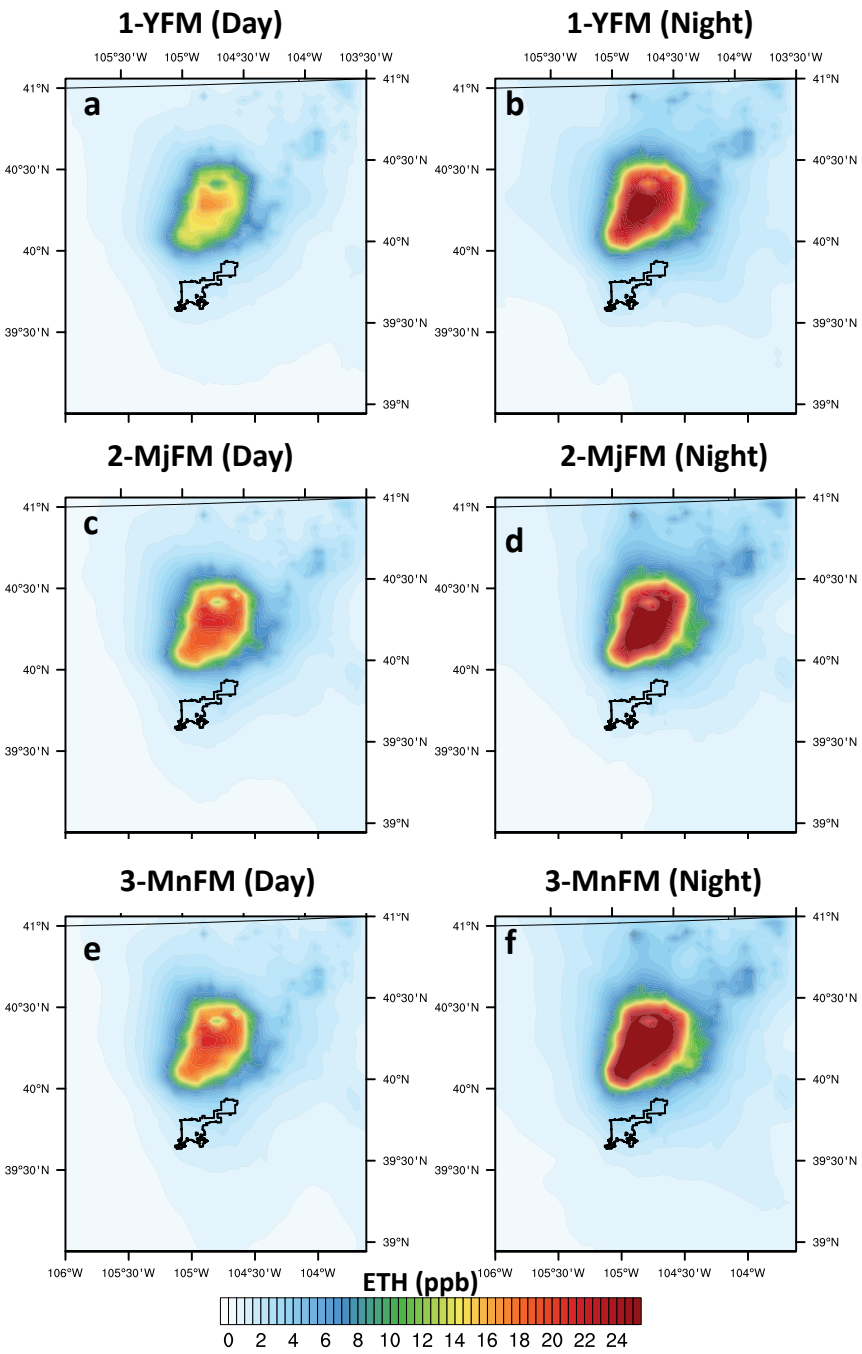

Figure A-6. Surface ethane in sim 1 (1-YFM), sim 2 (2-MjFM), sim 3 (3-MnFm) averaged from August 1 to 15, 2014

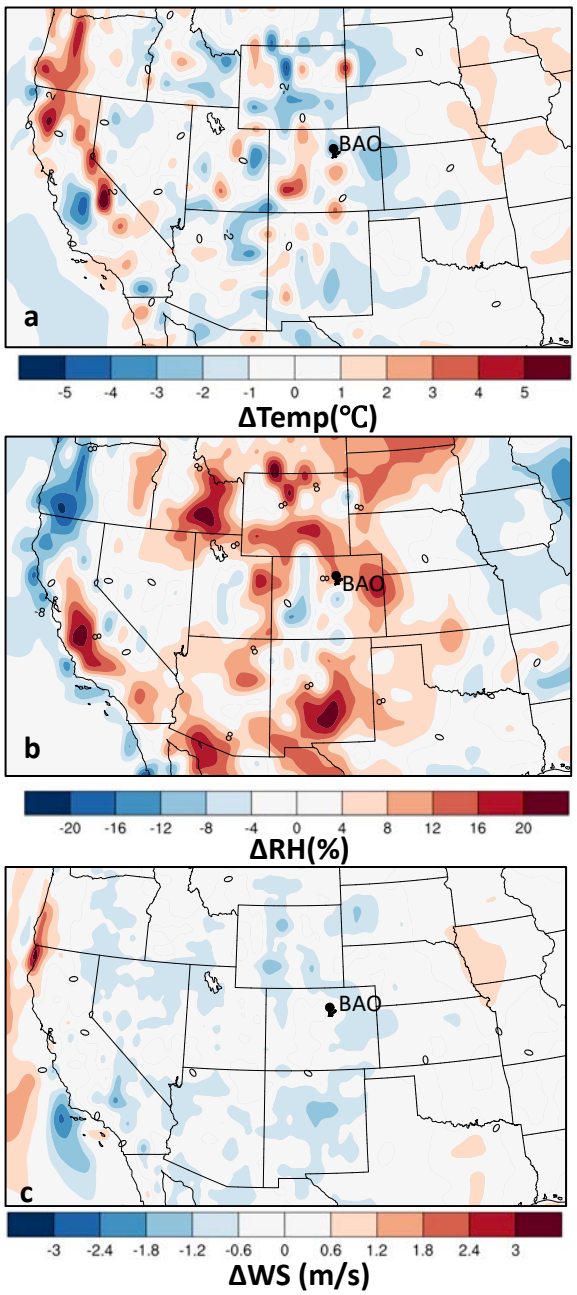

Figure A-7. Differences in temperature (a), relative humidity (b), and wind speed (c) between ERA-interim and NCEP-FNL global models (Δx = X(ERA-interim) – X(NCEP-FNL)) averaged from Aug 1 to 15, 2014 using 6-hourly data

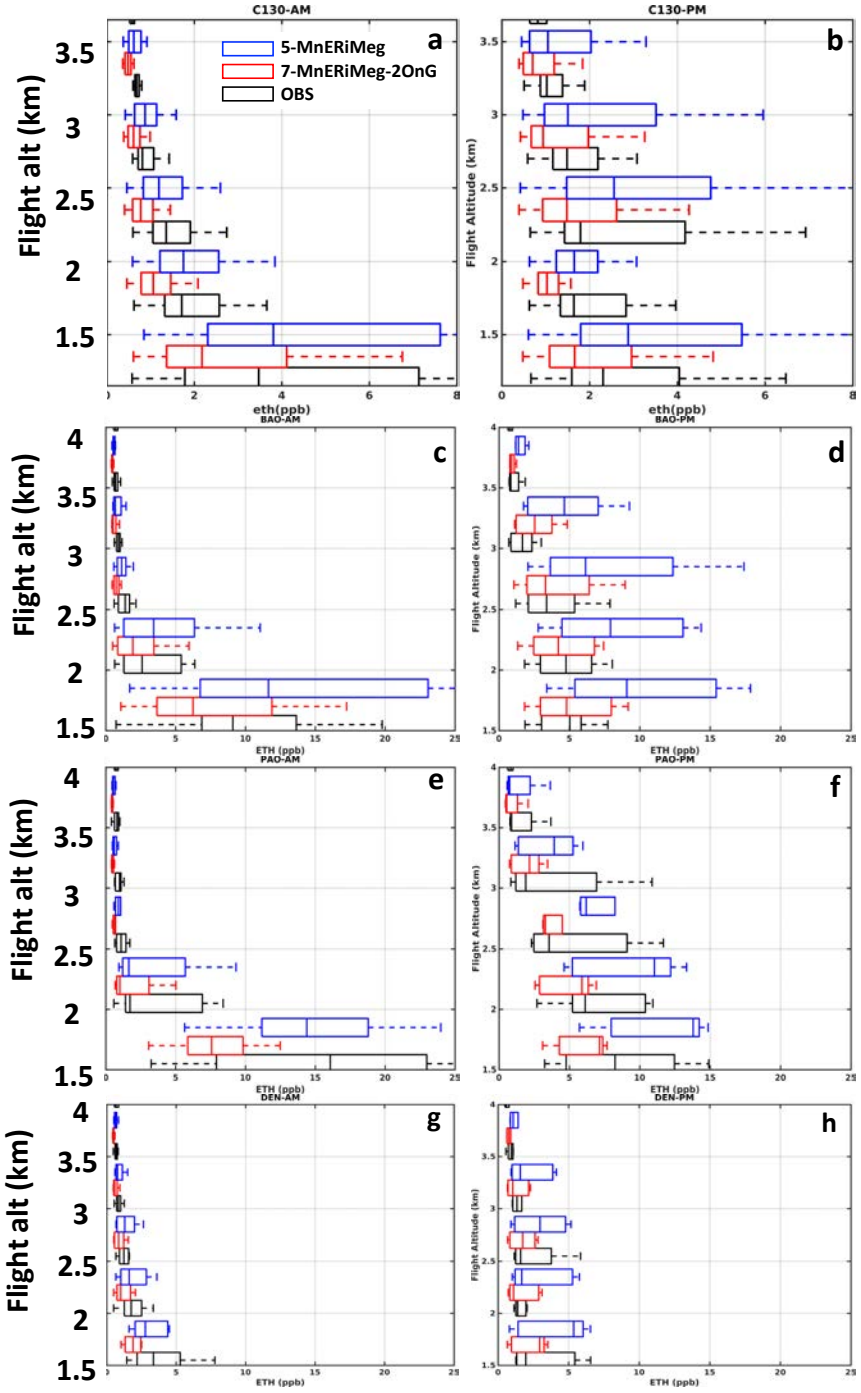

Figure A-8. Sensitivity of ethane to oil and NG emission during C130-AM (a), C130-PM (b), P3-PAO AM (d), P3-PAO PM (c), P3-BAO AM (e), P3-BAO PM (f) averaged for August flights